



## Durham E-Theses

---

### *Resonance production by energetic pions in hydrogen*

Halliwell, Harry

#### How to cite:

---

Halliwell, Harry (1968) *Resonance production by energetic pions in hydrogen*, Durham theses, Durham University. Available at Durham E-Theses Online: <http://etheses.dur.ac.uk/8754/>

#### Use policy

---

The full-text may be used and/or reproduced, and given to third parties in any format or medium, without prior permission or charge, for personal research or study, educational, or not-for-profit purposes provided that:

- a full bibliographic reference is made to the original source
- a [link](#) is made to the metadata record in Durham E-Theses
- the full-text is not changed in any way

The full-text must not be sold in any format or medium without the formal permission of the copyright holders.

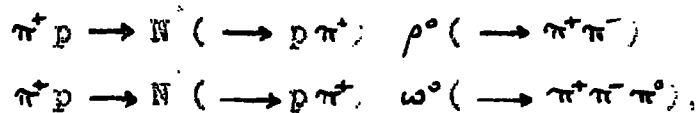
Please consult the [full Durham E-Theses policy](#) for further details.

## A B S T R A C T

An experiment has been described in which the interactions of positive pions in a hydrogen bubble chamber have been examined. Four lines of investigation have been followed.

1. The general behaviour of interactions in which four positively charged secondary particles are produced has been described. The cross-sections for these interactions and for different final states have been measured, and these have been found to be in reasonable agreement with those found in other experiments at different incident pion momenta. An examination has been made of the resonance production in reactions leading to the most common final states. Again, the results are in agreement with those from other experiments.

2. The quasi-two-body interactions:-



have been studied using the Gottfried-Jackson method of analysis. The spin density matrix elements obtained in this experiment are in agreement with the absorption model for the first of these reactions, but in poor agreement for the second reaction, as has also been found in other experiments.

3. The decay angular distribution of the  $B^+$  meson has been examined. The observed distribution is consistent with a  $J^P$  assignment of  $1^+$ .

4. Different decay modes of the  $A_2$  meson have been observed, and a sample of two pronged events with at least one visible  $V^0$  decay was examined in order to observe the  $K\bar{K}$  decay mode. The observed branching ratios are in agreement with those observed in other experiments. The recent suggestion that there may be more than one resonance with a mass in the region of the  $A_2$  mass has been investigated by examining the  $\rho\pi$  and the  $K\bar{K}$  decay modes of the  $A_2$  separately. The observed characteristics of the two decay modes is consistent with the assumption that only one meson exists with a mass in the region of  $1.0 \text{ GeV}/c^2$ .

RESONANCE PRODUCTION BY ENERGETIC PIONS IN HYDROGEN

A thesis presented by

HARRY HALLIWELL

for the

Degree of Doctor of Philosophy

at the

University of Durham

July 1968



# C O N T E N T S

|  | <u>Page</u> |
|--|-------------|
| PREFACE  |             |
| LIST OF TABLES   |             |
| LIST OF FIGURES  |             |
| INTRODUCTION .. ..   | 1.          |
| CHAPTER I <u>Review of the interactions of Elementary Particles</u> .. | 3.          |
| 1.1 General Properties of Strong Interactions ..                       | 4.          |
| 1.2 Conservation Laws ..   | 6.          |
| 1.2.1 Spin and Parity ..   | 7.          |
| 1.2.2 Isospin ..   | 7.          |
| 1.2.3 G-parity ..  | 8.          |
| 1.2.4 G-parity of $K\bar{K}$ system                                    | 10.         |
| 1.3 Particle Classification  | 11.         |
| 1.4 Interaction mechanisms ..  | 12.         |
| 1.4.1 One particle exchange (OPE) model ..                             | 13.         |
| 1.4.2 Form factor modification of (OPE) model ..                       | 14.         |
| 1.4.3 Absorption model ..  | 16.         |
| 1.4.4. Regge Pole model ..   | 19.         |
| 1.4.5 Optical model ..   | 20.         |
| CHAPTER 2 <u>Experimental Conditions</u>                               | 22.         |
| 2.1 The Exposure .. ..   | 22.         |
| 2.2 The O <sub>2</sub> Beam .. ..                                      | 22.         |
| 2.3 Contamination of the beam  | 24.         |
| 2.4 The British National Hydrogen Bubble Chamber ..                    | 25.         |
| 2.5 Quality of the film ..   | 27.         |
| 2.5.1 No-field film ..   | 28.         |
| 2.5.2 Fiducial point measurements                                      | 31.         |

|  | <u>Page</u> |
|--|-------------|
| CHAPTER 3 <u>Analysis of the film</u>                        | 33.         |
| 3.1 Introduction .. ..                                       | 33.         |
| 3.2 Scanning .. ..   | 33.         |
| 3.3 The efficiency of scanning ..                            | 35.         |
| 3.4 The length of track scanned ..                           | 36.         |
| 3.5 Selection of events for measurement                      | 37.         |
| 3.6 Measurement of Events ..                                 | 37.         |
| 3.7 Reap .. ..   | 39.         |
| 3.8 Tests in Reap  | 41.         |
| 3.8.1 Check on fiducial marks ..                             | 41.         |
| 3.8.2 Check on track measurement                             | 41.         |
| 3.8.3 Short check on track measurements                      | 42.         |
| 3.9 Thresh .. ..   | 42.         |
| 3.10 Grind .. ..   | 44.         |
| 3.11 Acceptance of events after Grind                        | 46.         |
| 3.12 Acceptance of hypotheses ..                             | 49.         |
| 3.13 The data summary type ..                                | 51.         |
| CHAPTER 4 <u>Preliminary experimental results</u>            | 54.         |
| 4.1 Cross-sections .. ..                                     | 54.         |
| 4.1.1 The 4-prong cross-section                              | 54.         |
| 4.1.2 Fitted hypotheses ..                                   | 55.         |
| 4.1.3 Channel cross-sections ..                              | 58.         |
| 4.2 Distributions of the square of the missing mass .. ..    | 61.         |
| 4.3 Data consistency .. ..                                   | 63.         |
| 4.3.1 Distributions of $\chi^2$ ..                           | 64.         |
| 4.3.2 Comparison of invariant mass distributions ..          | 65.         |
| 4.4 Angular distributions ..                                 | 66.         |
| CHAPTER 5 <u>Resonance production</u> ..                     | 68.         |
| 5.1 Introduction .. ..                                       | 68.         |
| 5.2 Estimation of cross-sections for resonance production .. | 69.         |
| 5.2.1 Fowl .. ..   | 69.         |
| 5.2.2 Empirical Background ..                                | 73.         |
| 5.2.3 Estimated Background ..                                | 75.         |
| 5.3 Reaction A .. ..   | 76.         |
| 5.3.1 $N^*$ and $\rho^0$ production ..                       | 77.         |
| 5.3.2 $f^0$ production ..                                    | 79.         |
| 5.3.3 t dependence of $N^*$ and $\rho^0$ production ..       | 80.         |
| 5.3.4 Decay angular distributions of $N^*$ and $\rho^0$ ..   | 83.         |
| 5.3.5 The $A_2$ meson ..                                     | 87.         |

|  | <u>Page</u> |
|--|-------------|
| 5.4 Reaction B ..  | 88.         |
| 5.4.1 $N^*$ , $\omega^0$ and $\gamma^0$ production ..                          | 88.         |
| 5.4.2 t dependence of $N^*$ and $\omega^0$ production ..                       | 90.         |
| 5.4.3 Decay angular distributions of $N^*$ and $\omega^0$ ..                   | 91.         |
| 5.4.4 $\rho$ production ..   | 94.         |
| 5.4.5 $A_2$ production ..  | 94.         |
| 5.4.6 The $B^+$ meson ..   | 95.         |
| 5.5 Reaction E ..  | 100.        |
| CHAPTER 6 <u>The production and decay of the <math>A_2</math> meson</u>        | 103.        |
| 6.1 Introduction ..  | 103.        |
| 6.2 The reaction $\pi^+ p \rightarrow \rho A_2$ ..                             | 105.        |
| 6.3 The reaction $\pi^+ p \rightarrow N^* A_2$ ..                              | 108.        |
| 6.4. The $A_2 \rightarrow K\bar{K}/A_2 \rightarrow \rho\pi$ branching ratio .. | 111.        |
| 6.5 The $K\bar{K}$ decay mode ..   | 114.        |
| 6.6 The $\rho\pi$ decay mode ..  | 116.        |
| 6.7 Conclusions ..   | 120.        |
| CONCLUSION ..  | 121.        |
| ACKNOWLEDGEMENTS ..  | 125.        |
| APPENDIX A ..  | 126.        |
| APPENDIX B ..  | 128.        |
| REFERENCES ..  | 130.        |

## PREFACE

This thesis is an account of the work carried out by the author whilst at the University of Durham, and is concerned with the interaction of positive pions in a hydrogen bubble chamber. The experiment described here is part of a larger experiment on the interactions of 5 GeV/c positive pions with protons being carried out by the High Energy Nuclear Physics Group of the University in collaboration with groups in the Universities of Bonn, Nijmegen, Paris (Ecole-Polytechnique), Strasbourg and Turin.

The author has been concerned with the exposure at CERN, the scanning of the film, and a considerable part of the analysis of the events measured in Durham, as well as with the analysis of the complete sample of events. Specific contributions by his collaborators are indicated in the text.

## LIST OF TABLES

| <u>Table</u>  | <u>Page No.</u> |
|---|-----------------|
| 1. $K\bar{K}$ Eigenstates of I, $I_3$ and G                               |                 |
| 2. Test of no-field film  | 29.             |
| 3. Rejection Criteria   | 47.             |
| 4. 4-prong cross-sections   | 55.             |
| 5. Distribution of fitted hypotheses                                      | 56.             |
| 6. Percentage of type A fits  | 58.             |
| 7. Ratio of type B fits to type A fits                                    | 59.             |
| 8. Reaction cross-sections  | 60.             |
| 9. Median $\chi^2$ for reaction B   | 65.             |
| 10. Comparison of $\omega^0$ peaks  | 66.             |
| 11. Forward-backward ratios   | 67.             |
| 12. $d\sigma/dt$ slopes for regions adjacent to $N^* \rho^0$ region       |                 |
| 13. Coefficients of $N^*$ and $\rho^0$ decay distributions                | 86.             |
| 14. $d\sigma/dt$ slopes for regions adjacent to $N^* \omega^0$ region     |                 |
| 15. Coefficients of $N^*$ and $\omega^0$ decay distributions              | 93.             |
| 16. Mass and width of B meson   | 100.            |
| 17. Branching ratio $A_2 \rightarrow \eta \pi / A_2 \rightarrow \rho \pi$ | 107.            |
| 18. Branching ratio $A_2 \rightarrow K\bar{K} / A_2 \rightarrow \rho \pi$ | 111.            |
| 19. Charge modes of $N^* A_2$ production                                  | 118.            |

Figure

57. Reaction G:
- Effective mass of  $\rho\pi^+$  versus effective mass of  $K^0\bar{K}^0$ .
  - Effective mass of  $K^0\bar{K}^0$ , if  $\rho\pi^+$  is compatible with  $N^*$ .
58. Cross-section for  $\pi^+\rho \rightarrow \rho A_2 (A_2 \rightarrow \rho^0 \pi^+)$  versus laboratory momentum of incident  $\pi^+$ .
59. Branching ratios of  $A_2$  decay versus laboratory momentum of incident particle in the experiment in which it was determined.
60. Reaction G: Effective mass of  $K^0\bar{K}^0$ , if both decays are observed.
61. Reaction E: Angular distribution of  $K^+K^-$  system.
- $A_2$  region,
  - control regions,
  - difference between a) and b).
62. a) Reaction B: Effective mass of  $\pi^+\pi^+\pi^-$ , if a  $\pi^+\pi^-$  combination is compatible with  $\rho^0$ , and  $\rho\pi^0$  is compatible with  $N^*$ .
- b) Reaction D: Effective mass of  $\pi^+\pi^+\pi^-$ , if a  $\pi^+\pi^-$  combination is compatible with  $\rho^0$ , and  $n\pi^+$  is compatible with  $N^*$ .
63. Reaction B: Effective mass of  $\pi^+\pi^+\pi^0$ , if a  $\pi^+\pi^0$  combination is compatible with  $\rho^+$ , and  $\rho\pi^+$  is compatible with  $N^*$ .

## LIST OF FIGURES

### Figure

1.  $\pi^+p$  total and elastic cross-sections.
2.  $K^+p \rightarrow$  three-body cross-sections.
3. Feynman diagrams for OPE models.
  - a) Simple OPE model.
  - b) OPE model with absorption.
4. Layout of the O<sub>2</sub> beam.
5. Plan view of the British National Hydrogen Bubble Chamber.
6. Diagram of the British National Hydrogen Chamber, showing the scan zone, fiducial marks and approximate positions of cameras.
7. Test of Fiducial mark system.
8. System of analysis of the data.
9. Form of paper tape output from the measuring machines.
10. General structure of Reap.
11. Track tests in Reap.
12. Relative ionisation.
13. Plot of the square of the missing mass ( $MM^2$ ) against the missing energy (ME).
14. Four-prong cross-sections.
15. The square of the missing mass for reactions A, B and D.
16. Reaction A:  $\chi^2$  distribution for each laboratory in the collaboration.
17. Reaction B:  $\chi^2$  distribution for each laboratory in the collaboration.
18. Angular distributions.

Figure

19. Reaction A:  
Effective mass of  $\rho\pi^+$  versus effective mass  
of  $\pi_2^+\pi^-$
20. Reaction A:  
Effective mass of  $\rho\pi^+$
21. Reaction A:  
Effective mass of  $\pi^+\pi^-$
22. Reaction A:  
Effective mass of  $\pi^+\pi^-$ , remaining  $\rho\pi^+$  compatible  
with an  $N^*$ .
23. Two-body cross-sections versus the laboratory  
momentum of the incident pion.
  - a)  $\pi^+p \rightarrow N^*\rho^0$
  - b)  $\pi^+p \rightarrow N^*\rho^+$
  - c)  $\pi^+p \rightarrow N^*\omega^0$
24. Reaction A: Effective mass of  $\pi^+\pi^-$ 
  - a)  $\cos \theta_{\pi^+} > 0$
  - b)  $\cos \theta_{\pi^+} < 0$

$\theta_{\pi^+}$  is the angle between the incident  $\pi^+$  and  
the outgoing  $\pi^+$ .
25. Reaction A:  $-t(\pi^+/\pi^+\pi^-)$  versus effective  
mass of  $\pi^+\pi^-$ .
26. Reaction A: Effective mass of  $\rho\pi_1^+$  versus  
effective mass of  $\pi_2^+\pi^-$ ,  
if  $-t < 0.3 \text{ GeV}^2$ .
27. Reaction A: Differential cross-section for  
 $N^*\rho^0$  production.
28. Reaction A: Section of fig. 25 for high values  
of  $|t|$ .
29. Reaction A: Differential cross-section for  
 $N^*\rho^0$  production by baryon exchange.

Figure

30. Reaction A: Spin density matrix elements for  $N^* \rho^0$  production.
31. Reaction A: Correlation of the angular distributions of  $N^*$  and  $\rho^0$  decays.
32. Reaction A: Effective mass of  $\pi^+ \pi^+ \pi^-$ .
33. Reaction A: Effective mass of  $\pi^+ \pi^+ \pi^-$ , if one  $\pi^+ \pi^-$  combination is compatible with  $\rho^0$ , but excluding events compatible with  $N^* \rho^0$  production.
34. Reaction B: Effective mass of  $\rho \pi^+$  versus of effective mass of  $\pi^+ \pi^- \pi^0$ .
35. Reaction B: Effective mass of  $\rho \pi^+$ .
36. Reaction B: Effective mass of  $\pi^+ \pi^- \pi^0$ .
37. Reaction B: Effective mass of  $\pi^+ \pi^- \pi^0$ , remaining  $\rho \pi^+$  compatible with  $N^*$ .
38. Reaction B: Number of  $\omega$ 's versus effective mass of  $\rho \pi^+$ .
39. Reaction B: Differential cross-section for  $N^* \omega^0$  production.
40. Reaction B: Spin density matrix elements for  $N^* \omega^0$  production.
41. Reaction B: Correlation of the angular distributions of  $N^*$  and  $\omega^0$  decays.
42. Reaction B: Effective mass of two-pion systems,
  - a)  $\pi^+ \pi^-$
  - b)  $\pi^+ \pi^0$
  - c)  $\pi^- \pi^0$
43. Reaction B: Effective mass of  $\pi^+ \pi^- \pi^0$ , if  $\pi^+ \pi^0$  or  $\pi^- \pi^0$  is compatible with  $\rho$ , and the associated  $\rho \pi^+$  is compatible with  $N^*$ .

Figure

44. Reaction B:
  - a) Effective mass of  $\pi^+\pi^+\pi^-\pi^0$ .
  - b) Effective mass of  $\pi^+\pi^+\pi^-\pi^0$ , if a  $\pi^+\pi^-\pi^0$  combination is compatible with  $\omega^0$ .
45. Reaction B: Dalitz plot; square of effective mass of  $\pi^+\pi^-\pi^0$  versus the square of the effective mass of  $\rho\pi^+$ .
46. Definition of  $\theta_B$ .
47. Reaction B: Effective mass of  $\omega^0\pi^+$  versus  $\cos \theta_B$ .
48. Distributions of  $\cos \theta_B$ ,
  - a)  $B^+$  meson region
  - b) control regions
  - c) difference between distributions a) and b).
49. Reaction B: Effective mass of  $\omega^0\pi^+$ ,
  - a)  $|\cos \theta_B| < 0.5$ .
  - b)  $|\cos \theta_B| > 0.5$ .
50. Reaction E: Effective mass of  $\rho\pi^+$ .
51. Reaction E: Effective mass of  $\rho K^-$ .
52. Reaction E: Effective mass of  $K^-\pi^+$ .
53. Reaction E: Effective mass of  $K^+K^-$ .
54. Reaction B: Effective mass of  $\pi^+\pi^+\pi^-\pi^0$ , if a  $\pi^+\pi^-\pi^0$  combination is compatible with  $\gamma^0$ .
55. Reaction F: Effective mass of  $K^+K^0$ .
56. Reaction E:
  - a) Effective mass of  $\rho\pi^+$  versus effective mass of  $K^+K^-$ .
  - b) Effective mass of  $K^+K^-$ , if  $\rho\pi^+$  is compatible with  $N^*$ .

## INTRODUCTION

Since the construction of beams of pions at high energy, a considerable amount of work has been done on the interaction of pions with nuclei, and much has been learnt about the strong interactions of matter as a result. The bubble chamber has been shown to be a particularly useful tool for the study of these interactions in that a permanent record of the events is made on film. Especially has it been found to be so for interactions in which a few particles are produced in the final state. It is found that a large proportion of such interactions proceed via the production of resonances which subsequently decay into two or more stable particles. A large number of resonances have been discovered over the last few years and investigations have been made to determine their properties and to classify them. The type of interaction which lends itself most easily to a theoretical approach is that in which two particles or resonances are produced, and several theories have been put forward to explain such interactions. These theories have been examined experimentally with some success although there is yet no theory which satisfactorily explains all features of two-body processes.

In chapter 1, a review of the strong interactions of elementary particles is given. The properties of

resonant states, and how they are determined experimentally are discussed, together with the main theories put forward to explain two-body processes, and their predictions.

In chapters 2 and 3 are described the exposure which took place at CERN, the scanning and measurement of the film, and the method by which the measured events were analysed.

The remaining chapters are concerned with the experimental results. In chapter 4, the preliminary results are discussed, and the checks made on the consistency of data from the several laboratories are described. Chapter 5 contains a survey of the production of resonances as observed in four pronged interactions, and in particular, some two-body processes are examined in the light of some of the theories reviewed in chapter 1. The final chapter is concerned with an examination of the  $A_2$  meson. A determination of the branching ratios into its different decay modes is presented, and the hypothesis that there exist two resonances with very similar mass to the  $A_2$  is discussed.

CHAPTER 1

REVIEW OF THE INTERACTIONS OF ELEMENTARY PARTICLES

Of the three types of interaction which are important in the study of elementary particles (strong, electromagnetic, and weak interactions) it is the strong interactions which are mainly of interest here. Firstly the general properties of interactions are briefly described. Secondly, the quantum numbers of particles and resonant states which arise from the invariance of physical processes under certain operations are discussed. Finally, the more important theories on the mechanisms of two-body interactions are described, and their experimentally observable predictions are reviewed.

## 1.1 General Properties of Strong Interactions

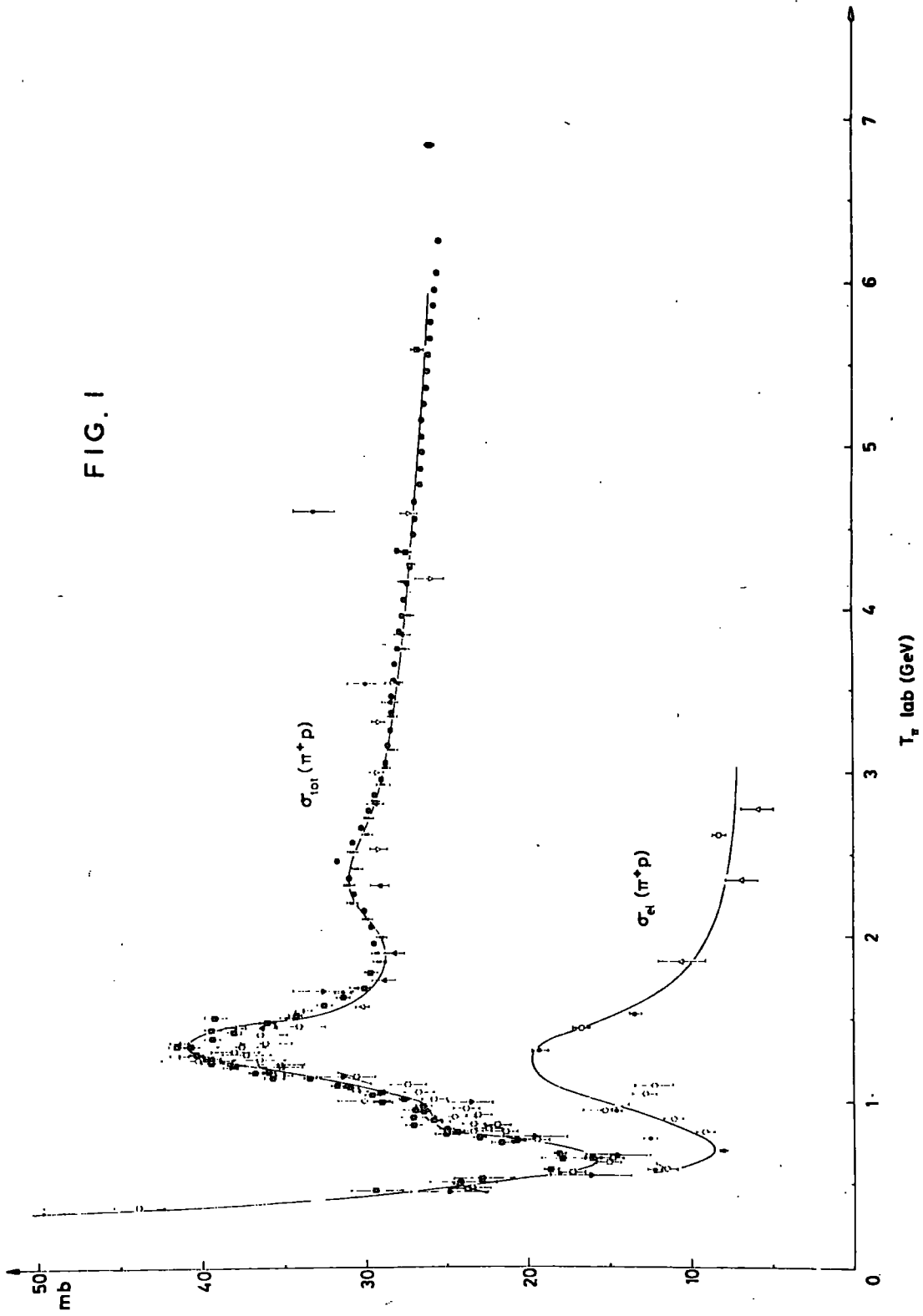
Fig 1 shows the variation of the total cross-section and of the cross-section for elastic scattering in  $\pi^+p$  interactions, as a function of the energy of the incident pion. At higher energies, (fig. 1(a)), it can be seen that the total cross-section appears to be tending towards a constant value. The elastic scattering cross-section also seems to tend towards a constant value, about one fifth of the total cross-section. A similar behaviour is also observed in the cross-sections for the interactions of other incident particles although the limit of the cross-section at high energy may be different for different incident particles.

At lower energies on the other hand (fig. 1(b)), quite rapid variations in both the total and the elastic cross-section, are observed.

The peak in the elastic scattering cross-section at the incident pion energy of 196 MeV has been interpreted as being due to the production of an intermediate resonant state, the  $N^*(1236)$ . Other variations in the elastic scattering cross-section can also be interpreted as resonant states.

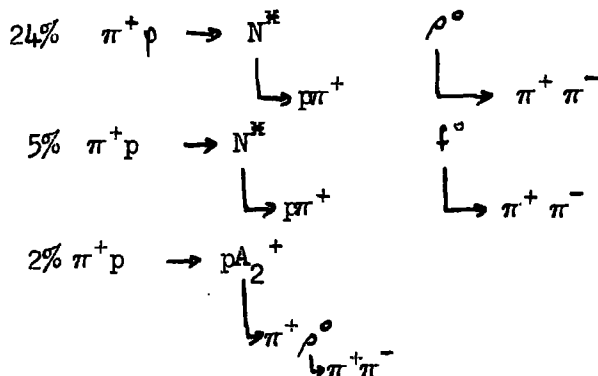
The  $N^*(1236)$  resonant state is also observed to be produced strongly in interactions in which pions are produced in the final state. The resonance decays

FIG. 1



to  $p\pi^+$ , and is observed to have an invariant mass in the region of  $1236 \text{ MeV}/c^2$ . Other resonances are also observed to be produced in interactions, including the meson resonances, of which several are observed in this experiment.

At lower energies, a large proportion of interactions proceed via the production of two particles or resonances, which may decay to produce final states of more than two particles. At higher energies, the proportion of interactions which proceed in this way decreases, and some three or more body processes take place. Even if the momentum of the incident pion is as high as a few  $\text{GeV}/c$ , a considerable proportion of the interactions resulting in the production of several particles is the result of two-body processes. The interaction  $\pi^+p \rightarrow p\pi^+\pi^+\pi^-$  at  $5 \text{ GeV}/c$  can be quoted as an example. The following two-body processes are observed to take place in 31% of the interactions.



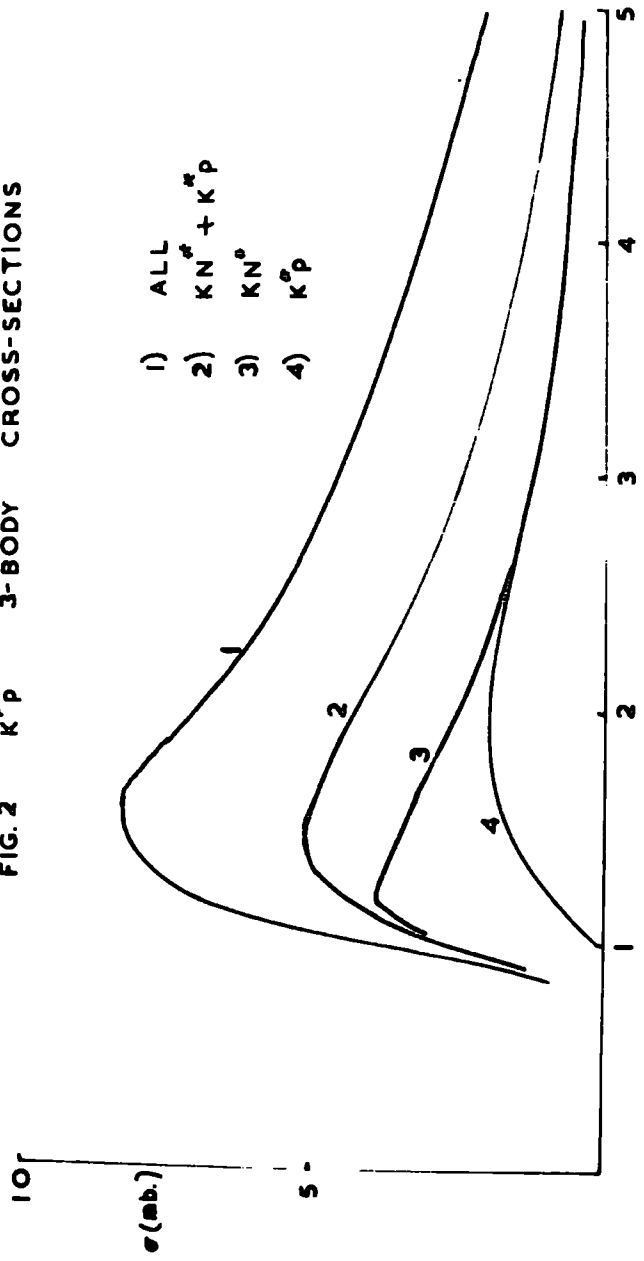
The remaining interactions are the result of three- and four-body processes.

As the energy of the incident particle is increased the threshold for new processes is passed, and the cross-section for these processes must increase. The fact that the total cross-section approaches a constant value at high energies means that the cross-section for a particular interaction should decrease with increasing energy due to the introduction of competing channels. This decrease is in fact what is observed experimentally, as for example in the reactions  $K^+p \rightarrow$  three particles shown in fig.2.

## 1.2 Conservation Laws

The interactions of elementary particles are limited by a number of conservation laws. The conservation of momentum, energy and angular momentum are well known. To every particle may be assigned quantum numbers and there are selection rules for the interactions of particles in terms of these quantum numbers. That the quantum numbers electric charge and baryon number are conserved in all interactions, and strangeness is conserved in strong interactions, is well known. The conservation laws governing other quantum numbers and some of their consequences in the study of resonances are discussed here.

FIG. 2  $K^+p$  3-BODY CROSS-SECTIONS



### 1.2.1 Spin and Parity

The quantum numbers spin (J) and parity (P) may be assigned to any particle. For any system of two particles moving with a relative orbital angular momentum,  $l$ , the composition of the spins of the two particles and of  $l$  to obtain the overall angular momentum of the system is governed by well known rules. The parity of a particle or system of particles, the property that the wave function remains the same (even parity) or changes sign (odd parity) upon spatial reflection is also observed to be conserved in strong and electromagnetic interactions. The fact that parity is conserved enables one to assign this quantum number to particles. The parity of a system of two particles which have intrinsic parities  $P_A, P_B$  is given by

$$P_A \cdot P_B \cdot (-1)^l$$

As an example, it can be seen that for a system of two pions, the  $J^P$  of the system can be  $0^+, 1^-, 2^+$ , etc. The conservation of angular momentum and of parity would therefore forbid the decay of  $\eta^0 (J^P = 0^-)$  to two pions in either strong or electromagnetic decays, and indeed, the  $\eta^0$  does not decay in this way.

### 1.2.2 Isospin

The fact that there are groups of particles which have very similar properties (such as the two nucleons or the three pions which have similar masses and

similar strong interaction cross-sections) suggests the assignment of a quantum number isospin (I) behaving in a similar way to ordinary spin, in that there are  $2I+1$  possible states of alignment. One can follow analogy between isospin and spin further by writing the commutation relations:

$$[I_k, I^2] = 0 \quad [I_k, I_j] = i\hbar I_i$$

where  $I_k, I_j, I_i$  are components of isospin. It is from these same commutation relations for ordinary spin that the rules for the addition of angular momentum are obtained, in the form of the Clebsch-Gordan coefficients. It therefore follows that the same coefficients must also apply to isospin. The fact that the Clebsch-Gordan coefficients are observed to be valid for the composition of isospin indicates the conservation of isospin in strong interactions.

### 1.2.3 G-parity

The G-parity operator has been defined by Michel (1) and by Lee and Yang (2) as,

$$G = Ce^{\pi i I_2}$$

where C is the charge conjugation operator. C has an eigenvalue only for neutral mesons, and it was shown by Lee and Yang that for a neutral meson,

$$G = C (-1)^I ,$$

and  $G$  can then be defined for all members of an isospin multiplet by its neutral member.

It was also shown that, if  $G$ -parity is conserved in interactions, a state consisting of an odd number of pions could not be transformed into a state with an even number of pions and vice versa. Thus the  $G$  parity of a meson can readily be determined by the number of pions produced in its strong decay. As  $G$  is related directly with isospin, it is only conserved in strong interactions. The conservation of  $G$ -parity therefore forbids such decays as  $\rho \rightarrow 3\pi$  or  $\omega^0 \rightarrow 2\pi$ . The

$\gamma^0 (G = +1)$  is also forbidden to decay strongly to three pions by this rule, and because, as has already been mentioned, the decay to two pions is forbidden by parity, the  $\gamma^0$  can not decay by strong interactions.

The decay of a meson to two pions or to  $K\bar{K}$  is of particular interest in the assignment of quantum numbers to mesons. If such a decay occurs with orbital angular momentum,  $l$ , then

$$G = (-1)^{l + I}$$

As an example, the  $B$  meson which has  $G = +1$  and  $I = 1$  can only decay to two pions or to  $K\bar{K}$  if these are produced with  $l$  even.

### 1.2.4 G-parity of $K\bar{K}$ system

Lee and Yang defined the G-parity operator for the kaons thus:

$$G \begin{bmatrix} K^+ \\ K^0 \\ \bar{K}^0 \\ -K^- \end{bmatrix} = \begin{bmatrix} \bar{K}^0 \\ -K^- \\ -K^+ \\ -K^0 \end{bmatrix}$$

It can be seen that a kaon is not an eigenstate of the G-parity operator, so a kaon can not have an eigenvalue of G-parity. It is possible to construct 16 states of two kaons, of which eight have strangeness  $S = 0$ . It was shown by Goldhaber et al. (3) that it is possible to construct from these eight states, linear combinations which are eigenstates of  $I_3$  (charge),  $I$  and  $G$ . These states are listed in table 1. Thus if a meson decays by strong interaction to  $K\bar{K}$ , it does so into the appropriate one of these states. It is also known that  $K^0$  and  $\bar{K}^0$  are not observable states of decay themselves, but  $K_S$  and  $K_L$ , the short and long-lived modes are, and it can be written:

$$K^0 = 1/\sqrt{2} (K_S + iK_L) \quad \text{and} \quad \bar{K}^0 = 1/\sqrt{2} (K_S - iK_L)$$

TABLE I    K $\bar{K}$  EIGENSTATES OF  $I_3, I$  AND G

| $I_3 = Q$ | $I^G$ | PRODUCTION WAVE FUNCTION                                   | DECAY WAVE FUNCTION                                |
|-----------|-------|--|--|
| +1        | $1^-$ | $1/\sqrt{2} [K^+ \bar{K}^0 + \bar{K}^0 K^+]$               | $1/2 [K^+ K_S - i K^+ K_L + K_S K^+ - i K_L K^+]$  |
|           | $1^+$ | $1/\sqrt{2} [K^+ \bar{K}^0 - \bar{K}^0 K^+]$               | $1/2 [K^+ K_S - i K^+ K_L - K_S K^+ + i K_L K^+]$  |
| -1        | $1^-$ | $-1/\sqrt{2} [K^0 K^- + K^- K^0]$                          | $-1/2 [K_S K^- + i K_L K^- + K^- K_S + i K^- K_L]$ |
|           | $1^+$ | $-1/\sqrt{2} [K^0 K^- - K^- K^0]$                          | $-1/2 [K_S K^- + i K_L K^- - K^- K_S - i K^- K_L]$ |
| 0         | $1^-$ | $1/2 [-K^+ K^- + K^0 \bar{K}^0 + \bar{K}^0 K^0 - K^- K^+]$ | $1/2 [-K^+ K^- - K^- K^+ + K_S K_S + K_L K_L]$     |
|           | $1^+$ | $1/2 [-K^+ K^- + K^0 \bar{K}^0 - \bar{K}^0 K^0 + K^- K^+]$ | $1/2 [-K^+ K^- + K^- K^+ - i K_S K_L + i K_L K_S]$ |
|           | $0^-$ | $1/2 [-K^+ K^- - K^0 \bar{K}^0 + \bar{K}^0 K^0 + K^- K^+]$ | $1/2 [-K^+ K^- + K^- K^+ + i K_S K_L - i K_L K_S]$ |
|           | $0^+$ | $1/2 [-K^+ K^- - K^0 \bar{K}^0 - \bar{K}^0 K^0 - K^- K^+]$ | $1/2 [-K^+ K^- - K^- K^+ - K_S K_S - K_L K_L]$     |

Thus if the decays of the kaons produced by the meson are to be observed, the wave functions must be written in the second form which is also shown in the table.

Consider for example the decay of the  $A_2$  meson, which has  $I^G = 1^-$ , to  $K\bar{K}$ . The wave functions for the three charge states can be seen in table 1, together with their decay wave functions. It can be seen that the decay of the neutral kaon from the decay of the charged  $A_2$  is observable equally in the two modes, as expected. It can be seen however that the decays of neutral kaons produced by an  $A_2^0$  are correlated, and the decay mode  $K_S K_L$  is not an observable state. Further, the decay of the  $A_2^0$  to  $K\bar{K}$  is observed in the three forms  $K^+K^-$ ,  $K_S K_S$ , and  $K_L K_L$  in the ratio 2:1:1.

### 1.3 Particle Classification

Attempts have been made to arrange particles into groups having similar properties. The grouping of particles into isospin multiplets has already been discussed. Work by Gell-Mann (4) and Ne'eman (5) led to the classification of particles into  $SU_3$  groups, all particles in a group having the same spin and parity but differing in the third component of isospin and the hypercharge (defined as baryon number + strangeness). Thus the groups  $N, \Lambda^0, \Sigma, \Xi$  and  $\pi, \eta^0, K, \bar{K}$  form the  $1/2^+$  baryon octet and the  $0^-$  meson octet respectively. The particular success of the

theory was the prediction of the  $\Omega^-$  to complete the  $3/2^+$  decuplet (with  $N^*$   $3/2$  (1236),  $Y_0^*$  (1385), and  $\Xi^*$   $1/2$  (1530)) and its subsequent discovery by Barnes et al. (6).

The  $SU_3$  symmetry of elementary particles has been interpreted by Gell-Mann (7) by the quark-model, in which the particles are composite states of quarks which are assumed to have spin  $1/2$ , charge  $-1/3$  or  $+2/3$ , and baryon number  $1/3$ . A meson is then a quark-antiquark state, and a baryon is a state of three quarks, the spin and parity being determined by the relative spins and orbital angular momentum. The symmetry has been extended by Gurnsey and Radicati (8) on these lines to the  $SU_6$  group.

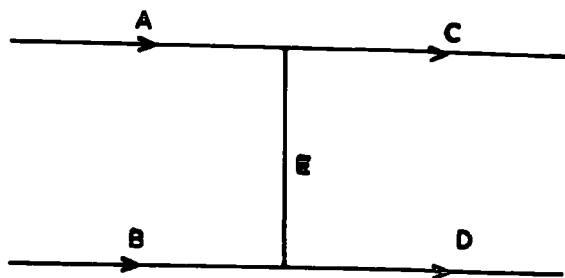
1.4 Interaction mechanisms

The simplest form of interaction is that in which two particles are produced in the final state, where a particle here is understood to include resonant states decaying to two or more stable particles. It is natural then, in order to understand the processes by which elementary particles interact, that two-body processes should be studied. The models which are successful in explaining two-body processes could then be extended to examine multi-body processes.

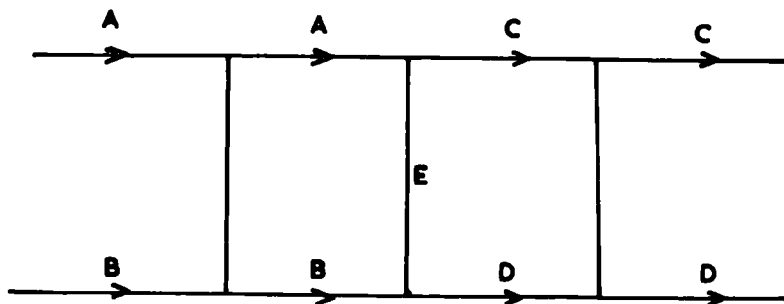
Fig. 3 (a) shows a Feynmann diagram for the reaction  $A+B \rightarrow C+D$ . The exchange particle, E, Shown on the diagram is not essential for the first part of this discussion and can for the moment be ignored. In discussing this reaction it is useful to define the usual Mandelstam variables.

FIG. 3  
OPE MODEL

a) SIMPLE



b) WITH ABSORPTION



$$\begin{aligned} s &= (q_A + q_B)^2 = (q_C + q_D)^2 \\ t &= (q_C - q_A)^2 = (q_D - q_B)^2 \\ u &= (q_C - q_B)^2 = (q_D - q_A)^2 \end{aligned}$$

Where  $q$  is the four-momentum of each particle, the metric being defined by  $q = (E, i\vec{p})$ . The three variables are not independent but are related thus:-

$$s+t+u = m_A^2 + m_B^2 + m_C^2 + m_D^2 \quad (m = \text{mass})$$

Thus,  $s$  is the square of the centre of mass energy of the system, and  $t$  is the square of the four-momentum transfer of the interaction. The variable  $u$  has no obvious physical interpretation. The dependance of interactions as functions of these variables is examined in terms of different models.

#### 1.4.1 One particle exchange (OPE) model

The fact that reactions are observed to proceed preferentially at low values of  $t$  suggests that interactions take place by the exchange of a particle. On fig. 3 (a), this is shown as the particle E. On such a model, the transition amplitude contains the propagator term  $(m_E^2 - t)^{-1}$ , and therefore has a pole at  $t = m_E^2$ . This is in the unphysical region, and the model therefore predicts the observed peaking in  $t$ . This peak should be particularly pronounced if  $m_E$  is small, and one would expect reactions taking place by one pion exchange to be very peripheral.

In an interaction of the type shown in fig. 3(a) the exchanged particle is not unlimited. The usual conservation laws valid for strong interactions must hold at each vertex, so only those particles whose quantum numbers can satisfy the conservation laws may be exchanged. The transition amplitude for the reaction is then the sum of the amplitudes for all possible exchange processes.

Badier et al. (9) have examined the reaction:



If a meson were to satisfy the conditions of the exchange particle, it would have  $Q = 2$ ,  $S = 2$  and such a meson is not known to exist. If the reaction were to proceed by the exchange of a baryon, on the other hand, the exchanged particle would have  $Q = 0$ ,  $S = 1$ . The only particle with simple quantum numbers that can be exchanged is therefore a baryon. Moreover if  $t$  is defined as  $(q_K^+ - q_p)^2$  the usual peak at small values of  $|t|$  is observed, in evidence of baryon exchange mechanisms.

One consequence of the model for the exchange of a pion (or some other spinless particle) should be mentioned. As the exchange particle has no spin, no information about the alignment of the angular momentum at any vertex can be transferred to the other vertex. There should therefore be no correlation between the production planes of the two vertices, nor any correlation between the decays of the two particles produced. The fact that

such correlations are observed indicates that the one pion exchange model without modification can not fully explain two-body processes.

Another drawback to the unmodified OPE model is that, although there is qualitative agreement with the  $t$ -dependence of interactions, detailed agreement with experiment is not obtained. The cross-section is in general too high at larger values of  $|t|$ .

One also observes that the  $t$ -dependence of such processes as  $\pi p \rightarrow N^* \pi$  ( $\pi$  exchange forbidden) and  $\pi p \rightarrow p \rho$  ( $\pi$  exchange allowed) is very similar at high energies. (See for example ref.10) The energy dependence of interactions is also in disagreement with experimental data.

#### 1.4.2 Form factor modification of OPE model

In order to account for the dependence of the cross-section on  $t$ , phenomenological form factors were introduced (11). The differential cross-section would then be written in the form:-

$$\frac{d\sigma}{dt} = \frac{1}{PA^2 S} \cdot V_{ACE}(t) \cdot V_{BDE}(t) \cdot \frac{|F(t)|^2}{(m_E - t)^2}$$

$PA$ , the momentum of the incoming particle, is measured in the overall centre of mass system.

$V_{ACE}, V_{BDE}$  are terms for the vertices, and are dependent on  $t$ .

$F(t)$  is the form factor.

The result of including such a form factor is that reactions with high values of  $|t|$  are suppressed, and the  $t$ -dependence predicted is in reasonable agreement with the experimentally observed dependence. The obvious disadvantage of such a model is that it is only a phenomenological approach. In addition, the form factor is only a function of  $t$ , so the predictions of the decay angular distributions, and the energy dependence remain the same as for the unmodified OPE model.

#### 1.4.3 Absorption model

A modification to the OPE model was suggested by Sopokovich (13) who postulated interactions of the initial and final states. The simplest form of such interactions is elastic scattering, as represented schematically in fig 3(b). In this form, the model was first applied to the reaction:-  $\pi p \rightarrow p p$

The model predicts directly a reduction in the cross-section for high values of  $|t|$ , and the calculated variation of  $d\sigma/dt$  agrees well with experimental results.

The orbital angular momentum of a resonance produced by a two-body reaction lies perpendicular to the production plane. That is, the component of

the spin of a final state particle along the direction of the incoming particle, in its own centre of mass, is zero. On the basis of the simple OPE model, the direction of the incoming and outgoing particles is the same at the point of interaction and far from it, and the above statement would be true if the direction of the incoming particle far from the point of interaction.

On the basis of the absorption model, however, the other matrix elements may become non-zero. Moreover the model predicts the values of the spin density matrix elements as functions of  $t$  and can be used to test the model experimentally. Gottfried and Jackson (13) have shown how the spin density matrix elements may be determined from the decay angular distributions for various reactions. For example the decay distribution of the  $\rho^0$  is of the form:-

$$W(\theta, \phi) = \frac{3}{4\pi} \left[ \rho_{11} \sin^2 \theta + \rho_{00} \cos^2 \theta - \rho_{1,-1} \sin^2 \theta \cos 2\phi - \sqrt{2} \operatorname{Re} \rho_{10} \sin 2\theta \cos \phi \right]$$

Where  $\theta$  is the angle between the outgoing  $\pi^+$  and the incoming particle.

$\phi$  is the angle between the decay plane of the  $\rho^0$  and the production plane at the baryon vertex.

It should be noted that, because of the invariance of the reaction under reflection, some of the spin density matrix elements are equal. In

addition because of unitarity the four elements in the above expression are not all independent and one has further that:-

$$\rho_{11} = 1/2 [1 - \rho_{00}]$$

If the final state interaction includes spin-exchange scattering the conclusion from the simple one-pion-exchange model, that there can be no correlation between the spins of the two final products of the interaction, is no longer valid. Indeed, the absorption model predicts such a correlation and suggests a search for correlation between the decays of the final state particles.

It is found that, for the exchange of a pseudoscalar meson such as a pion, the agreement between the predictions of the absorption model and experimental results is good. The dependence of the reactions on  $s$  and  $t$  are reasonably well accounted for, and in particular the reaction  $\pi p \rightarrow p \rho$  is very successfully described by the model. The model overestimates, however, the cross-section for reactions in which two resonances, or a resonance with  $J = 2$ , is produced. The correlation between the decays, when two resonances are produced, agree well with experiment.

For reactions in which a vector meson, such as

$p$ , is exchanged, on the other hand, the agreement between the predictions of the absorption model and experimental results is not good. The  $s$ -dependence of the cross-sections is not correctly predicted. The spin-density matrix elements, and their dependence upon  $t$ , are in disagreement with experiment.

A further extension of the model is to include inelastic processes in the initial and final state interactions. An advantage is that unitarity can be built into the model. This extension to the absorption model retains the successful predictions of the absorption model and, in addition, gives a proper normalisation of cross-sections. The failure of the model to explain vector meson exchanges still remains after this extension.

#### 1.44 Regge Pole Model

In this model, reactions are considered in terms of the exchange of a Regge trajectory which has quantum numbers which satisfy the conservation laws at both vertices. At high energy, the transition matrix element is given by:-

$$T(s, t, u) = \sum_{s \rightarrow 0} \sum_J \left( \frac{s-u}{S_J} \right)^{\alpha_J(t)} \beta_J(t) \frac{1 \pm e^{-i\pi\alpha_J(t)}}{\sin \pi\alpha_J(t)}$$

The sum is performed over all possible trajectories

and over all possible exchanges of spin.  $\alpha_j$  is a function only of the exchanged trajectory and is therefore independent of the initial and final state particles. In practice, the reaction is dominated by only a few terms of the above expression, and the calculation is further simplified if one studies reactions in which only one or two trajectories may be exchanged.

The model accounts well for the dependence of cross-section on  $s$  and  $t$  for both pseudoscalar and vector meson exchanges. It does not however make any predictions about the polarisation of the final state, or about the decay angle correlations, which is one of the successful features of the absorption model.

#### 1.4.5 Optical Model

Experimentally, it is observed that, at high energies, the differential cross-section of two-body reactions can be expressed roughly in the form:-

$$\frac{d\sigma}{dt} \propto e^{-at}$$

For elastic scattering, it is found that  $a \approx 10 \text{ GeV}^{-2}$ . For a large number of inelastic two-body reactions, it is found that the slope of the distribution has much the same value. (See for example ref. 10.) This suggests a behaviour similar to optical diffraction,

in which  $a = (R/2)^2$ , where R is the radius of the interaction volume.

CHAPTER 2

EXPERIMENTAL CONDITIONS

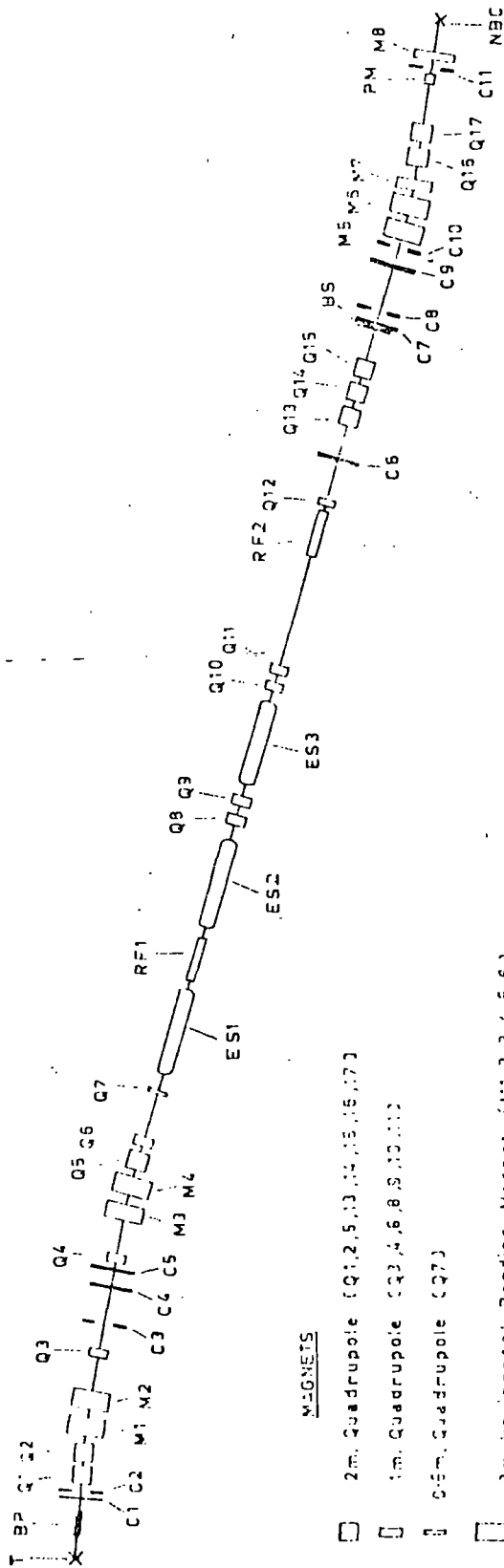
2.1 The Exposure

The exposure took place during February, 1965. About 150,000 pictures were taken of the British National Hydrogen Bubble Chamber exposed to a beam of pions with a momentum of 5 GeV/c produced by the O2 beam. The pictures were divided amongst the laboratories taking part, Bonn, Durham, Ecole-Polytechnique (Paris), Nijmegen, Strasbourg and Turin, and each laboratory was responsible for the scanning, measuring and the initial analysis (i.e. up to the preparation of the data summary tape) of its own films.

2.2. The O2 Beam (14)

The O2 beam was built in the East Experimental area of the CERN proton synchrotron to provide beams for the British National Hydrogen Bubble Chamber. The beam, 180 metres long contained both electrostatic and radiofrequency separators, but for this experiment, only the electrostatic separation was used. The layout of the beam is shown in fig. 4.

A flux of particles was produced at the target using about 10% of the intensity of protons in the synchrotron, the production angle for positive particles being  $5.1^\circ$ . The particles pass first through an iron tube, thus eliminating the effects



MAGNETS

- 2m. Quadrupole (Q1,2,5,10,14,15,16,17)
- 1m. Quadrupole (Q3,4,6,8,9,10,11)
- 0.5m. Quadrupole (Q7)
- 2m. Horizontal Bending Magnet (M1,2,3,4,5,6)
- 1m. Vertical Bending Magnet (M7,8)
- 1m. Pulsed Vertical Bending Magnet (PM)

COLLIMATORS

- Horizontal Collimator (C2,3,8,10,11)
- Vertical Collimator (C1,4,5,6,7,9)

Beam Stopper (BS)

SEPARATORS

- Electrostatic Separator (ES1,2,3)
- Radiofrequency Separator (RF1,2)

T = Target

NBC = Bubble Chamber

Fig 4 THE O<sub>2</sub> BEAM LAYOUT

of the field of the next synchrotron magnet. Horizontal and vertical collimators C1, C2 defined the angular spread of the beam. The quadrupole lenses Q1, Q2, Q3 refocussed the beam on the collimators C3, C4. The bending magnets M1, M2 produced a dispersion of the beam so that the collimator C3 was used to select the momentum of the particles. After the lens Q4 and the bending magnets M3, M4, there was again no dispersion in the beam.

From the collimator C4, the lenses Q4, Q6, Q7 produced a beam which was parallel in the vertical plane. The electrostatic separation stage then followed and the lenses Q10, Q11, Q12 produced a vertical focus on the collimator C6 where the appropriate mass of the beam was selected.

The lenses Q13, Q14, Q15 focussed the beam on the collimators C7, C8. The angular spread of the beam was redefined by the collimator C9 and the gap of the vertical bending magnet M7. The magnets M5, M6 and the lenses Q16, Q17 produced a dispersed horizontal image at the collimator C11, where the momentum bite was redefined. This redefinition of momentum was done in order to improve the purity of the beam.

The lenses Q16, Q17 produced a vertical focus in the bubble chamber which was swept across the chamber by a pulsed magnet. The bending magnets M7, M8 were used to direct the beam into the bubble chamber.

### 2.3 Contamination of the beam

The contamination in a beam of pions consists of the muons from the decay of the pions. In the O2 beam the momentum was reanalysed just before the chamber by the bending magnets M5, M6 and the collimator C11. Thus muons resulting from decays of pions before this stage of the beam would be stopped at the collimator C11 if their momentum was significantly different from the beam momentum. Only those pions which decayed within a few degrees of the beam direction in the pion rest system would produce a muon that would be accepted at C11. Thus one could assume that all the particles leaving that collimator were pions. All the muons produced between this point and the chamber, a distance of about six metres, would enter the chamber, and some of them would be indistinguishable from a beam pion. At 5 GeV/c, the number of pions decaying in its six metres of path before entering the chamber is about 2.2%. The decision as to whether a track is a beam pion or not on the scan table is a

rather subjective one, and so the proportion of muons which would be accepted as a beam pion is uncertain, but probably about one third of the muons would be rejected as being not a beam track. With this assumption the muon contamination of the beam would be 1.5%.

#### 2.4 The British National Hydrogen Bubble Chamber

A simplified diagram of the chamber is shown in fig. 5. The chamber itself has a length of 152 cm., is about 45 cm. wide, and 50 cm. high. The windows on either side are of borosilicate glass with a refractive index of 1.523. The windows are protected by a hydrogen shield and this is surrounded by a liquid nitrogen system to reduce heat lost by radiation. The whole of this is then suspended in a vacuum tank. The windows of the hydrogen shield and of the vacuum tank are of a similar glass to the windows and are respectively 25.5 and 16mm. thick. Thus the total thickness of glass through which the chamber is seen by the cameras is 19.65 cm.

The chamber is operated with liquid hydrogen at 27°K under a pressure of 6.3 kg.cm.<sup>-2</sup> the pressure being reduced to 2.8 kg.cm.<sup>-2</sup> on expansion. The signal for the expansion is received

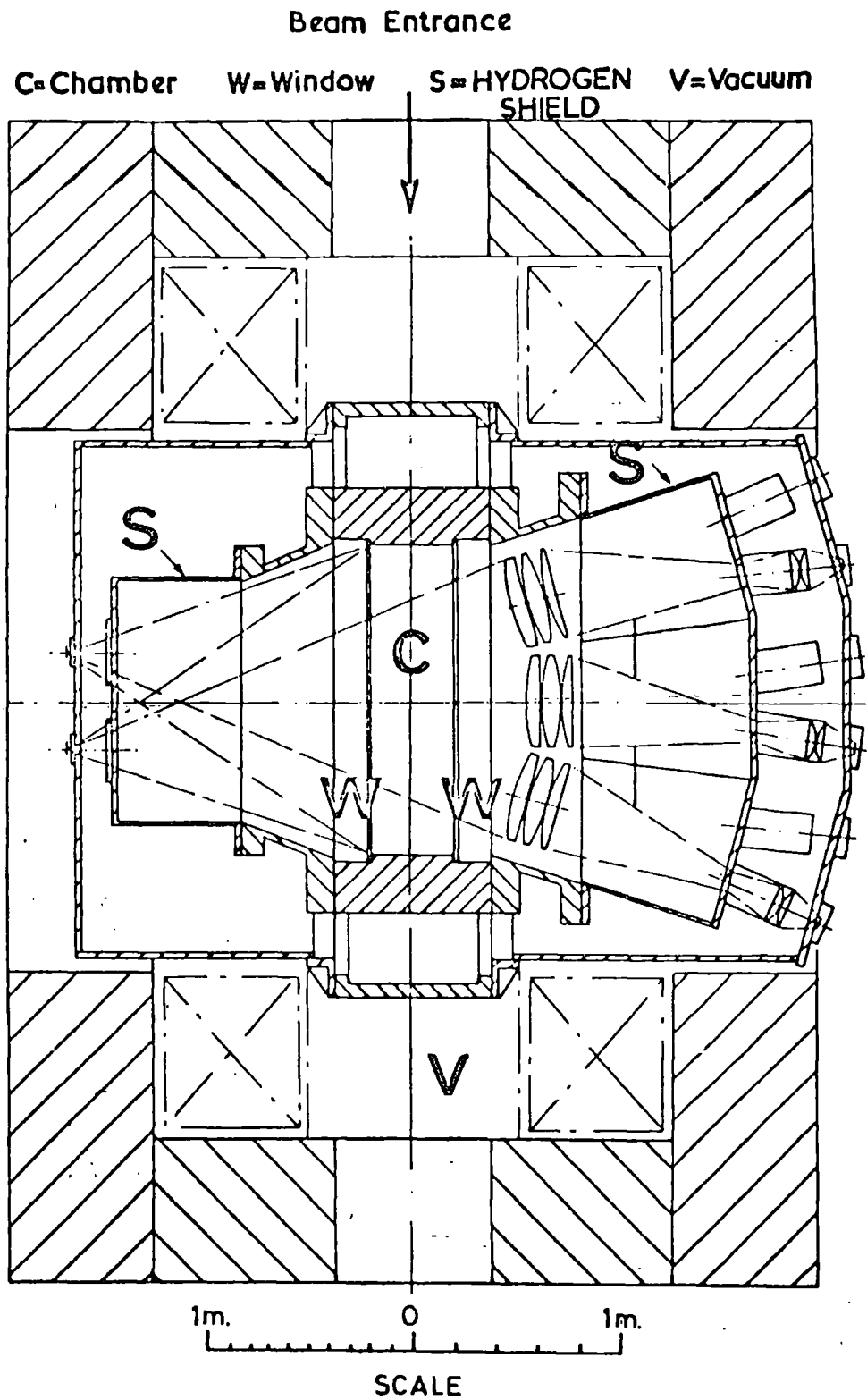


FIG. 5 PLAN VIEW OF B.N.H.B.C. SHOWING OPTICAL SYSTEM AND MAGNET.

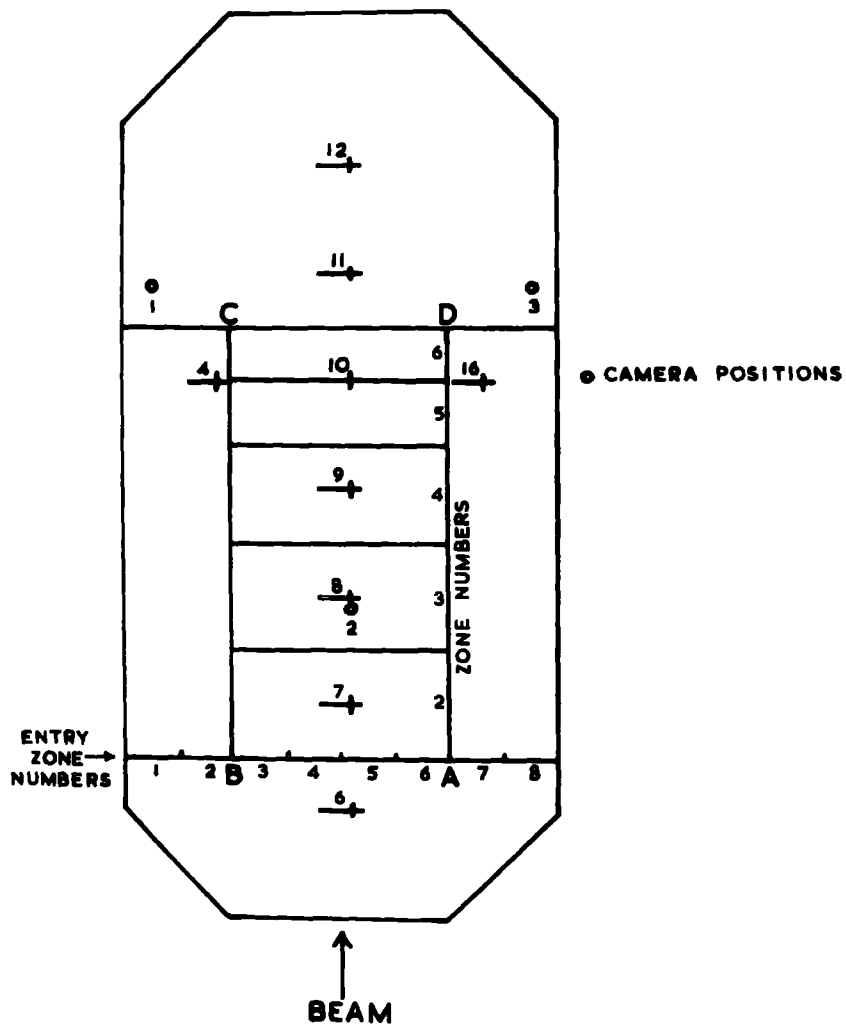
from the proton synchrotron 30 ms. before the particles enter the chamber so that when the beam particles arrive, the hydrogen is fully expanded to its superheated state. The expansion valves are closed and the recompression valves opened after the flash tubes have fired, the hydrogen being returned to its normal state in about 10 ms.

The beam is detected by a scintillation counter, which provides a signal for the flash tubes. These are fired 1 ms. after the particles have entered the chamber so that the bubbles have grown to the right size. There are nine flash tubes, arranged in three groups, each group with a condenser lens so that the chamber volume is uniformly illuminated.

The chamber is photographed by an array of three cameras whose lenses and film gates form part of a rigid assembly on a cast metal plate. The cameras have parallel axes and their positions are shown in fig. 6, forming an isosceles triangle with a base and height of 48 cm. The cameras use 35 mm. unperforated film which is kept flat in the film gates by sucking it onto flat glass plates.

The chamber has a reference system of fiduciary crosses ruled on the surfaces of the windows which are in contact with the liquid. The relative positions of the crosses on the same window

FIG 6 DIAGRAM OF B.N.H.B.C.



are accurately known. A camera based fiducial mark, an eight-sided figure around the image of the chamber, is printed on the film through the glass plates on which the film is held. This system could be used to determine the relative positions of the cameras and of the two chamber fiducial surfaces. (15).

On each frame the film number and the frame number were photographed, together with other information not used in this experiment.

The chamber is surrounded by an electromagnet which for this experiment gave a magnetic field at the centre of the magnet of 13.46 kgauss. The percentage variation of the magnetic field over the chamber has been measured (16). This was found to be the same for two different magnet currents giving central field values on either side of the value for this experiment, so it can be assumed that the same field map is valid for this experiment. The central value used here was determined from the measurement and analysis of  $V^0$  decays.

There are some distortions of the image of an event on the film due to the optics and to the development of the film. The correction of these distortions is discussed later. (sect. 3.9).

## 2.5 Quality of the film

During the exposure, at the end of each film

(about 1250 pictures), a small sample of film was developed. This was checked for the bubble density, the number of tracks per frame, and the general quality of the picture. As a result of these tests, the beam or the operating conditions of the bubble chamber was adjusted if necessary. In addition to these tests at the time of the exposure, further tests were made on the quality of the film.

#### 2.5.1 No-field film

One roll of film was exposed with the magnetic field of the chamber switched off, and the film was divided among all the laboratories taking part in the experiment. The residual field of the magnet was  $4 \pm 2$  gauss.

A sample of 95 beam tracks from this film, chosen close to the axis of the camera to avoid difficulties due to optical distortions were measured on a precision microscope. The film was set in the stage so that the track lay roughly along the x-axis of the stage, and for 30 equally spaced positions in the x-direction, the displacement of the track in the y-direction was measured accurately to about one micron. To each of these tracks, a curve was fitted of the form:

$$y = a_0 + a_1 x + a_2 x^2$$

In addition to fitting the curve to the complete track, a similar curve was fitted to the first 20 points of the track, the middle 20 points, and to the last 20 points. The co-efficients  $a_0$  and  $a_1$  depend only on the positioning of the track in the microscope stage. The co-efficient  $a_2$  is, to a very good approximation, given by:

$a_2 = 1/2r$ , where  $r$  is the radius of curvature of the track on the film.

For tracks in a chamber without magnetic field, this should of course be zero, and for beam tracks in the residual field of the chamber  $a_2$  should be  $+ .2 \times 10^{-5} \text{ cm}^{-1}$ . The sign of  $a_2$  obviously depends on the choice of axes but on this system if the field were switched on, positively charged tracks would have  $a_2$  positive.

The mean values of  $a_2$  are set out in the table below.

| Table 2          |                                 |
|------------------|---------------------------------|
| points fitted    | $a_2$ ( $\text{cm}^{-1}$ )      |
| all 30 points    | $(-4.7 \pm 1.2) \times 10^{-5}$ |
| first 20 points  | $(-6.7 \pm 1.5) \times 10^{-5}$ |
| middle 20 points | $(-6.7 \pm 1.9) \times 10^{-5}$ |
| last 20 points   | $(-2.3 \pm 1.8) \times 10^{-5}$ |

There is a significant bias towards negative curvature which is certainly not due to the residual field of the chamber. The effect is slightly less towards the end of the track. The result of this bias on the measurement of a beam track would be to overestimate its momentum by about 0.6%.

A possible explanation of this bias is that there is some distortion due to motion of the chamber liquid in the time between the entry of the beam and the firing of the flash tubes (about 1ms.). Relative motion of the liquid of a few cm./sec. would produce an effect of this magnitude.

To check the effect of this bias on the measurement and re-construction of tracks a further test was made on the no-field film. 93 beam tracks which interact near the end of the chamber were selected and measured on a digitised measuring table (about 8 or 9 points per track). The tracks were re-constructed by the programme Thresh (See section 2.9). The corrections for optical and other distortions were included in Thresh. The mean value of  $1/\rho$  where  $\rho$  is the radius of curvature of the track in the chamber was  $(0.7 \pm 0.3) \times 10^{-5} \text{ cm}^{-1}$ . The corresponding value of  $a_2$  is  $-(6 \pm 3) \times 10^{-5} \text{ cm}^{-1}$  in agreement with the values obtained by microscope measurements. The standard deviation of  $1/\rho$  was  $(2.7 \pm 0.2) \times 10^{-5} \text{ cm}^{-1}$ .

The systematic error ( $0.7 \times 10^{-5} \text{ cm}^{-1}$ ) is rather smaller than this, so its effect will not be very important.

The maximum detectable momentum is defined to be the momentum at which

$$1/p = \Delta(1/p) \quad (\Delta = \text{standard deviation})$$

The m.d.m. is then  $160 \pm 10 \text{ GeV/c}$ .

### 2.52. Fiducial point measurements

The disadvantage of the above test is that only the no-field film can be examined, and if faults had occurred at some other time during the exposure, these would not be detected. The programme Reap was used to calculate the quantities  $R_1$  and  $R_2$  in each view for a few events measured in each film, where

$$R_1 = (d_{4,7}/d_{11,16})^2, \quad R_2 = (d_{7,16}/d_{4,11})^2$$

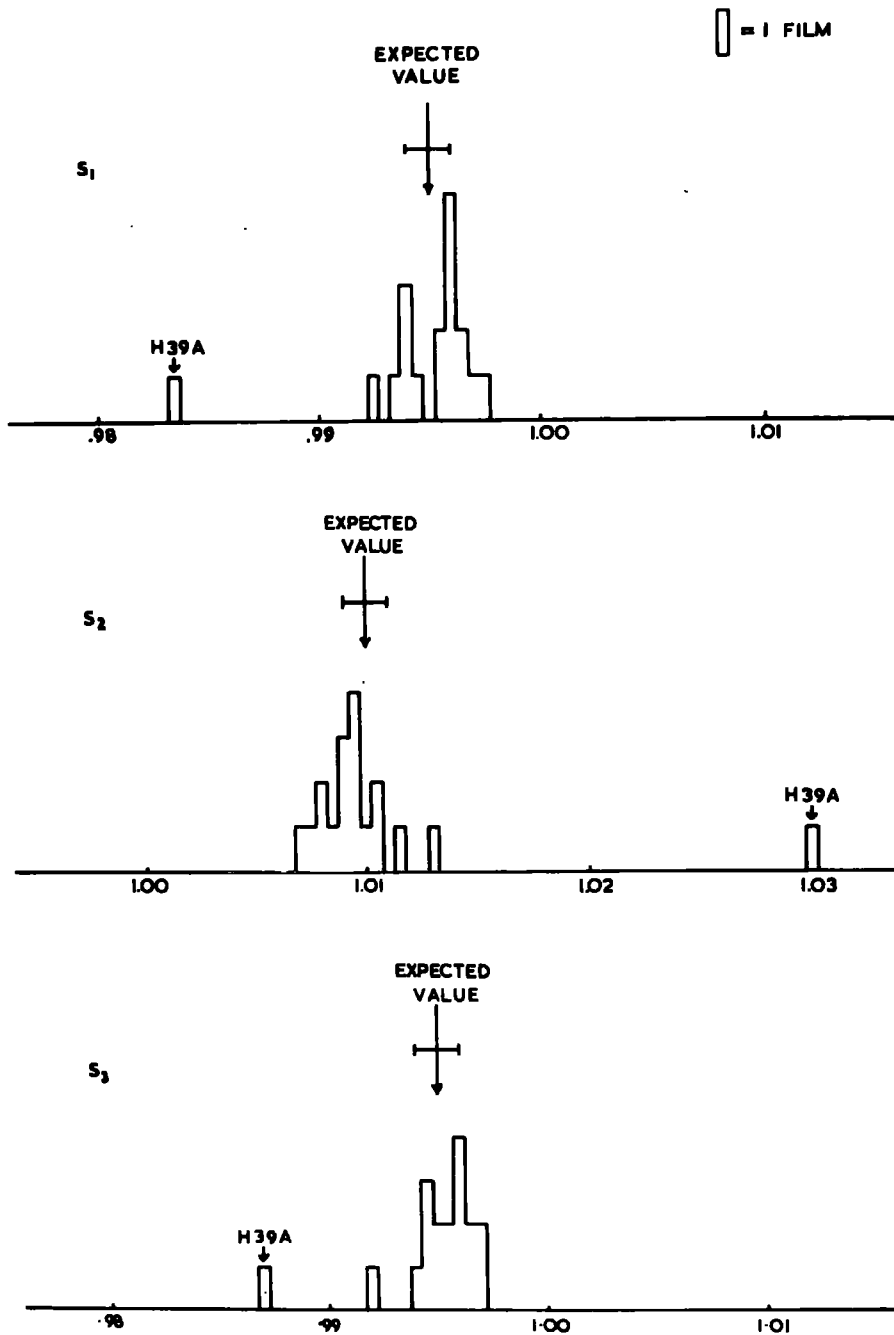
and  $d_{4,7}$  is the distance between fiducial marks 4 and 7, and so on. The median of each set of values was taken to obviate error due to inclusion of an incorrect measurement. The unit of digitisation is different in the x- and y- directions on two of the measuring machines so the quantities  $R_1$  and  $R_2$  are dependant on the measuring machine. To compare films measured on different machines the quantities  $S_1, S_2, S_3$  were defined as follows:-

$$S_1 = \frac{\text{mean } (R_1, R_2 \text{ for view 2, } R_1, R_2 \text{ for view 3})}{\text{mean } (R_1, R_2 \text{ for view 1})}$$

and similarly for  $S_2$  and  $S_3$ .

The distribution of these quantities is shown in fig. 7, and the expected values of the quantities from the known apparent positions of the fiducial marks is indicated. The standard error of setting on a fiducial point was found by repeated setting on a cross, and the corresponding standard error on  $S_1, S_2$  and  $S_3$  is shown. More care may have been taken whilst testing the setting accuracy than would be taken in the normal course of measuring events, so this is probably an underestimate of the error. On most of the films, there is reasonable agreement with the expected values of  $S_1$ , but the film H39A has values which are in poor agreement. It was also found to be difficult to reconstruct events measured on this film. The reason for this is probably that the film was not being sucked flat on the glass plates in one of the cameras at the time that these pictures were taken.

FIG. 7 TEST OF FIDUCIAL MARK SYSTEM



## CHAPTER 3

### ANALYSIS OF THE FILM

#### 3.1 Introduction

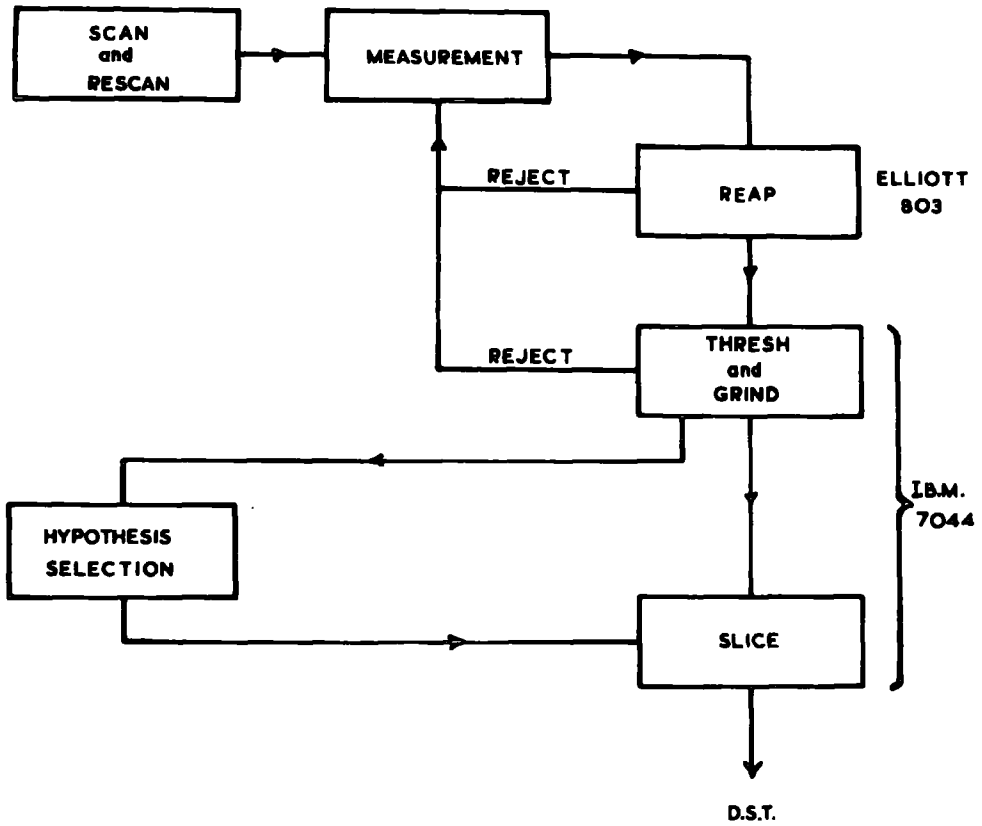
This chapter describes the system used for the analysis of the film, which is much the same as that used by most groups engaged in the analysis of bubble chamber film.

The system is shown schematically in fig. 8. The film was scanned and events of the type to be obtained were selected. The events were measured on digitised measuring tables, and the measurements, punched on paper tape, were analysed on the Elliott 803 computer by the programme REAP. At this stage events which were obviously wrongly measured were rejected and remeasured. The events were analysed by the CERN T.C. programmes, THRESH AND GRIND, on the I.B.M. 7044 computer at Glasgow University. Events which were found to be badly measured were rejected and remeasured. The well measured events were classified and the data summary tape (D.S.T.), a magnetic tape containing the information for every event, was prepared. A statistical analysis of the sample of events was made, using the D.S.T.

#### 3.2. Scanning

Of the 25 films in Durham, six were rejected after a preliminary scan due to poor visibility,

FIG. 8



SYSTEM OF DATA ANALYSIS

or to too many tracks on each frame. The remaining 19 films were scanned by a physicist and a scanner on views 1 and 2, using view 3 in cases of doubt. The scanning volume is the area of ABCD shown in fig. 6, as seen in view 2, the requirement being that the beam track should be seen to enter the region through the side AB and that the interaction should take place inside it. All types of event were scanned for, and for each event found, the frame number, the number of the event on the frame, the number of charged secondaries of the interaction, and whether any charged decays or possible associated neutral decays were observed. The approximate position of the event was recorded, by noting the section of the base line where the beam track entered the zone in which the interaction took place as shown in fig. 6. This was used to help identification of the events at a later stage. Recognised stopping protons were recorded so that a range measurement could be made. Other features such as secondary interactions, associated  $\gamma$ 's, Dalitz pairs, or pion decays were also noted.

Eleven of the films were rescanned on the same view, but only the frame number, the number of prongs, and whether there were any charged decays or neutral decays were recorded. The comparison of the results of the two scans was used to estimate

the efficiency of scanning as described below. The discrepancies between the two scans were checked on the scanning table so that lists of events for measurement would be correct.

### 3.3. The efficiency of scanning

In estimating the efficiency of scanning, it is assumed that the process of scanning is a statistical one, that is, that for any event on the film, there is a certain probability of finding the event. It is further assumed that this probability is the same for all events of the same type, and that it remains constant throughout the scan, although the probability of finding an event in the rescan may be different from that of finding it in the first scan.

Suppose that:

$P_1$  = probability of event being found in first scan.

$P_2$  = probability of event being found in second scan.

and that in a sample of film there are  $N$  events.

Then:

no. of events found in first scan =  $P_1 N = n_1$

no. of events found in second scan =  $P_2 N = n_2$

no. of events found in both scans =  $P_1 P_2 N = n_{12}$

Thus efficiency of scan =  $P_1 = n_{12}/n_2$

and efficiency of rescan =  $P_2 = n_{12}/n_1$

In eleven films, 3553 4 prong events were found in the first scan. In the second scan, 3542 were found, of which 3432 had also been found in the first scan. With the above assumptions, the efficiency of the first scan is 96.9% and of the second scan, 96.6%. A further eight films were scanned once only, and 2242 4 prong events were found. It is assumed that the efficiency of scanning these films is also 96.9%.

### 3.4 The length of track scanned

For ten consecutive frames in every 100 frames, the number of tracks were counted which entered the scanning volume through AB and left by CD. The number of tracks leaving the side of the scanning volume, BC, were counted, and a frequency distribution of the zone in which the track left was found. From these the mean length of beam track per frame was estimated, taking the median length of track for each zone for tracks leaving the side of the scanning volume. The number of tracks which leave by the side is small, so such an approximation is justified. The length of tracks travelling the full length of the volume was taken to be the length of the scanning volume at the mean depth of incoming beam tracks. The curvature of beam tracks, and their inclination to the length of the chamber make no significant difference to this length. Corrections were made for interactions inside

the volume and for muon contamination of the beam. The length of track which was scanned was  $1.59 \times 10^5$  metres.

### 3.5 Selection of events for measurement

All four prong events without an associated  $V^0$  decay that were found by the scan and rescan were listed for measurement, with the exception of those interactions with a secondary interaction or a charged particle decay at a short distance from the primary apex. Events with a recognised stopping proton whose range was to be measured were noted. To aid the identification of an event, the zone number in which the event occurred was recorded, together with any feature of the event which may have been noticed in the scanning, for example, secondary interactions or  $\gamma$ 's.

### 3.6 Measurement of Events

The events were measured on three machines of the film plane digitised type which had been made in the department. On two of these machines, the film stage could be moved in the x-direction, and the projecting lens in the y-direction, the movement of these being digitised by a Moiré fringe system. The film was projected on a vertical screen on which was marked a small reference point. The measurement of a point on the film consisted of aligning the point on the reference spot and pressing a button, the

value of the coordinates of the point being output on eight track paper tape in the form shown in fig. 9(a). The parity hole was punched on the tape as necessary so that each character had an even number of holes. The correct state of the counters for these machines was displayed on a set of lights, so that, by resetting on a known point, it was possible to check that there had been no fault in digitisation during measurement. This check was performed at the end of the measurement of each view.

On the third machine, the stage moved in both the x- and y- directions and the motion was digitised mechanically. The form of output of the coordinates is shown in fig. 9(b). This is a decimal form of output, with the exception that for the two least significant digits, the code is reflected when the next most significant digit is odd, as shown in fig. 9(c). The reason for that is that, at each step, only one contact of the mechanical digitiser changes, so that, at the transition, a completely incorrect value of the coordinate is not registered.

Each machine had a typewriter keyboard by which characters in Elliott eight-track code could be punched on the paper tape. These were used to insert information about the event, to label the measurements and to be used as control characters, for example,



as erasure, end of event, etc.

Each event that was measured was labelled for identification with the film number, the frame number and the number of the event on the frame. For reference, the date of measurement, the measurer and the machine on which the event was measured were also recorded.

The events were measured on each of the three views. In each view, wherever possible, the four fiducial crosses, 7, 4, 22, and 16, shown in fig. 6, were measured. In parts of the film, where one of these crosses was not clearly visible on a view, the other three of the fiducial marks only were measured. The apex of the interaction, about eight or nine points along each track, and the end point of the track of

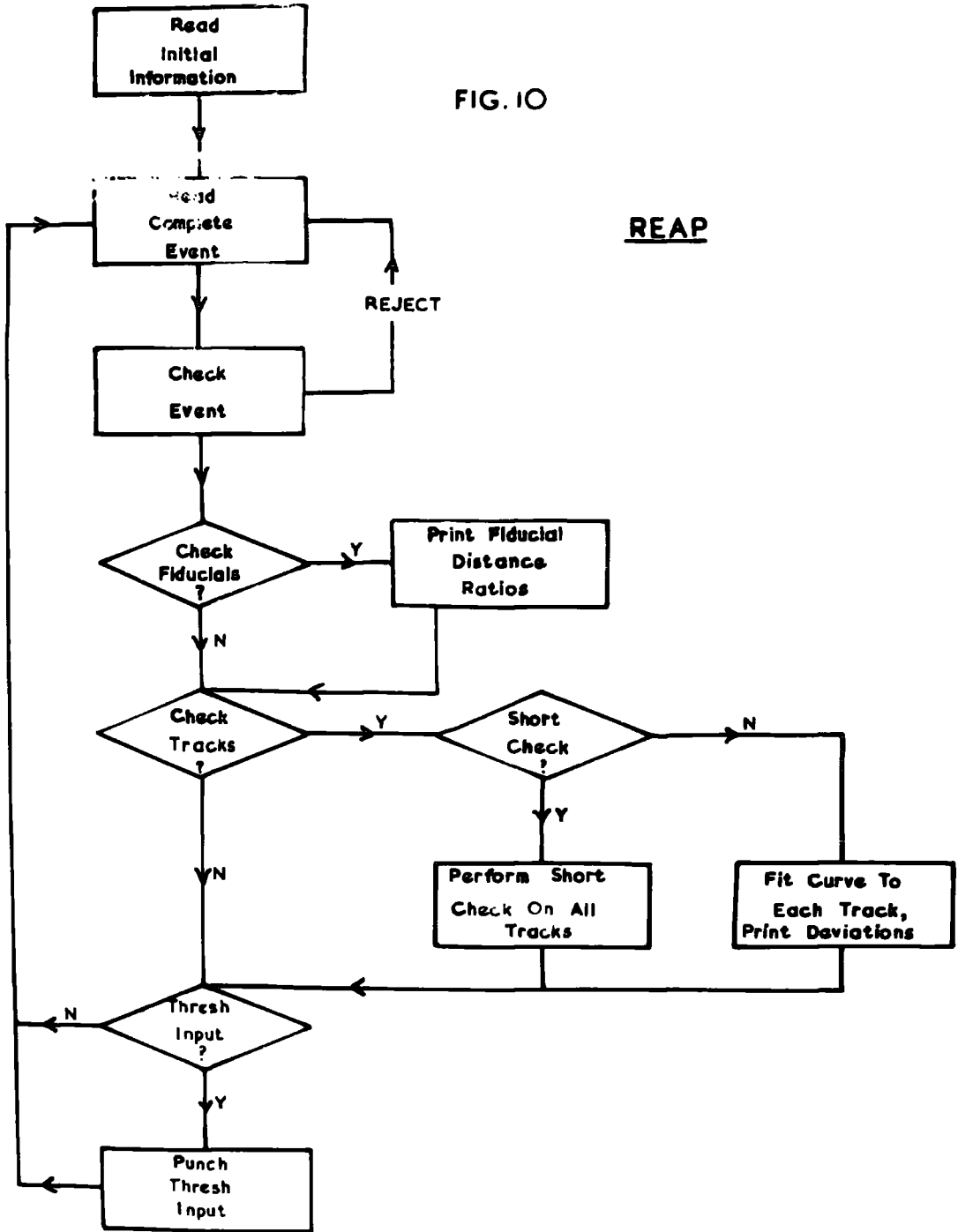
a recognised stopping proton where appropriate, were measured. In those events in which the range of the proton was less than about 1cm., the end point of the track was measured, but no measurements along the track were made.

### 3.7 Reap

The output tapes from the measuring machines were analysed by a computer programme, called REAP, which was written by the author for the Elliott 803. The general structure of this programme is shown in fig. 10. The information read in initially consisted of the experiment number, the labels of the

FIG. 10

REAP



fiducials that were to be measured, a list of the labels which could be used for tracks and points, and information concerned with the running of the programme.

In reading an event, the programme would first read the event number, together with other information which may have been punched and then start to read measurements. A coordinate pair was recognised by the previously read view number and label, so the measurer would be able to remeasure any track by repeating it, and a single point on a track could be erased. If a label was read which had not previously been used on that event, it was only accepted if it was in the list of permitted labels. This was so that, should a fault have occurred in punching the tapes, co-ordinates would not be recognised as a label.

When an event had been read in, it was checked for completeness. The event was rejected unless each point and track had been measured in at least two views. For this purpose, a view was only considered if at least three fiducial crosses had been measured in that view. If the event was accepted it was then punched on five track paper tape in the standard Thresh input format.

In addition, the programme could perform tests on the measured fiducial crosses and tracks, and these were applied from time to time to check the quality of the measurements.

### 3.8 Tests in Reap

#### 3.8.1 Check on fiducial marks

In each view where the four fiducial marks had been measured, the following quantities were calculated and printed:-

$$1) R_1 = (d_{4,7}/d_{11,16})^2 \quad 2) R_2 = (d_{7,16}/d_{4,11})^2$$

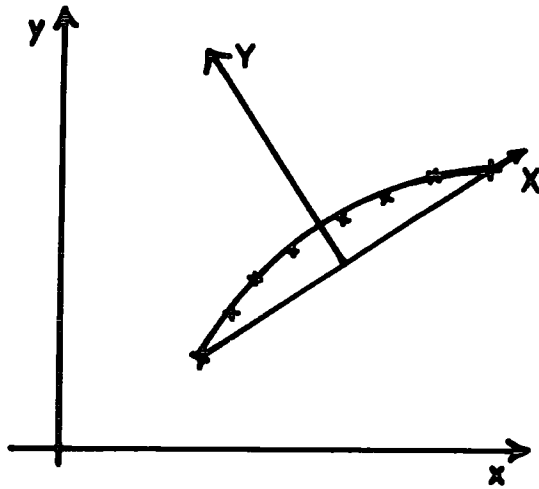
Where  $d_{4,7}$  is the distance between the fiducial marks 4 and 7 and so on.

The standard fractional error expected on such a ratio is about  $10^{-3}.E$ , where  $E$  is the standard error, on  $x$  or  $y$ , in measuring a point, in the units of digitisation, about two microns. Thus, if the fiducial marks are set to an accuracy of two units of digitisation ( $4\mu$ ), the ratio should be constant to about 0.2%.

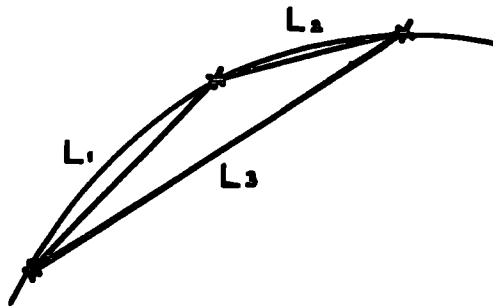
#### 3.8.2 Check on track measurements

This test was performed on each track that had been measured in the event. The measurements of each track were first transformed into the X,Y system of co-ordinates shown in fig. 11(a). That is, the X-axis passed through the first and last point measured, and the origin was half-way between these points. A parabola of the form,  $Y = AX^2 + BX + C$ , was then fitted to these points such that  $\sum [Y - (AX^2 + BX + C)]^2$  was a minimum. The deviation of each point from the fitted curve,  $Y - (AX^2 + BX + C)$  was printed.

FIG. II REAP TRACK CHECKS.



a) REAP - Transformation of track measurements for checking



b) REAP - Short check on track measurements

### 3.8.3. Short check on track measurements

For each set of three consecutive measurements along each track (i.e. points 1, 2, 3; points 2, 3,4; etc.), the quantity  $(L_1 + L_2 - L_3)/(L_1 \cdot L_2 \cdot L_3)$  was calculated. (See fig 11(b)). Assuming that the track turned through a small angle over the three consecutive points, this quantity is approximately  $1/8r^2$ , (See appendix A.) where r is the radius of curvature of the tracks. So for a curve of constant curvature, the calculated quantity should be constant. Consecutive values of this parameter were compared, and if any pair disagreed by more than a certain value, the test was considered to have failed, and in such cases, the test described in the previous section was performed for that track.

### 3.9 Thresh

This programme was used to reconstruct the events in space. The measurements of the fiducial marks on each view are used to set up a reference system for all the measurements. The measurements are transformed to their apparent positions on the liquid surface of the camera side window. The transformed measurements of the fiducial marks are compared with their known position to check the quality of the measurements. If any fiducial mark fails this check, all the measurements for the corresponding view are rejected.

The measurements are corrected for distortion by applying a transformation of the form

$$\begin{bmatrix} X' \\ Y' \end{bmatrix} = (1 + \alpha_1 x + \alpha_2 y + \alpha_3 xy + \alpha_4 x^2 + \alpha_5 y^2 + \alpha_6 (x^2 + y^2)) \begin{bmatrix} X \\ Y \end{bmatrix}$$

Where X, Y are measured co-ordinates in the reference plane, relative to the optic axis

X', Y' are the transformed measurements;

$$x = X/d;$$

$$y = Y/d;$$

and d is the distance of the camera from the reference plane.

The co-efficients  $\alpha_1$  and  $\alpha_2$  are corrections for the distortions produced by film tilt. The other co-efficients correct the optical distortions and distortions produced during the development of the film. The co-efficients are dimensionless, and so the correction is independent of the units of the measuring machine. The values of the co-efficients used were based on those supplied by Kellner (17). As an illustration of the effect of this transformation, a correction of about 0.1mm. is made by the  $\alpha_1, \alpha_2$  terms at about 20cm. from the optic axis, by the  $\alpha_4, \alpha_5$  terms at about 45 cm. from the optic axis, and

by the  $\alpha_3, \alpha_6$  terms only in the extremes of the chamber.

Points were reconstructed in space using the three measurements, and an estimate of the accuracy was made. Where the reconstruction was bad, the point was reconstructed from the two best measurements, or not reconstructed at all. For each track measured, checks were made on the points measured, and inaccurate points were rejected. The tracks were reconstructed by fitting a helix to each one, and estimating the errors on the parameters of each helix.

### 3.10 Grind

This programme was used to test several hypotheses for each event, and to perform kinematic fitting. The magnetic field at several points along the track is calculated, and an average value used to determine the momentum of the track. The measured momentum of the beam is compared with the known beam momentum, and a weighted average was taken. The following hypotheses were tested against the event, each possible assignment to the positive tracks being made.

- 1)  $\pi^+ p \longrightarrow p \pi^+ \pi^+ \pi^-$
- 2)  $\pi^+ p \longrightarrow p \pi^+ \pi^+ \pi^- \pi^0$
- 3)  $\pi^+ p \longrightarrow p \pi^+ \pi^+ \pi^- \eta^0$
- 4)  $\pi^+ p \longrightarrow n \pi^+ \pi^+ \pi^- \pi^-$
- 5)  $\pi^+ p \longrightarrow p \pi^+ K^+ K^-$

In hypothesis 3), the  $\eta^0$  must decay to neutral particles ( $\eta^0 \rightarrow 2\gamma$ ,  $\rightarrow \pi^0 2\gamma$ , or  $\rightarrow 3\pi^0$ ). If it had decayed into a charged mode ( $\eta^0 \rightarrow \pi^+ \pi^- \pi^0$ ), the event would have been observed as a six pronged interaction. A study has been made of six pronged interactions in this sample of film (19). The cross-section for the interaction 3) was estimated to be  $100 \mu\text{b.}$  and as 70% of the decays of the  $\eta^0$  are to neutral particles, one would expect the cross-section for this interaction in four-pronged events to be  $70 \mu\text{b.}$

If a track had been labelled as stopping, the range was used as a measurement of momentum, depending on the mass of the particle assigned to the track. Otherwise, the momentum was determined from the curvature of the tracks. For each successful hypothesis, the measured quantities were fitted so as to give conservation of energy and momentum.

The variation of magnetic field that was used was determined by Blum (16). The central value of the magnetic field was assumed to be 13.46 kgauss

which was that found by D. Z. Toet by measuring the decays of  $\Lambda^0$ 's and kaons. The beam momentum was taken to be 4.996 GeV/c, determined by D. J. Schotanus, from the fitted momentum of a sample of events with unambiguous four-constraint fits.

A card was punched for each successful hypothesis, containing the event number, the number of the hypothesis, and the sequence number of the event on the Grind Library Tape, the magnetic tape output of Grind containing all the measured quantities and the results of the calculations. A similar card was also punched for every event, but with the hypothesis number left blank. The use of these cards to select the well measured events and the correct hypothesis is explained in section 3.13.

### 3.11 Acceptance of events after Grind

From the printed output of Grind, each event was checked for errors detected during Thresh and Grind. If the errors were too serious, as set out in the table below, the event was rejected and remeasured.

Table 3

Rejection Criteria

| Error  | Action  |
|--|---|
| 1 Complete failure of a track in Thresh.                 | Event rejected.   |
| 2 No convergence in fitting a helix to a track in Thresh | Event rejected unless momentum < 400 MeV <u>or</u> dip > 60°.   |
| 3 Momentum <u>and</u> direction inaccurate               | Same as for error No. 2.  |
| 4 Momentum <u>or</u> direction inaccurate.               | Event rejected if more than two such tracks.                    |
| 5 Straight track.  | Event rejected unless this is a beam track or a stopping track. |

The errors 2 and 3 were not taken to be a reason to reject an event if they occurred on steep tracks or tracks of low momentum, which are difficult to reconstruct. In the errors 3, 4, and 5, the terms "inaccurate" and "straight track" have the meanings described below.

$p$  = momentum,  $\lambda$  = dip,  $\phi$  = azimuthal angle.

$\epsilon_{\text{int.}}(1/p)$  = internal error on  $1/p$  (similarly,  $\epsilon_{\text{int.}}(\lambda)$ ,  $\epsilon_{\text{int.}}(\phi)$ ).

$\epsilon_{\text{ext.}}(1/p)$  = external error on  $1/p$  (similarly,  $\epsilon_{\text{ext.}}(\lambda)$ ,  $\epsilon_{\text{ext.}}(\phi)$ ).

The internal errors are calculated by Thresh, based on the deviation of measured points from the fitted track. The external errors are calculated by Grind, and are the expected errors on the track parameters, depending on the length of the measured track, the track parameters, and the known measurement error. The terms used in the above table are then defined as follows:-

|                        |  |
|------------------------|--|
| "Inaccurate momentum"  | $\epsilon_{\text{int.}}(1/p) > 3 \times \epsilon_{\text{ext.}}(1/p)$             |
| "Inaccurate direction" | $\epsilon_{\text{int.}}(\lambda) > 3 \times \epsilon_{\text{ext.}}(\lambda)$     |
|                        | <u>or</u> $\epsilon_{\text{int.}}(\phi) > 3 \times \epsilon_{\text{ext.}}(\phi)$ |
| "Straight track"       | $1/p < 3 \times \epsilon_{\text{ext.}}(1/p)$                                     |

### 3.12 Acceptance of hypotheses

All events which had been successful in Grind, whether there were any hypotheses accepted or not, were examined on the scanning table. For each of the positive tracks in the final state, an "ionisation code" was determined as follows:-

0 if the track was definitely not a proton.

1 if the track could be a proton.

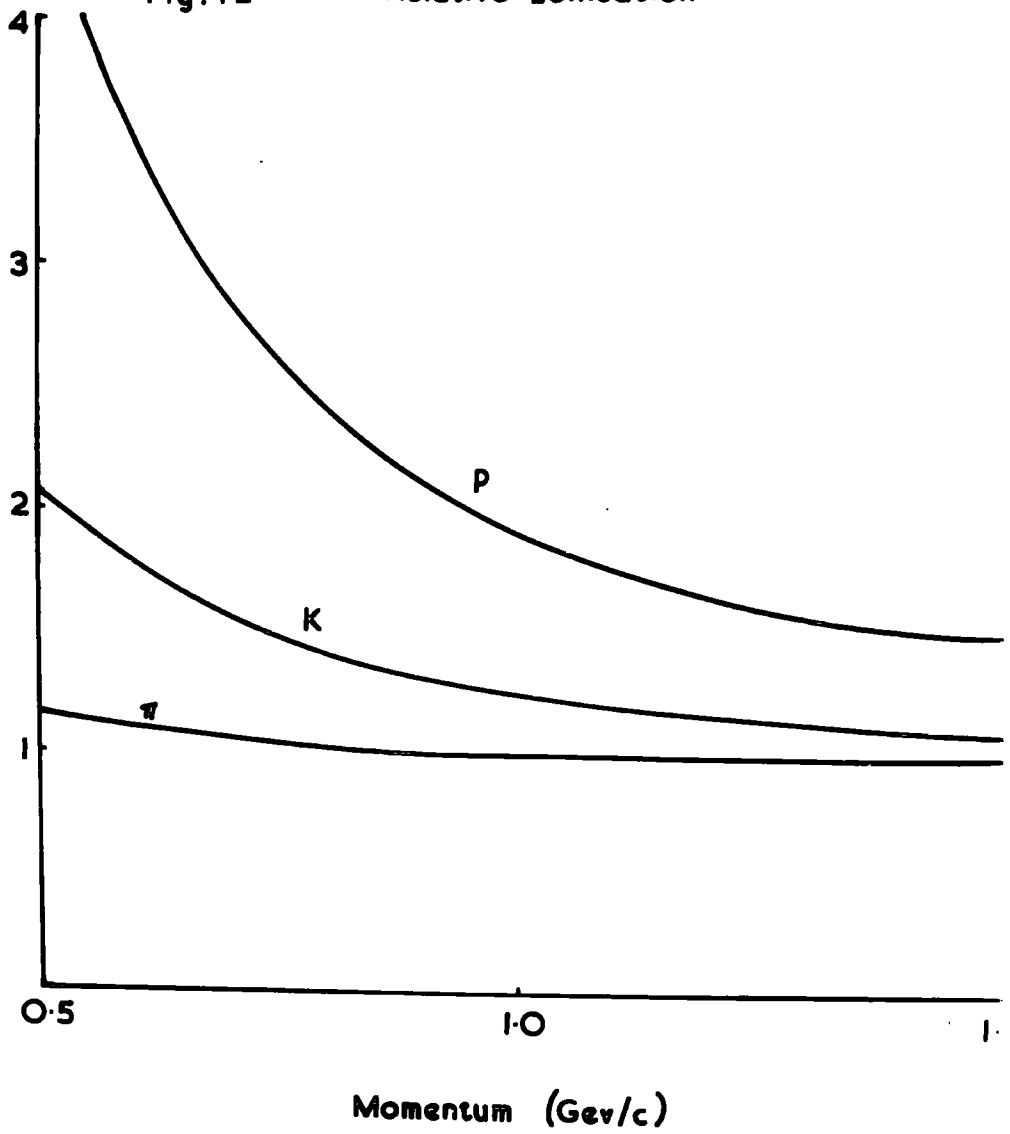
2 if the track was definitely a proton.

The decision was made by comparing the bubble density of the track and its momentum with the curves in fig. 12, which are calculated as  $1/\beta^2$ . It can be seen that it was possible to make a definite decision on a track if its momentum was less than 1.3 - 1.5 GeV/c. Further, not more than one of the tracks could be a proton, so if one was identified as a proton, the others were given the code 0, that is, definitely not a proton, even if the momentum was so high that a decision made on ionisation was impossible.

A fitted hypothesis was accepted only if it was compatible with the ionisation of all the tracks.

Fig. 12

Relative Ionisation



An acceptance limit on  $\chi^2$  was imposed as follows:-

fits with 4 degrees of freedom,  $\chi^2 \leq 24$

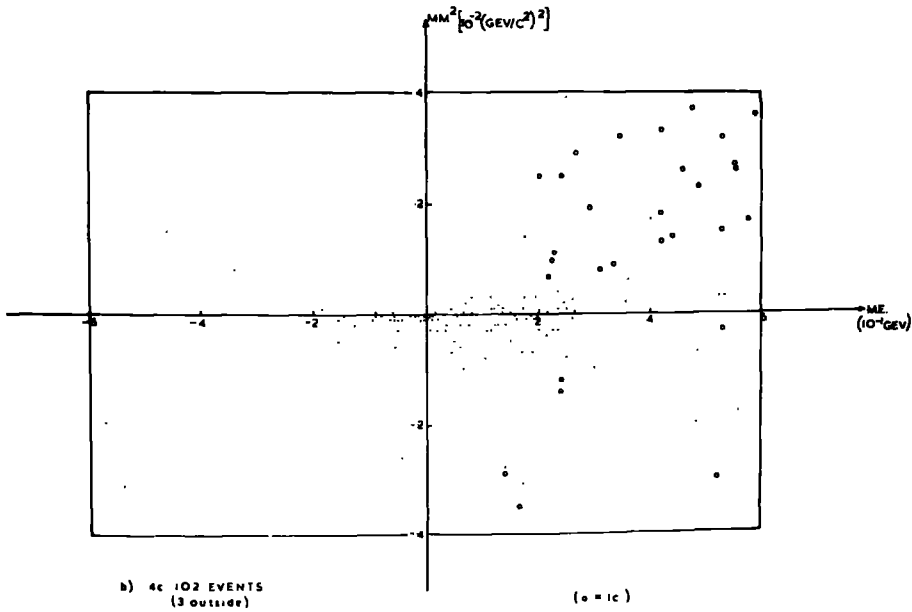
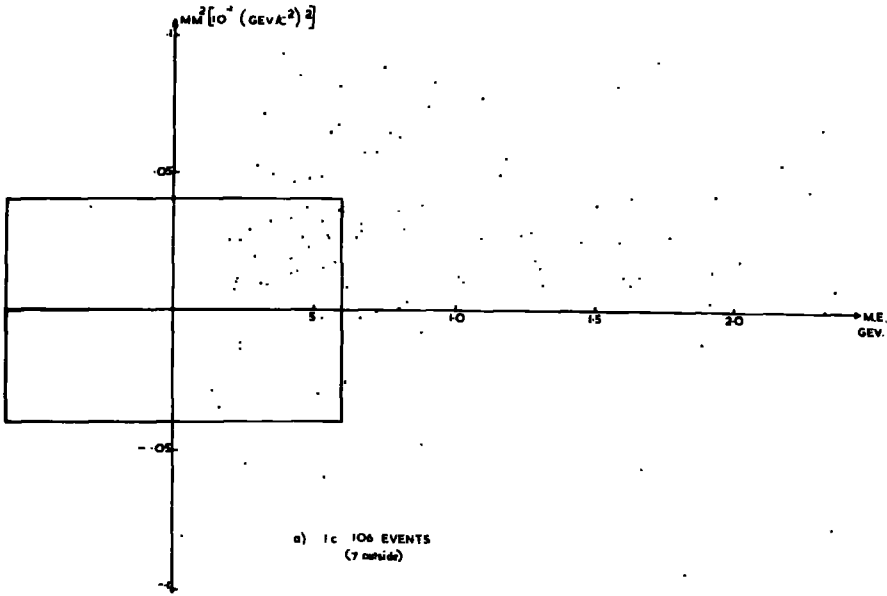
fits with 1 degree of freedom,  $\chi^2 \leq 6$

In addition, if both a 4-constraint fit and a 1-constraint fit were acceptable, the 4-constraint fit only was taken. A calculation based on a random generation of events had shown this to be valid for an earlier experiment, and so the same process was adapted here. As a confirmation of the validity of this procedure, a graph was plotted of  $(M.M.)^2$  versus M.E. for a small sample of 4-constraint (4C) fits and a small sample of 1-constraint (1C) fits (missing  $\pi^0$ ). (fig. 13).

M. E. is the energy of the assumed missing particle, based on measured quantities.  $(M.M.)^2$  is the square of the mass of the assumed missing particle.

Clearly, the points corresponding to 4C fits occupy a very small area of this graph, in contrast to those corresponding to 1C fits. One might make the simple assumption that an event with a missing  $\pi^0$  would produce a successful but false 4C fit if  $(M.M.)^2$  and M.E. were in the region normally occupied by events with no missing

FIG. 13 PLOTS OF MISSING MASS SQUARED AGAINST MISSING ENERGY



neutral particle. On this assumption, the probability that a  $\pi^0$  event would be wrongly classified is not more than 1%.

### 3.13 The data summary tape

The data from the different laboratories were collected together on magnetic tape. Each laboratory produced a tape called the DST, containing the selected parts of the output Grind. This tape was in a standard format for each laboratory, and this was thus the stage at which all the different systems of analysis became compatible. From these tapes, using the CERN programme, Slice, a data summary tape containing various calculated quantities was produced for each reaction.

The DST was produced for the Durham data from the Grind library tape and the cards produced by Grind. From these cards, the cards corresponding to the selected events and hypotheses were selected as follows. For an event with one or more accepted hypothesis, the cards containing the appropriate hypothesis number were taken, and for a no-fit event, the card without a hypothesis number was selected. The cards were arranged in the same order as the events occurred on the Grind library tape. On the first (or only) card for each event, the ionisation code was

punched. A computer programme was used to produce the DST<sub>i</sub> from these cards and the Grind library tape.

The DST<sub>i</sub> contained for each event a record of the geometry of the event followed by, for each accepted hypothesis (if any), a record of the fitted event. The geometry record contained details of the measured parameters of each track and the vertex and of the errors on these quantities, the ionisation code, and the square of the missing mass for the three possible assignments of  $p\pi^+\pi^+\pi^-$  and the assignment  $\pi\pi^+\pi^+\pi^-$  to the four charged secondary tracks. The record of the fit included the fitted parameters of each track and their errors, details of the fit including the  $\chi^2$  of the fit, and the square of the mass of the missing neutral particle calculated from measured quantities.

The programme Slice was used to produce, from the DST<sub>i</sub>'s, a data summary tape for each reaction, containing details of the event and of the fit, together with the effective mass, the four-momentum transfer from both the incoming proton and the incoming pion, and the components of momentum in the overall centre of mass system, for all possible combinations of final state particles.

A statistical analysis of the data on the D.S.T. was made using the programme SUMX, which can present the result in the form of a histogram or a two-dimensional scatter plot. Some of the plots presented here have been produced by a similar, more simple programme on the 7044.

CHAPTER 4

PRELIMINARY EXPERIMENTAL RESULTS

4.1 Cross-sections

4.1.1 The 4-prong cross-section

The 4-prong cross-section was calculated for each laboratory taking part in the experiment. Different laboratories had different methods of determining the total track length scanned, and for some the track length would be uncertain by about 5%. The track length was corrected for muon contamination and for absorption (i.e. the reduction in the track length due to interactions taking place in the scanning volume. The continuation of the beam track to the end of the volume must be subtracted from the calculated length of track.

The number of 4-pronged interactions that were found was corrected for the efficiency of scanning. The density of hydrogen used in this calculation was the density at 27°K and at saturation pressure, 0.0611. The variation of the density with pressure is negligible but the density varies with the temperature by about 3% per degree. The uncertainty in the temperature contributes to the uncertainty in the cross-section. The calculated cross-sections are listed in the table below:

Table 4

| 4-prong cross-sections (mb.) |      |
|------------------------------|------|
| Bonn                         | 9.3  |
| Durham                       | 11.0 |
| Nijmegen                     | 11.7 |
| Paris                        | 10.6 |
| Strasbourg                   | 9.6  |
| Turin                        | 10.5 |

The mean value of these was taken, which gives for the cross-section for 4-prongs  $10.5 \pm 0.5$  mb.

#### 4.1.2 Fitted Hypotheses

The distribution of the fitted hypotheses for 3307 events measured in Durham is given in table 5.

The distribution for the other laboratories is much the same, except that there are some discrepancies in the number of ambiguities. These differences could be due to differences in the accuracy of measurement or to differences in assessing to what accuracy the ionisation of a track could be determined. It is shown in section 4.1.3 that these differences in the number of ambiguities do not lead to discrepancies in the cross-sections.

Table 5

Distribution of fitted hypotheses

| Reaction  | Number of Events |
|---|------------------|
| A) $\pi^+ \rho \rightarrow \rho \pi^+ \pi^+ \pi^-$        | 762              |
| B) $\pi^+ \rho \rightarrow \rho \pi^+ \pi^+ \pi^- \pi^0$  | 829              |
| C) $\pi^+ \rho \rightarrow \rho \pi^+ \pi^+ \pi^- \eta^0$ | 210              |
| D) $\pi^+ \rho \rightarrow n \pi^+ \pi^+ \pi^+ \pi^-$     | 218              |
| E) $\pi^+ \rho \rightarrow \rho \pi^+ K^+ K^-$            | 37               |
| NO FIT  | 953              |
| <b>Ambiguities</b>  |                  |
| A-A   | 6                |
| A-E   | 1                |
| E-E   | 2                |
| B-B   | 5                |
| B-C (1)   | 122              |
| B-C (2)   | 3                |
| B-D   | 15               |
| C-C   | 1                |
| C-D   | 99               |
| 3 1-C fits  | 44               |

The two letters specify the interaction type of each fitted hypothesis when specifying the ambiguities. The ambiguities of the type B-C are further subdivided:-

- 1) Those in which the identity of the charged particles is the same in the two fitted hypotheses.
- 2) Those in which the identity of the charged particles is different.

The entry for threefold ambiguities includes all events for which any three hypotheses were accepted. All except a few of these are of the type B-C(1)D. There were no events in the Durham data for which three 4-C fits were accepted, but there were a few in the complete sample of events.

The number of events of type C, 210, would correspond to a cross-section for that type of about  $650 \mu\text{b}$ , and correcting for other decay modes of the  $\eta^0$ , about  $1\text{mb}$ . If some of the ambiguous events were also included the calculated cross-section would be even more. Yet, it is known from the analysis of 6-prongs that the cross-section for the process is only  $100 \mu\text{b}$ . Clearly most of the events accepted as type C are in fact no fit events. The cross-sections were calculated only for the remaining four reactions.

4.1.3 Channel cross-sections

For the purpose of calculating the cross-sections, cuts were imposed on the samples of 1-C events as described in section 4.2.

Further, in the case of ambiguities not resolved by the above criteria, the hypothesis was selected for which  $\chi^2$  was the lowest. The error introduced by this last step is not likely to be significant.

As a first step in calculating the cross-sections the percentage of events of the type A was calculated for each laboratory, and these are shown in the table below.

Table 6

Percentage of type A fits

|            |      |
|------------|------|
| Bonn       | 26.9 |
| Durham     | 23.3 |
| Nijmegen   | 26.2 |
| Paris      | 25.6 |
| Strasbourg | 25.5 |
| Turin      | 26.0 |

The values agree to within the expected standard deviation (about 1 - 1.5%). The mean value of 25.6  $\pm$  1.0% was accepted.

For channel B, the ratio of the number of events to the number in channel A was calculated for each laboratory. The values are consistent and are set out in the table below.

Table 7

Ratio of type B fits to type A fits

|            | B/A  |
|------------|------|
| Bonn       | 1.07 |
| Durham     | 1.07 |
| Nijmegen   | 1.05 |
| Paris      | 1.10 |
| Strasbourg | 1.10 |
| Turin      | 1.03 |

The mean value is 1.07, and the percentage of events of type B is then 27.4  $\pm$  1.0%.

The percentage of events of types D and E were calculated in the same way. The values for the different laboratories are consistent, and are for channel D, 8  $\pm$  1%, and for E, 1.3  $\pm$  .3%. The corresponding cross-sections are shown in the table below.

Events of reaction B have been randomly generated, and  $\approx$  1% have been found to give a spurious fit of

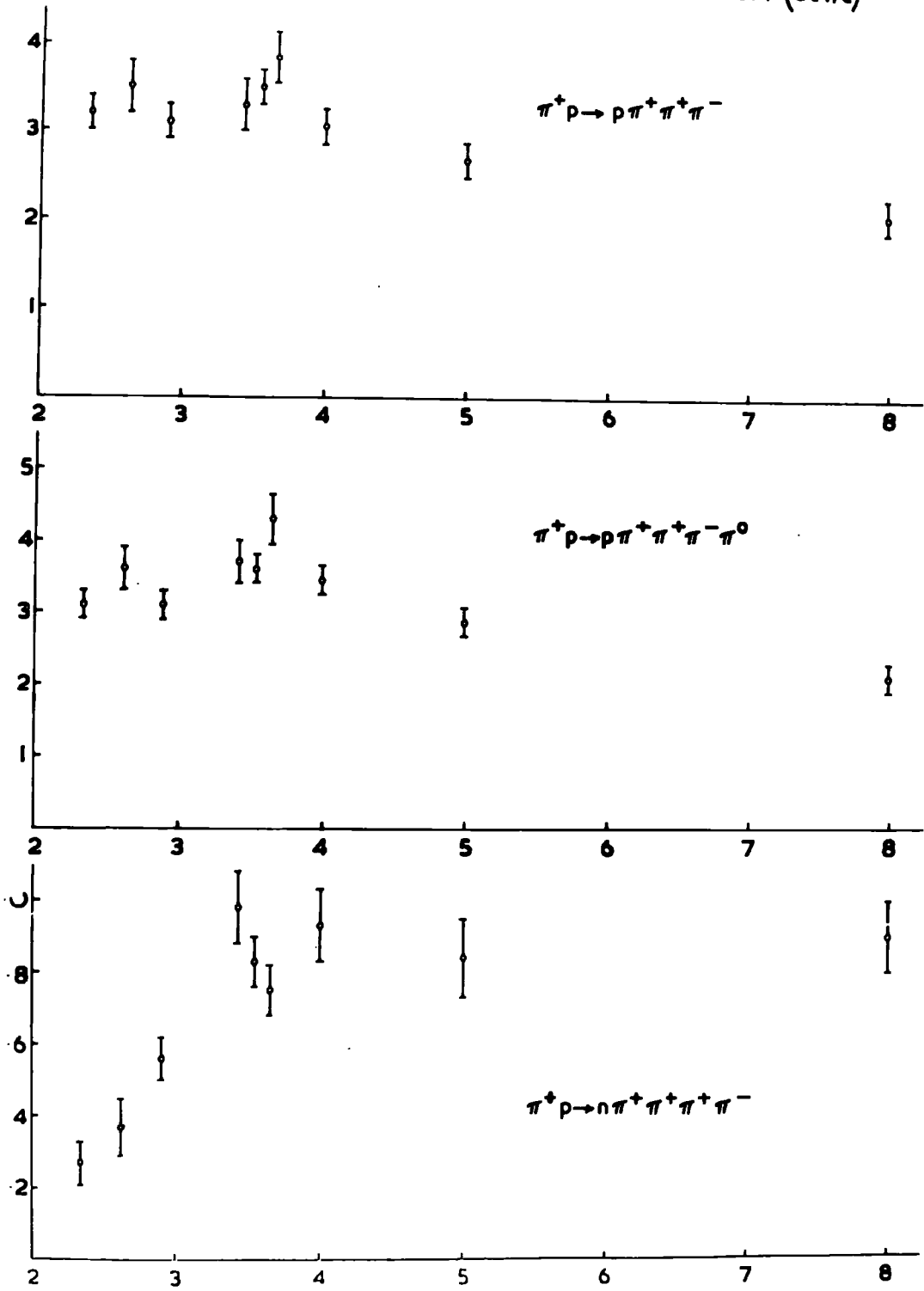
reaction E. This corresponds to about 20% of the events classified as belonging to reaction E. On the other hand, of randomly generated events of reaction E, 70% were found to give a fit of type B, and so the acceptance of the four constraint fit in preference to the one constraint fit was felt to be justified. The cross-section for reaction E has been corrected for the spurious fits. The cross-sections for channels A, B and D are compared with the cross-sections for different incident pion momenta in fig. 14 (Refs. 19-23).

Table 8  
Reaction Cross-sections

|   | ( $\bar{m}$ b. ) |
|---|------------------|
| 4-prongs                                      | 10.5 $\pm$ .5    |
| A) $\pi^+p \rightarrow p\pi^+\pi^+\pi^-$      | 2.69 $\pm$ .17   |
| B) $\pi^+p \rightarrow p\pi^+\pi^+\pi^-\pi^0$ | 2.88 $\pm$ .18   |
| D) $\pi^+p \rightarrow n\pi^+\pi^+\pi^+\pi^-$ | 0.84 $\pm$ .11   |
| E) $\pi^+p \rightarrow p\pi^+K^+K^-$          | 0.11 $\pm$ .04   |

FIG. 14

$\pi^+p$  CROSS SECTION (mb) vs. INCIDENT PION MOMENTUM (Gev/c)



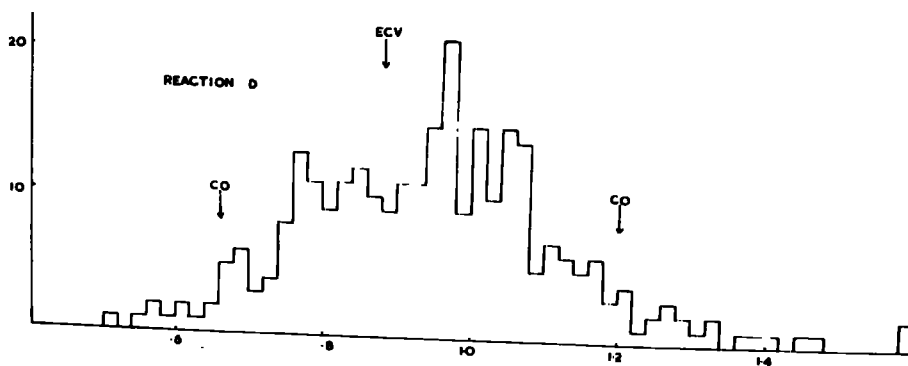
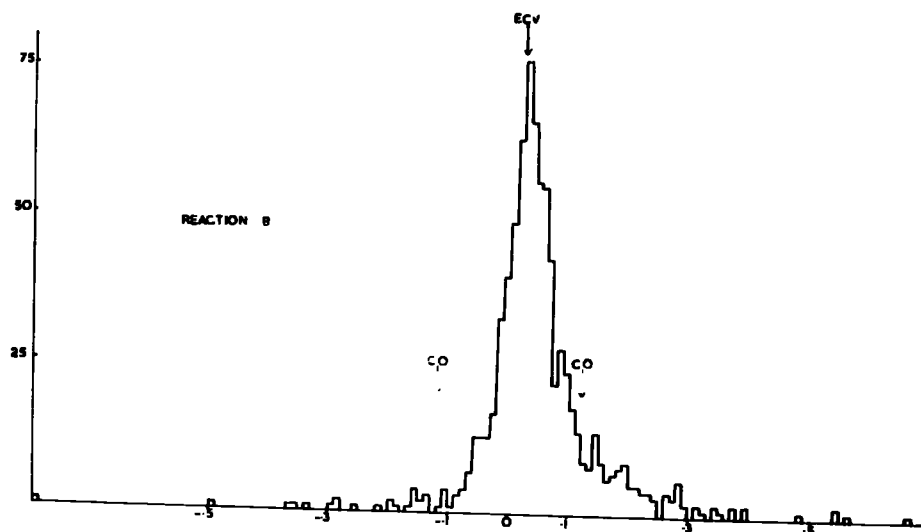
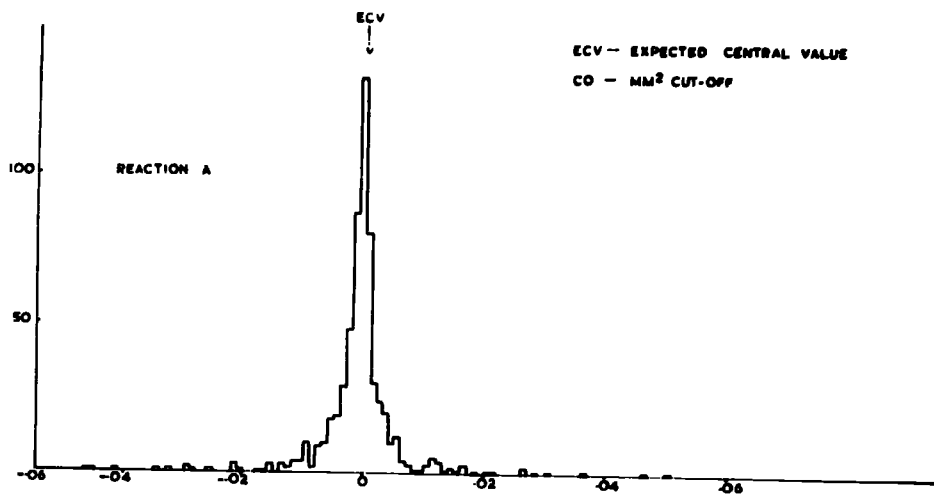
#### 4.2 Distributions of the square of the missing mass ( $MM^2$ )

Fig. 15 shows the distributions of  $MM^2$  for the reactions A, B, and D. In each case the position of the expected central value, being the square of the mass of the missing neutral particle, is indicated.

Fig. 15(a) shows the distribution of  $MM^2$  for reaction A, in which no neutral particle is produced so the expected central value is zero. It can be seen, however, that there is a small but significant shift in the peak of about  $.0005(\text{GeV}/c^2)^2$  in the negative direction. The reason for this shift can be understood as follows. Suppose that there was an error in the measurement of the momentum of one track only, of  $\delta p_x$ . This would then be the missing momentum of the event. The corresponding missing energy would be  $\beta_x \delta p_x$ , where  $\beta_x$  is the velocity of the track with the error. The missing energy is therefore less than the missing momentum, i.e.  $MM^2$  is negative. An error in the measurement of the direction of a single track would give a non-zero value for the missing momentum, but the missing energy would be zero. Again the result would be to calculate  $MM^2$  negative. Thus if the error in the measurement of any single quantity results in a negative value of  $MM^2$ , one would expect that the combination of all errors would result in

Fig. 15

Distributions of (missing mass)<sup>2</sup> [(GeV/c<sup>2</sup>)<sup>2</sup>]



a shift towards negative values of  $MM^2$ .

Fig. 15(b) and (c) show the  $MM^2$  distributions for reactions B and D respectively. The distributions have a large number of events which are far from the central value. It is likely that a large proportion of these events do not correspond to the relevant reaction, but have nevertheless given a reasonable fit to the hypothesis. In order that these incorrectly assigned events should not contaminate the sample, limits were set on the values of  $MM^2$  which would be accepted, as follows

|            |                       |
|------------|-----------------------|
| Reaction B | $-0.12 < MM^2 < 0.12$ |
| Reaction D | $0.66 < MM^2 < 1.2$   |

The positions of these limits are shown in fig. 15. Events in which  $MM^2$  was outside the prescribed limits were excluded from the calculation of the cross-sections and from the analysis of the reaction. A test was made on the validity of the above restriction for reaction B. The distribution of the invariant mass of the supposed  $\pi^+\pi^-\pi^0$  combinations for events which were outside the above limit was examined. The sample contained only about 1%  $\omega^0$  compared with

about 20% in the accepted sample. One concludes that of the excluded sample of events, only about 5% are really events of reaction B.

It can be seen that, on these two distributions, there is an excess of events for higher values of  $MM^2$  than the central value. This is due to the inclusion of some no-fit events, those with more than one missing neutral particle.

#### 4.3 Data consistency

As several different laboratories were each measuring and analysing a sample of events for this experiment, it was necessary to check that the different sets of data were consistent before an analysis was made. The usual test, that of comparing the results of the measurement and analysis by each laboratory of the same small sample of film, was not used in this experiment because of the relatively large number of laboratories taking part. Instead, various checks were made on the data, and the possible effect of any differences between the different laboratories on the physical results were examined. One such check on the consistency of the data, the comparison of the cross-sections and of the distribution of accepted hypotheses has already been described

(sect.4.1). The following checks were also made:

#### 4.3.1 Distribution of $\chi^2$

Fig. 16 shows the distribution of  $\chi^2$  for each laboratory for fits to events of reaction A. Each distribution is normalised to one event. The general shape of the distributions is much the same but it can be seen that there are differences. If the distribution corresponded to the statistically expected distribution of  $\chi^2$  for a four constraint fit, the maximum value of the distribution would be 0.184 occurring at  $\chi^2 = 2$ . The differences between the distributions could be explained by the fact that the different laboratories measure to different accuracies, and all have used the same value for the calculation of  $\chi^2$ . To explain these distributions in this way, the measurement accuracy of no laboratory would be different from the assumed value by more than 20%.

Fig. 17 shows similar distributions for reaction B. The difference between the distributions of different laboratories is not so easily seen as for the four constraint fit. The table below gives the median value of  $\chi^2$  for each laboratory, 0.455 being expected statistically for a one constraint fit.

FIG. 16

$\chi^2$  DISTRIBUTIONS / CHANNEL A

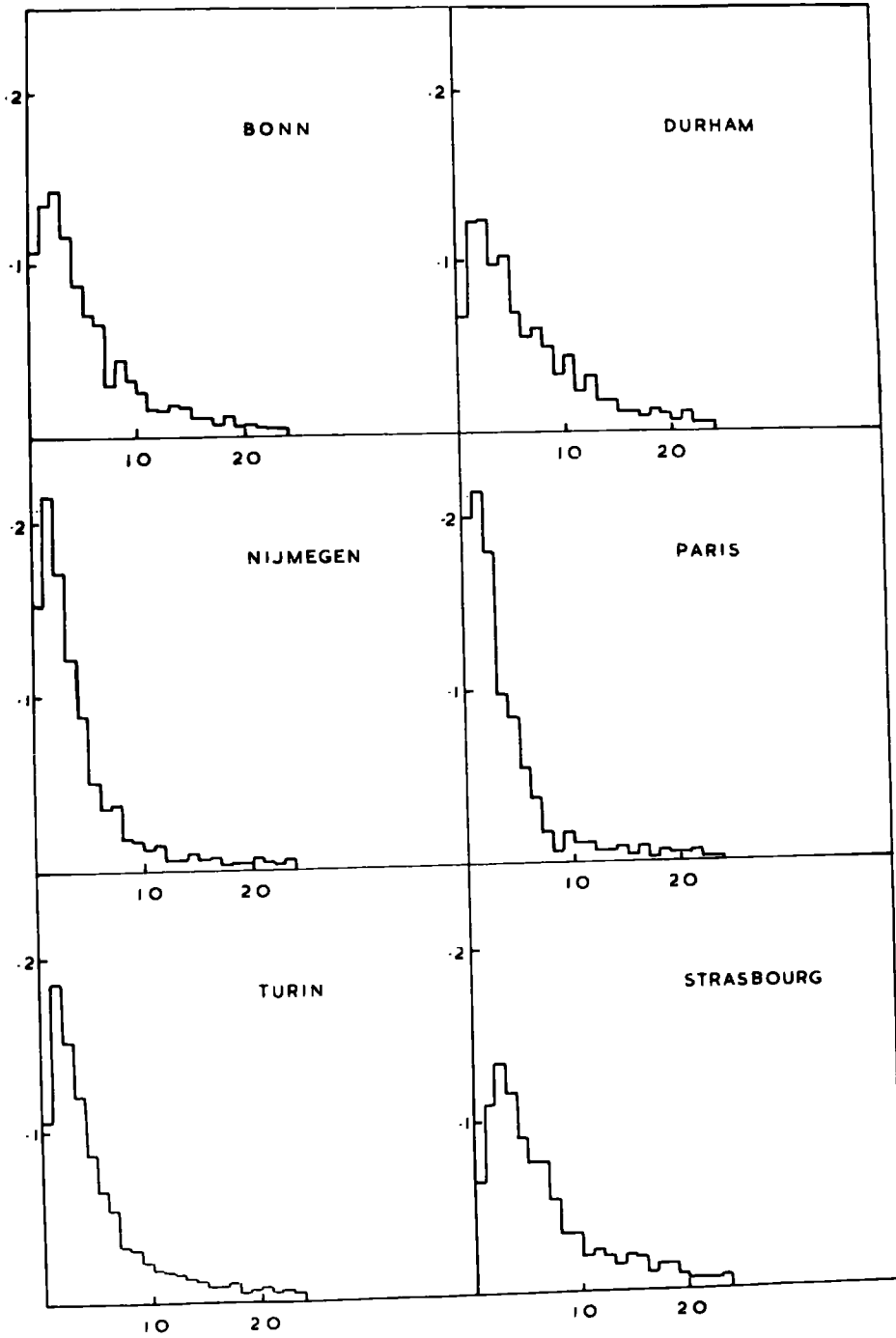


FIG. 17

$\chi^2$  DISTRIBUTION / CHANNEL B

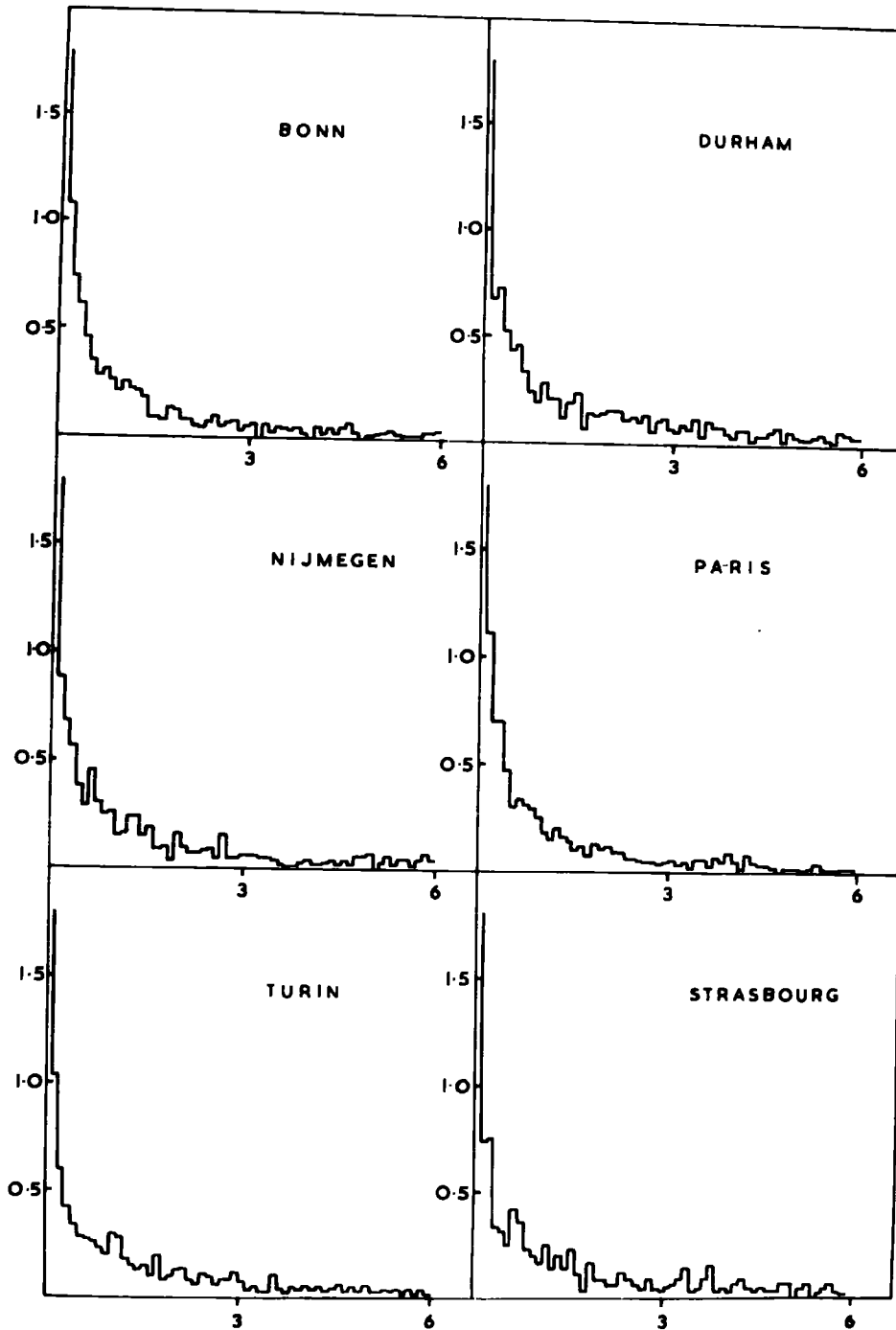


Table 9

|            | Median $\chi^2$<br>for reaction B. |
|------------|------------------------------------|
| Bonn       | 0. 40                              |
| Durham     | 0. 66                              |
| Nijmegen   | 0. 49                              |
| Paris      | 0. 40                              |
| Turin      | 0. 60                              |
| Strasbourg | 0. 67                              |

Assuming the differences in these values to be due to differences in the accuracy of measurement, one again concludes that the measurement error is in no case greater than the assumed value by more than 20%.

#### 4.3. 2 Comparison of invariant mass distributions

To check the effect that the different systems of measurement and analysis might have on the effective mass distributions, the distribution for  $\pi^+\pi^-\pi^0$  from reaction B, plotted in intervals of  $5 \text{ MeV}/c^2$ , was examined. The  $\omega^0$  should appear as a Gaussian distribution as its width is much smaller than the experimental error of measuring effective mass. The central value of the mass of the  $\omega^0$  and the standard deviation of the distribution are shown in the table below for each laboratory.

Table 10  
Comparison of  $\omega^0$  peaks

|            | mass of $\omega^0$<br>MeV/c <sup>2</sup> | standard<br>deviation |
|------------|--|-----------------------|
| Bonn       | 780                                      | 12                    |
| Durham     | 780                                      | 14                    |
| Nijmegen   | 780                                      | 11                    |
| Paris      | 775                                      | 14                    |
| Turin      | 785                                      | 13                    |
| Strasbourg | 775                                      | 17                    |

The standard deviation of the  $\omega^0$  peak shows some variation between the different laboratories, but the differences are not large.

The central value of the peak in each case agrees well with the mass of the  $\omega^0$ , 783 MeV/c<sup>2</sup>.

#### 4.4 Angular Distributions

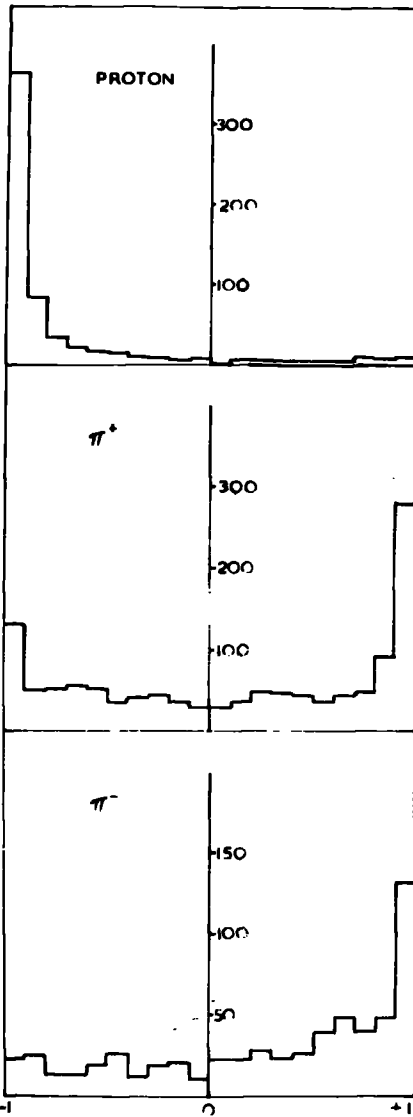
Fig. 18 shows the distribution of  $\cos \theta^*$  for the outgoing particles in reactions A and B, where  $\theta^*$  is the angle between the outgoing particle and the incident pion in the overall centre of mass system.

FIG. 18

DISTRIBUTIONS of  $\cos \theta^*$

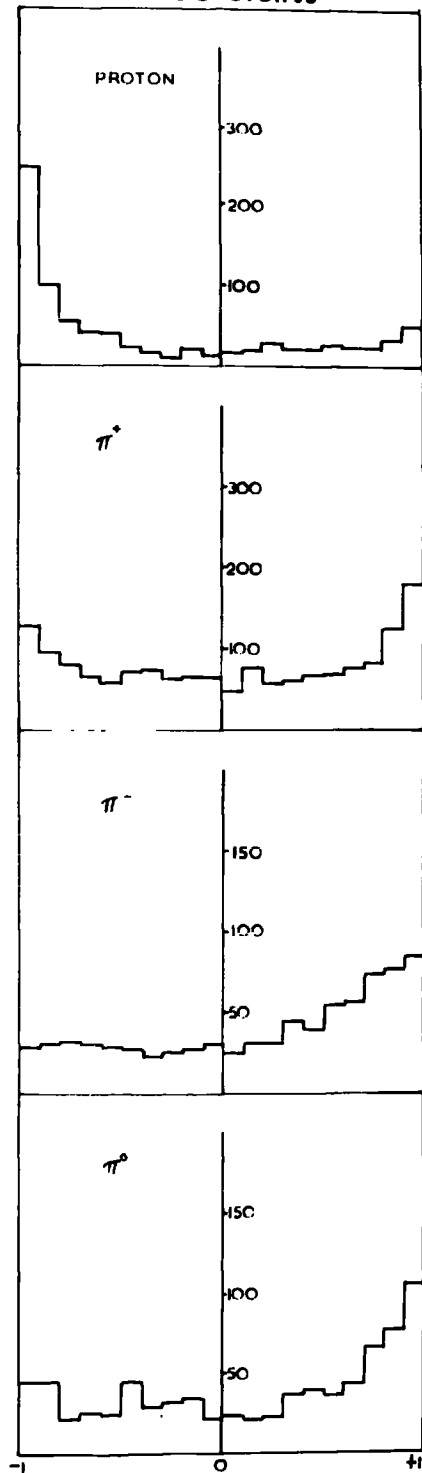
REACTION A

611 events



REACTION B

800 events



In both cases the proton is produced strongly backwards, but there is also a small peak in the forwards direction. The distributions for pions are not so strongly marked, but some peaking in the forward and backward directions is noticed. Comparing the two reactions, it can be seen that the distributions vary more sharply for reaction A than for reaction B. The general distribution of the outgoing particles can be summarised by defining the quantity:-

$$R = (F - B) / (F + B)$$

Where F is the number of particles produced in the forwards direction, and B the number of particles produced in the backwards direction. The values of R are shown in the table below.

Table 11  
Forward - Backward Ratios

|         | Reaction A     | Reaction B      |
|---------|----------------|-----------------|
| Proton  | $-.81 \pm .04$ | $-.37 \pm .035$ |
| $\pi^+$ | $+.15 \pm .03$ | $+.05 \pm .025$ |
| $\pi^-$ | $+.41 \pm .04$ | $+.29 \pm .035$ |
| $\pi^0$ | -----          | $+.18 \pm .035$ |

RESONANCE PRODUCTION5.1 Introduction

In this chapter, resonance production seen in four-pronged interactions is discussed. The main reactions under consideration here are reaction A ( $\pi^+ p \rightarrow \rho \pi^+ \pi^+ \pi^-$ ), and reaction B ( $\pi^+ p \rightarrow \rho \pi^+ \pi^+ \pi^- \pi^0$ ). In addition, resonance production in reaction E ( $\pi^+ p \rightarrow \rho \pi^+ K^+ K^-$ ) is discussed. The only appreciable production of a resonance seen in reaction D ( $\pi^+ p \rightarrow \pi^+ \pi^+ \pi^+ \pi^-$ ) is that of the  $A_2$ , and this is described separately in chapter 6. The sample of events of the remaining reaction ( $\pi^+ p \rightarrow \rho \pi^+ \pi^+ \pi^- \eta^0$ ) has already been shown to contain only a small proportion of correctly assigned events, and this reaction is not discussed.

In each of the three reactions discussed in this chapter, strong resonance production occurs. The  $N^*$  (1236) is a dominant feature of each of these reactions and as this is by far the most commonly occurring  $N^*$  resonance in this experiment, the name " $N^*$ " is used throughout for this particular resonant state, except where confusion might arise. Reaction A is also characterised by the strong production of  $\rho^0$ , particularly in association with an  $N^*$ , and some  $f^0$  and  $A_2$  production is also observed. Resonance production in reaction B is not so strong as in reaction A, but quite strong  $N^*$  and  $\omega^0$  production is

observed, including some associated production of these. Also observed are the  $A_2$ ,  $\eta^0$  and B mesons. Resonance production in reaction E comprises the  $N^*$ ,  $A_2$  (decaying to  $K^+K^-$ ),  $Y^*$  (1520), and  $K^*$  (890).

In order to estimate the cross-sections for resonance production different methods have been tried. These methods are discussed before the description of resonance production in the separate reactions.

## 5.2 Estimation of cross-sections for resonance production.

### 5.2.1 Fowl

Attempts were made to fit effective mass distributions calculated by the computer programme, Fowl, which generates random events and assigns to each one a weight so that the sample is distributed according to Lorentz invariant phase space. Distributions of physical quantities, and correlations of pairs of physical quantities, can be displayed as histograms or as densities on a two-dimensional plot. Resonance production can be introduced by multiplying each weight by a Breit-Wigner function of the form:-

$$\frac{\Gamma}{\Gamma^2 + \frac{(M^2 - M_0^2)^2}{M_0^2}}$$

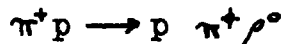
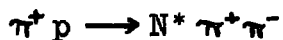
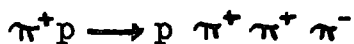
M is the effective mass of the combination of particles under consideration, and  $M_0$  is the mass of the resonance to be generated.  $\Gamma$  is the width of the resonance and, as a first approximation, can be written as a constant. The shape of the resonance is better represented if, instead of a constant, the width is written as suggested by Anderson (24):-

$$\Gamma = \Gamma_0 \left( \frac{p}{p_0} \right)^{2l+1} \frac{0.0436 + p_0^2}{0.0436 + p^2}$$

Where  $p$  is the momentum of the two decay products in their centre of mass system, which is a function of their effective mass.  $p_0$  is then the value of  $p$  for which  $M = M_0$ .  $l$  is the orbital angular momentum of the decay products.

For a narrow resonance, such as the  $\omega^0$ , the shape of the effective mass peak was generated as a gaussian function to represent the distribution of experimental errors.

For reaction A, events of the following four types were generated:-



Attempts were made to fit the experimental effective mass distributions or effective mass scatter plots with an incoherent addition of different amounts of the four reactions. Remembering that the sum of the four fractions must be unity, and that each fraction can not be less than zero, it was found impossible to find anything like a reasonable fit to the data. In particular, the large concentration of points at the bottom right of fig. 19 (or the high mass part of fig. 20.) could not be represented in this way. On fig. 20, the effective mass distribution calculated in Fowl, using for the fractions of the above reactions the values determined as described later, is indicated. A constant width was used to generate the resonances for this, but it was found that the variable width alters only the detailed shape of the peak. It can be seen that the predicted distribution is in very poor agreement with the background. This result is contrary to that obtained for six-pronged events in this film (18)

for which the distributions predicted by Fowl was in reasonable agreement with the experimental data. The procedure in the analysis of six prongs, having found the amount of the dominant processes, was to generate a mixture of events giving these proportions and to look at the effective mass distributions for this mixture. Deviations of the experimental distributions from those predicted by Fowl were examined for possible resonance production. The fact that the distributions predicted for four-prongs are so far from the experimental data clearly indicates that such a procedure applied here could not lead to accurate results.

The calculation of phase space distributions for reaction B was found to be in better agreement with the experimental data, but the discrepancies were still too much to accept the predictions of Fowl as reliable.

The reason for this failure to predict correctly the effective mass distributions is easy to see. For instance, there is no  $t$ -dependence taken into account in Fowl, which assumes all angular distributions to be isotropic. The decay angular distribution of resonances should be introduced too, and these would have to be found experimentally, since the observed

distributions are not the same as would be predicted by a simple OPE model. It would also have been better to include the production of other resonances, such as the  $A_2$  and  $f^0$  in reaction A. The disadvantage of such modifications is that many extra parameters, and a considerable amount of experimental results would have to be brought into the calculation, with a consequent loss of reliability.

### 5.2.2 Empirical background

The second method that was used in an attempt to estimate the cross-sections of resonance production was to approximate the background by an empirical distribution. The form used for the background was:-

$$(M - M_1). P(M)$$

$M_1$  is the minimum possible effective mass (i.e. the sum of the masses of the decay products)

$P(M)$  is a polynomial in  $M$ , the coefficients to be found by fitting. In general,  $P$  was a second or third order polynomial.

The experimental distributions were fitted with the sum of such a background and a Breit-Wigner function, and it was found that good fits could be obtained. The disadvantage of this method can be

seen by considering the distribution of the effective mass of  $p\pi^+$ , in which there is a large  $N^*$  peak close to  $M_1$ . The peak makes it impossible to find the shape of the background at low masses from the experimental distribution, and this must be found from the distribution at high masses and the fact that the background is zero at  $M=M_1$ . The general shape of a distribution of the effective mass of two particles has a vertical slope at  $M=M_1$  according to phase space, and this feature can not be represented by a polynomial. One would therefore expect that the fitted background would be too low when calculated by this method. Another disadvantage of using an empirical background of this form is that a small broad peak could be interpreted as being part of the background. This is particularly true in the case of the  $f^0$  seen in the distribution of the effective mass of  $\pi^+\pi^-$  in reaction A. The strong  $\rho^0$  production makes difficult the estimation of the background in the  $f^0$  region. Indeed in fig. 24(b), the  $f^0$  peak was entirely fitted with a polynomial background, and one would reach the conclusion that there are no backward decaying  $f^0$ 's. The reason for this is that the background for the two distributions of fig. 24 were estimated independently, with the result that different shapes for these were estimated.

Two instances have been pointed out in which a

good fit has been obtained using an empirical background, and from which wrong conclusions would be drawn. Clearly, the use of this method of estimating the cross-sections for resonance production could be dangerous in cases where the behaviour of the background is not so well understood.

### 5.2.3 Estimated Background

In this method, the background, assumed to be smoothly varying, is estimated by eye, with due regard for the expected general shape of phase space distributions. The obvious disadvantage of this method is that it is a subjective one. The advantage that this method has over Fowl is that the background, above which the size of a peak is estimated, is in agreement with the experimental background. The advantages over the polynomial background method are that the estimated background can be made to have the same general shape as the expected phase space distribution, and that backgrounds which are expected to have a similar shape can be made to have a similar shape. For these reasons this method has, with one exception, been used. An allowance has been made for the error in estimating the position of the background in calculating the error on the amount of resonance production. In fact, this error is insignificant in comparison to the statistical error when estimating the size of many of

the peaks. In each case the position of the estimated background is shown on histograms.

In one case the background has been expressed in polynomial form over a limited range. This method was used for the estimation of the mass and width of the B meson, where it was necessary to express the form of the background in terms of a few parameters. In section 5.46 the details of the method used for this are described.

Clearly, since the background is estimated as smoothly varying, resonance production in regions where the background is not smoothly varying can not be discussed. An obvious example of such a case would be the  $A_1$  meson, whose observation is complicated by the Deck effect (25). However, the resonances which are affected in this way are not the strongly occurring ones, and are omitted from the following description of resonance production.

### 5.3 Reaction A

In this section the reaction A (i.e.  $\pi^+ p \rightarrow p \pi^+ \pi^+ \pi^-$ ) is examined. This reaction comprises 5975 events and unless otherwise specified, this is the number of events plotted on all diagrams for this reaction. The reaction is dominated by the production of  $N^*$  and of  $\rho^0$ . In addition, the  $f^0$  and  $A_2^+$  are observed.

### 5.3.1 N\* and $\rho^0$ production

In fig. 19 is shown the scatter diagram of the effective mass of  $p\pi_1^+$  versus the effective mass of  $\pi_2^+\pi^-$ . (The subscripts of the  $\pi^+$  indicate that a different  $\pi^+$  is taken in the two different combinations.) Each event is represented twice on the diagram, corresponding to the two possible choices of the  $\pi^+$  to be combined with the proton. The bands corresponding to the production of N\* and of  $\rho^0$  can be seen clearly. The large concentration of points in the region of the overlap of these two bands indicates the strong double resonance production.

Fig. 20 is the projection of this scatter plot to give a histogram of the distribution of the effective mass of  $p\pi_1^+$ . The peak due to the production of N\* is clearly seen. The number of entries above an estimated smooth background (the continuous line in the figure) is  $3840 \pm 240$  corresponding to a cross-section for the production of N\* of  $1.73 \pm 0.12$  mb., or  $64 \pm 4\%$  of reaction A.

Fig. 21 shows the projection of the scatter diagram to give the distribution of the effective mass of  $\pi_1^+\pi^-$ . The peak due to the  $\rho^0$  can clearly be seen. The number of entries in the peak above the

Fig. 19

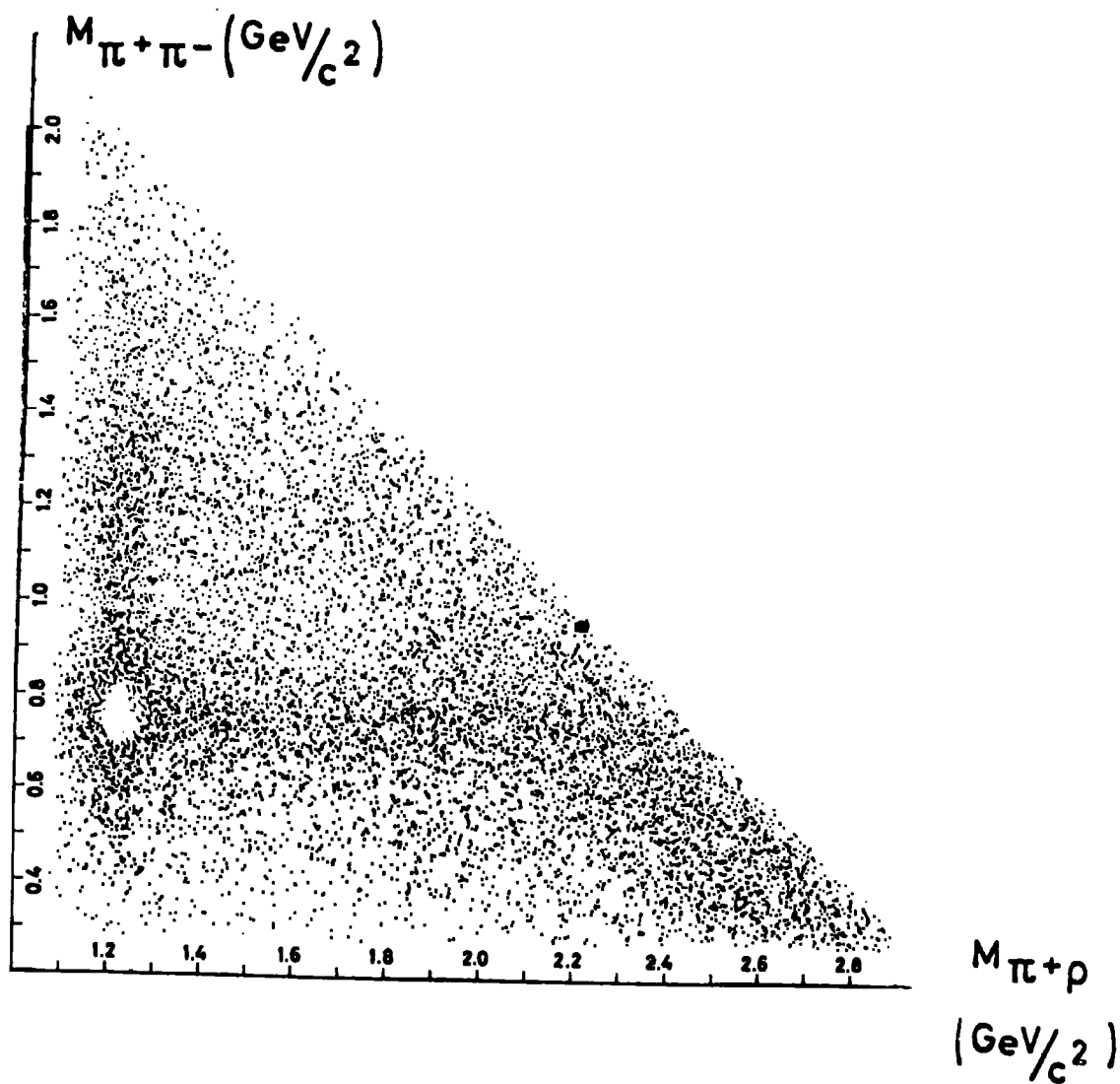


FIG. 20

REACTION A

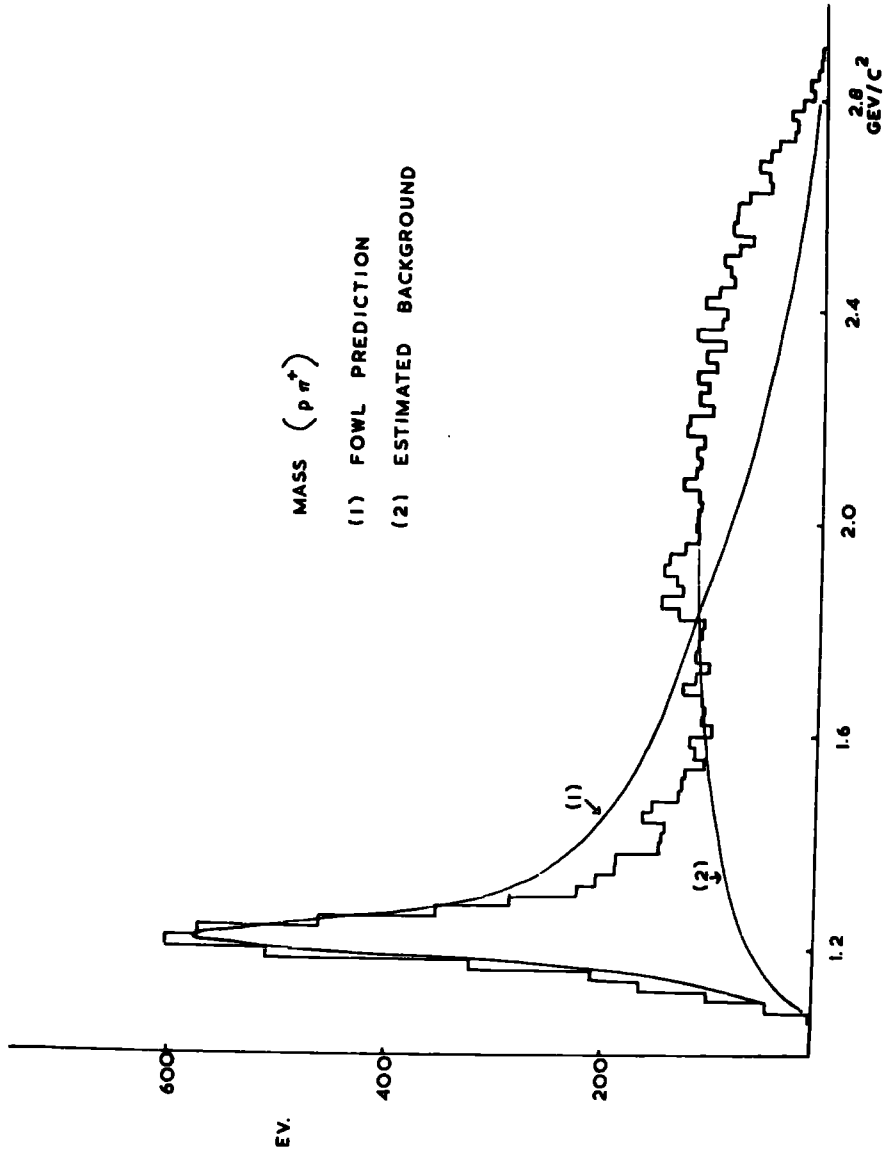
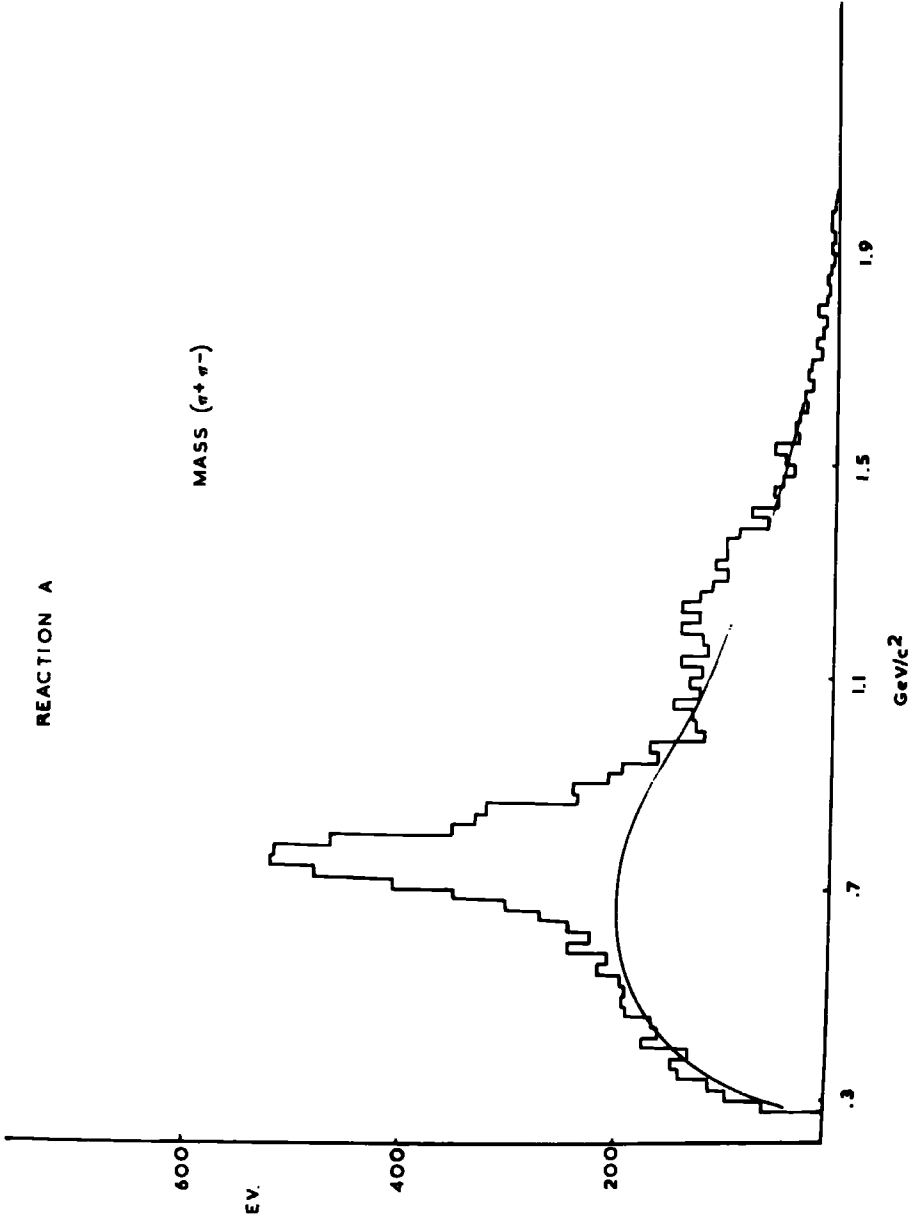


FIG. 21



estimated smooth background is  $3330 \pm 200$  and the cross-section for  $\rho^0$  production is therefore  $1.50 \pm 0.11$  mb., or  $56 \pm 3\%$  of reaction A.

Fig. 22 is the distribution of the effective mass of  $\pi^+\pi^-$  for those events in which the remaining  $\rho\pi^+$  is compatible with an  $N^*$ . For this purpose it was required that the effective mass of the  $\rho\pi^+$  combination should be in the range 1.14 to 1.30 GeV/c<sup>2</sup>. Examination of the distribution shown in fig. 20 shows that about 85% of the  $\rho\pi^+$  combinations selected would be an  $N^*$ . The  $\rho^0$  signal in this selected sample is much stronger than in the total sample, and the number of entries in the  $\rho^0$  peak above the estimated background is  $1250 \pm 120$ . Thus the selected sample contains a  $\rho$  in  $37.8 \pm 3.6\%$  and as the sample is largely of  $N^*\pi^+\pi^-$ , one would conclude that a  $\rho^0$  is produced in association with that proportion of  $N^*$ 's that is the cross-section for the double resonance production process  $N^*\rho^0$  is  $37.8 \pm 3.6\%$  of the cross-section for  $N^*$  production. The cross-section for the production of  $N^*\rho^0$  is therefore estimated to be  $0.65 \pm 0.08$  mb., which is  $24 \pm 3\%$  of reaction A. This value of the cross-section is compared with the value from experiments at other incident pion momenta in fig. 23

FIG. 22

REACTION A

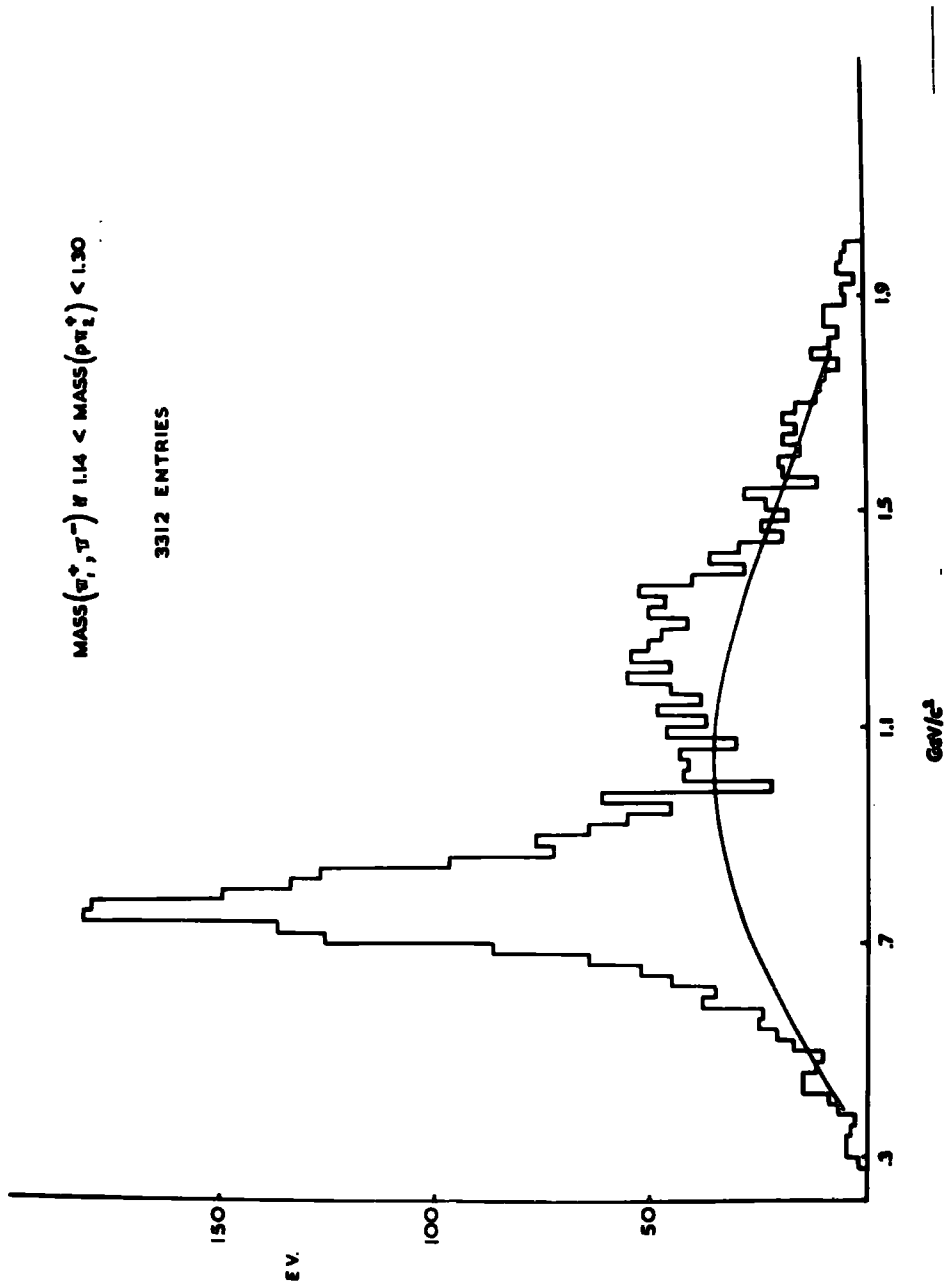
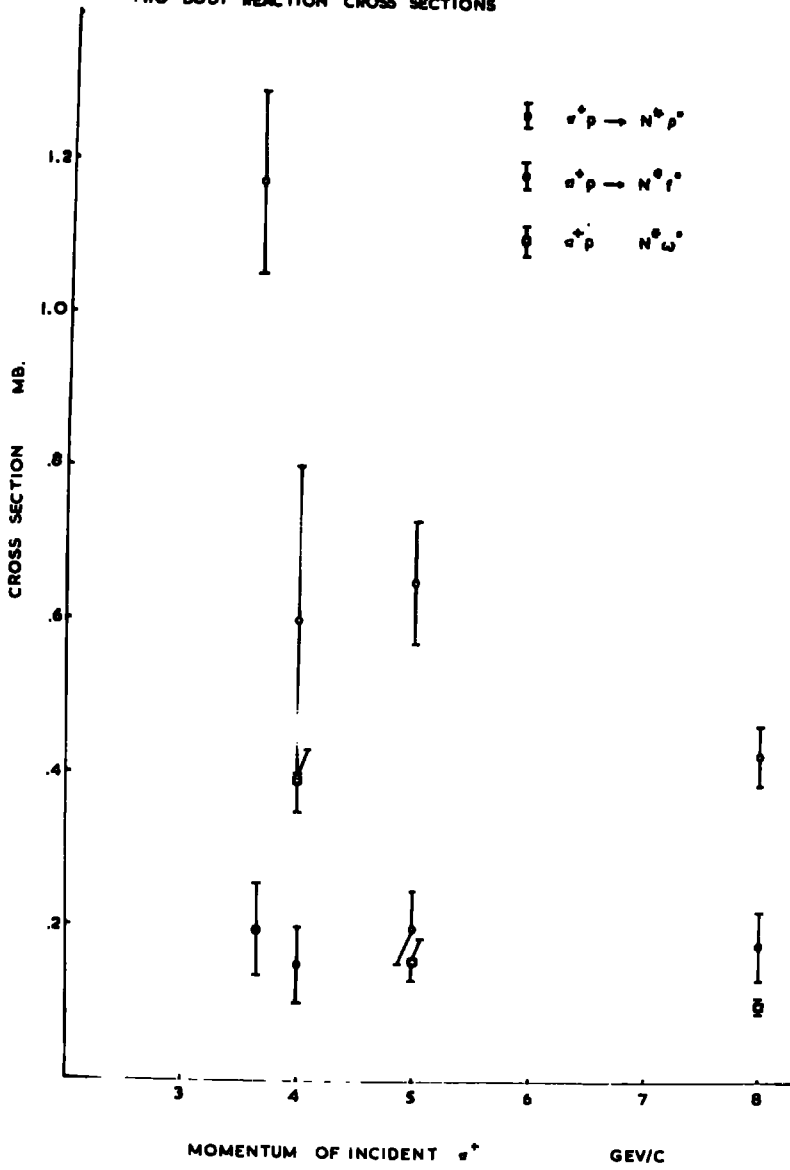


FIG. 23  
TWO BODY REACTION CROSS SECTIONS



### 5.3.2 $f^0$ production

Fig. 19 also shows evidence for  $N^*f^0$  production, although no  $f^0$  band is seen.

The distribution of the effective mass of  $\pi^+\pi^-$  shown in fig. 21. also indicates the presence of  $f^0$  production. An estimation of the number of entries above the background in the region of the  $f^0$  is  $420 \pm 110$ , which corresponds to a cross-section for the production of  $f^0$  decaying to  $\pi^+\pi^-$  of  $0.19 \pm 0.05$  mb. In the distribution of the effective mass of  $\pi^+\pi^-$  associated with an  $N^*$ , fig. 22, the  $f^0$  signal is improved. There are  $260 \pm 70$  entries above the estimated background in the  $f^0$  region which is  $7.8 \pm 2.1\%$  of the sample under consideration. From this one calculates a value for the cross-section for the double production of  $N^*f^0$  ( $\rightarrow \pi^+\pi^-$ ) of  $0.135 \pm 0.035$  mb. As the  $f^0$  has isospin zero, it is predicted by Clebsch-Gordan coefficients that it should decay to  $\pi^+\pi^-$  and to  $\pi^0\pi^0$  in the ratio 2:1. The cross-section for  $N^*f^0$  production is therefore  $0.20 \pm 0.05$  mb. The data is not inconsistent with the statement that the  $f^0$  is produced in association with the  $N^*$  but not separately. The cross-section for the production of  $N^*f^0$  is compared with those from other experiments in fig. 23.

Fig. 24(a) shows the distribution of the effective mass of  $\pi^+\pi^-$  associated with an  $N^*$  where the  $\pi^+$  in the centre of mass system of the  $\pi^+\pi^-$  is produced in the forward direction relative to the incident  $\pi^+$ . Fig. 24(b) shows the complementary distribution where the  $\pi^+$  is produced in the backward direction. The  $f^0$  signal can be seen to be stronger in the first diagram, in which there is an excess of  $190 \pm 30$  events above the estimated background. From the overall spectrum of fig. 22, assuming the usually observed symmetrical decay of the  $f^0$ , one would have expected  $130 \pm 35$  events, and the value obtained is not inconsistent with this. However, the peak for the backward decaying  $f^0$  is certainly broader than that for the forward decaying  $f^0$  and the difference in the appearance of the two peaks does not support the assumption of a symmetrical decay, and is probably the result of an interference with some scattering with odd angular momentum.

### 5.3.3 t dependence of $N^*$ and $\rho^0$ production

Fig. 25 shows the Chew-Low plot for  $\pi^+\pi^-$  systems. The concentration of points in the  $\rho^0$  region at low values of  $|t|$  is very clear. The peripheral production of the  $f^0$  can also be observed on this plot. Selecting

FIG. 24

REACTION A

MASS ( $\pi_1^+ \pi^-$ ) IF  $1.14 < \text{MASS}(\rho \pi_2^+) < 1.30$

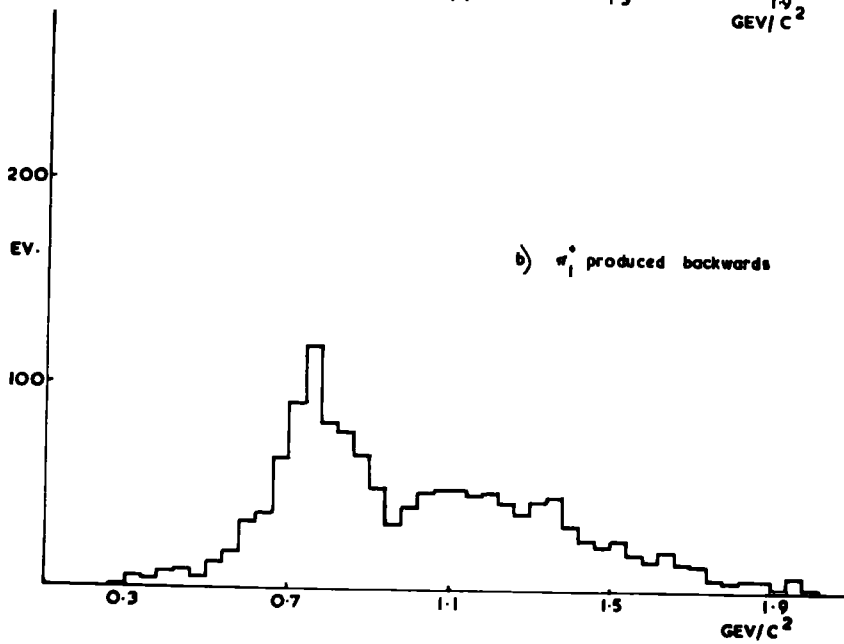
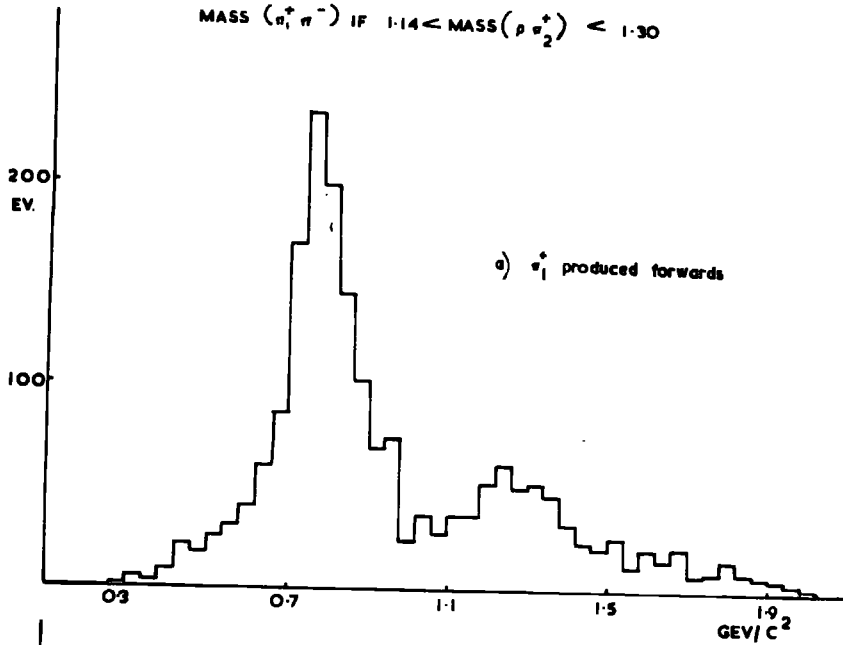
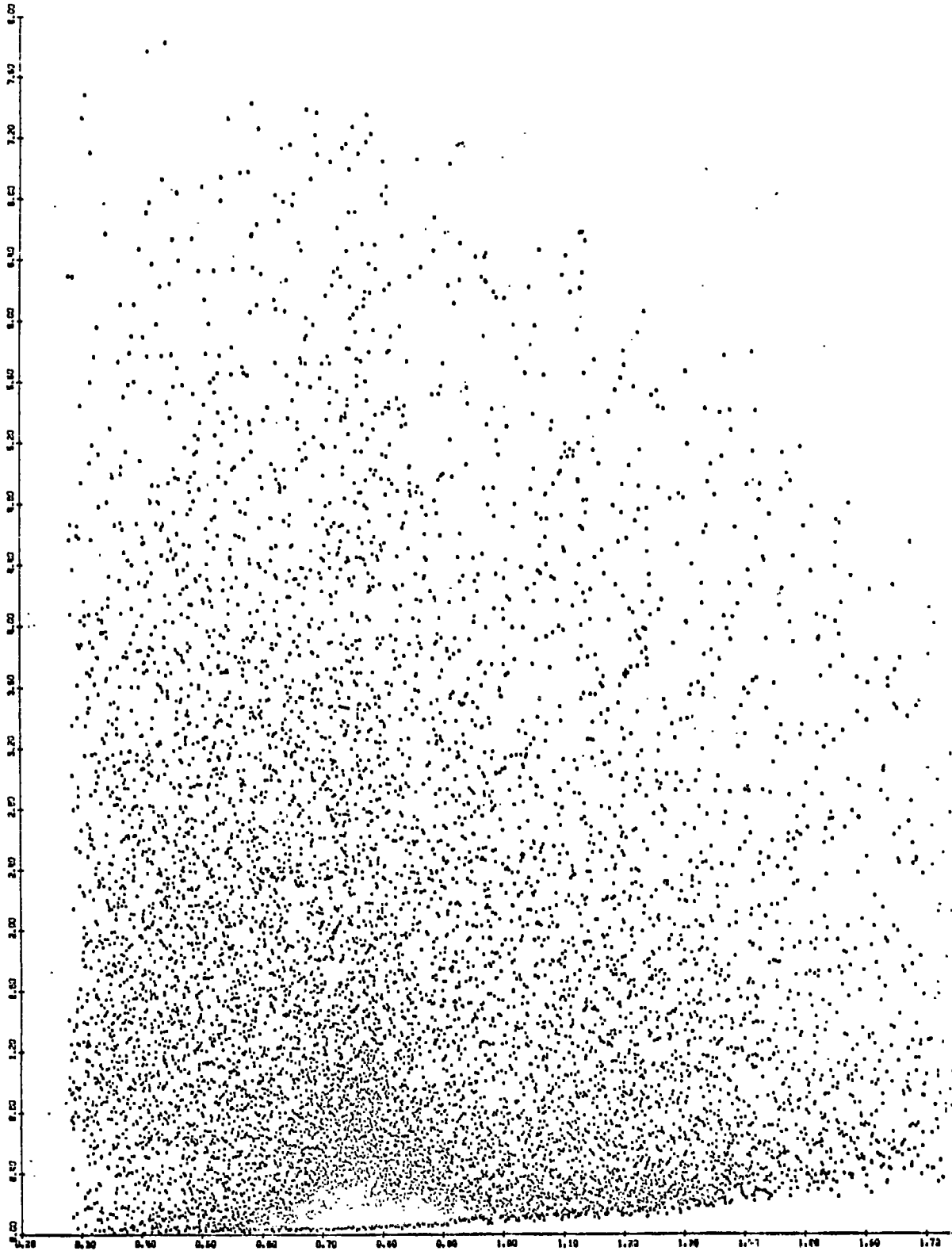


FIG. 25

$\Delta^2 (\pi^+ / \pi^+ \pi^-)$  VS. MASS ( $\pi^+ \pi^-$ )



events for which  $|t(p/p\pi^+)| < 0.3 \text{ GeV}^2$  (and taking both  $p\pi^+$  combinations if both satisfy this condition), the scatter plot of the effective mass of the  $p\pi^+$  combination against the effective mass of the associated  $\pi^+\pi^-$  system is shown in fig. 26. It can be seen that the  $N^*\rho^0$  and  $N^*\omega^0$  production processes are very much favoured by such a selection.

Fig. 27 shows the distribution of  $-t$  for the reaction of  $\pi^+p \rightarrow N^*\rho^0$  showing the sharp forward peak. For this, events have been selected in which a  $p\pi^+$  combination has an effective mass in the range 1.14 to 1.30  $\text{GeV}/c^2$  and the complementary  $\pi^+\pi^-$  combination has an effective mass in the range 0.66 to 0.86  $\text{GeV}/c^2$ . Writing  $d\sigma/dt \propto e^{at}$  for this range of  $t$  the value  $a = 11.6 \pm 0.6 \text{ GeV}^{-2}$  is obtained. At 8  $\text{GeV}/c(10)$ , it was found that  $a = 11.7 \pm 1.1 \text{ GeV}^{-2}$  for  $0.06 < -t < 0.4 \text{ GeV}^2$ . In table 12, the values of the slope for different, nearby regions of fig.19 are given for comparison. There appears to be quite strong peripheralism with the production of a single resonance, but not so much with the four-body production process.

Fig. 28 shows a part of the Chew-Low plot of the  $\pi^+\pi^-$  systems associated with a possible  $N^*$ . The region shown is that corresponding to high values of  $|t|$ , and the boundary of the physical region, as limited by kinematics, is shown. The presence of  $\rho^0$  production at

FIG. 26

MASS( $\pi^+\pi^-$ ) vs. MASS( $\rho\pi^+$ )  
 $\Delta^2(\rho/\rho\pi^+) < 0.3$

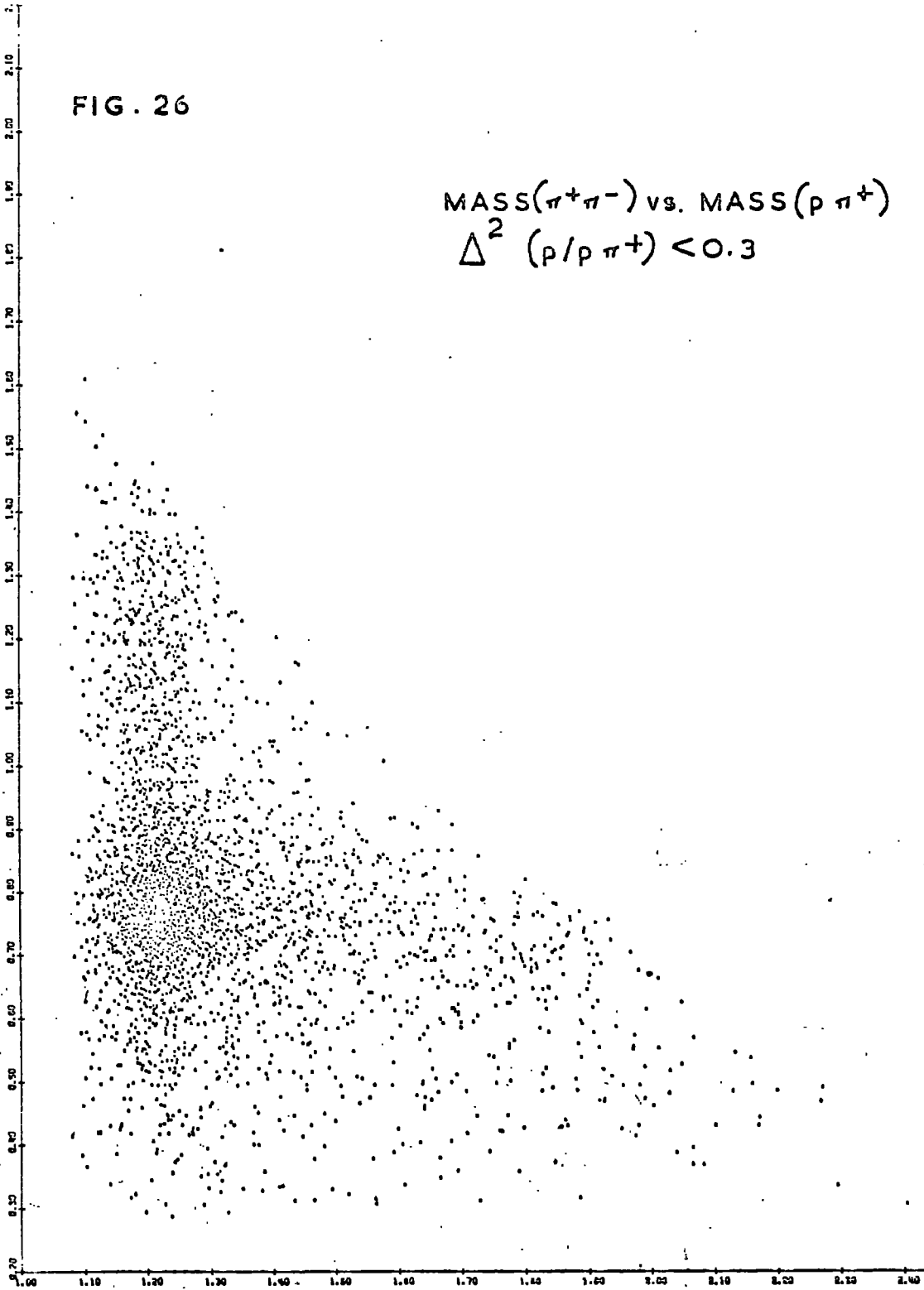
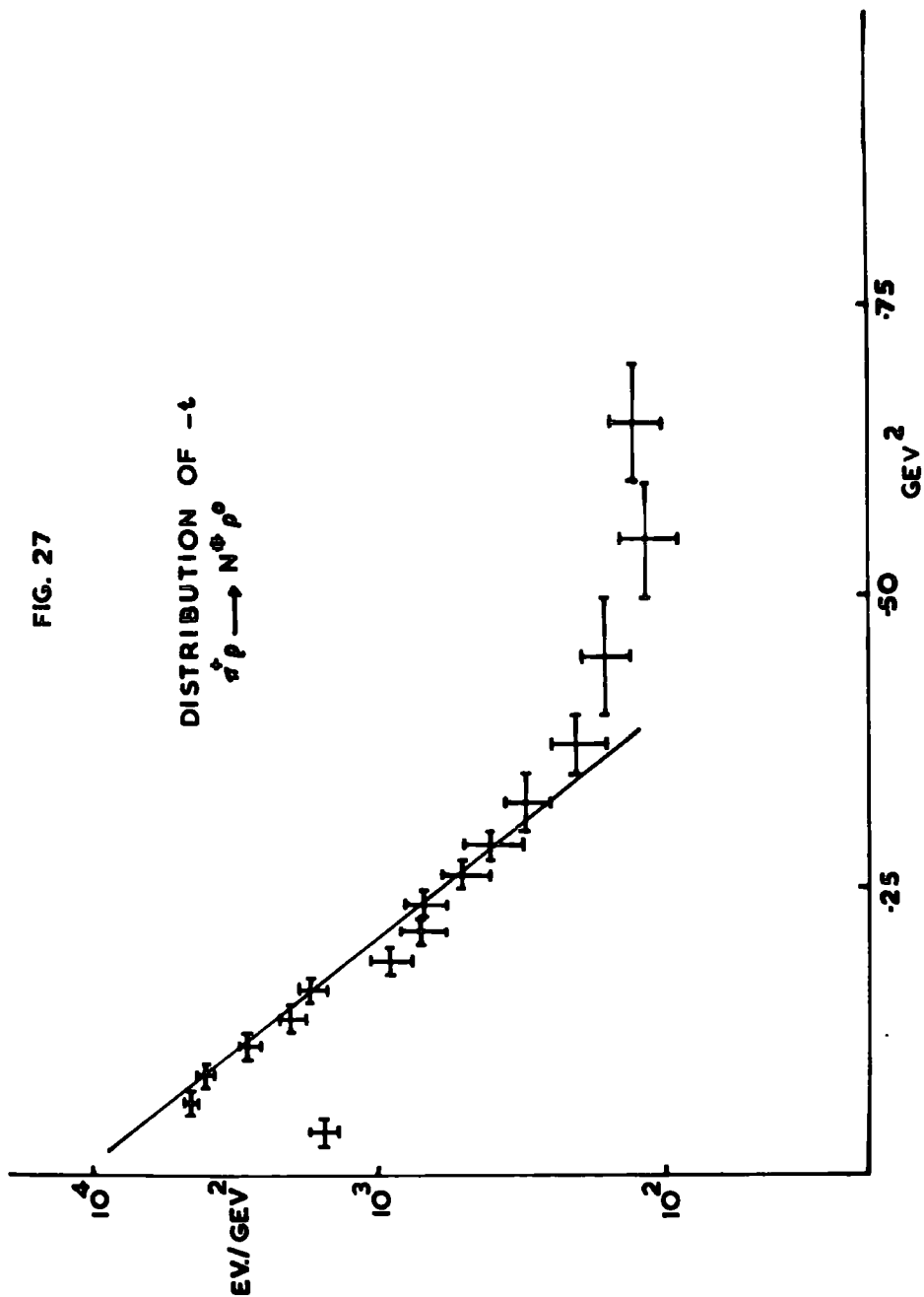
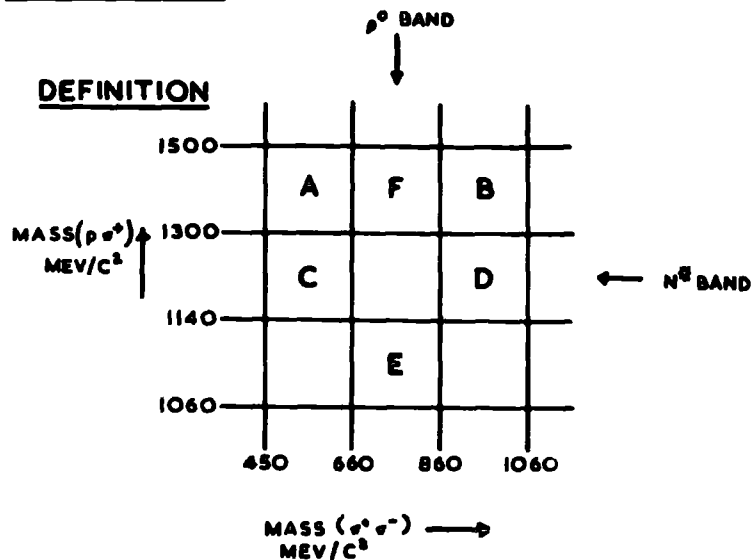


FIG. 27



**TABLE 12**

**$d\sigma/dt$  SLOPES FOR REGIONS ADJACENT TO  $N^{\oplus}\rho^{\ominus}$  REGION**



|  |   | RANGE OF<br>$-t$ (GEV <sup>2</sup> ) | SLOPE<br>(GEV <sup>-2</sup> ) |
|--|---|--------------------------------------|-------------------------------|
| $\sigma^+p \rightarrow p\sigma^+\sigma^+\sigma^-$  | A | 0.0 - 0.8                            | $4.6 \pm 0.5$                 |
|  | B | 0.1 - 0.8                            | $3.5 \pm 0.5$                 |
| $\sigma^+p \rightarrow N^{\oplus}\sigma^+\sigma^-$ | C | 0.0 - 0.6                            | $9.3 \pm 0.8$                 |
|  | D | 0.1 - 0.6                            | $7.6 \pm 0.6$                 |
| $\sigma^+p \rightarrow p\sigma^+\rho^{\ominus}$    | E | 0.0 - 0.6                            | $10.6 \pm 1.3$                |
|  | F | 0.1 - 0.6                            | $7.3 \pm 0.6$                 |
| $\sigma^+p \rightarrow N^{\oplus}\rho^{\ominus}$   |   | 0.05 - 0.35                          | $11.6 \pm 0.6$                |

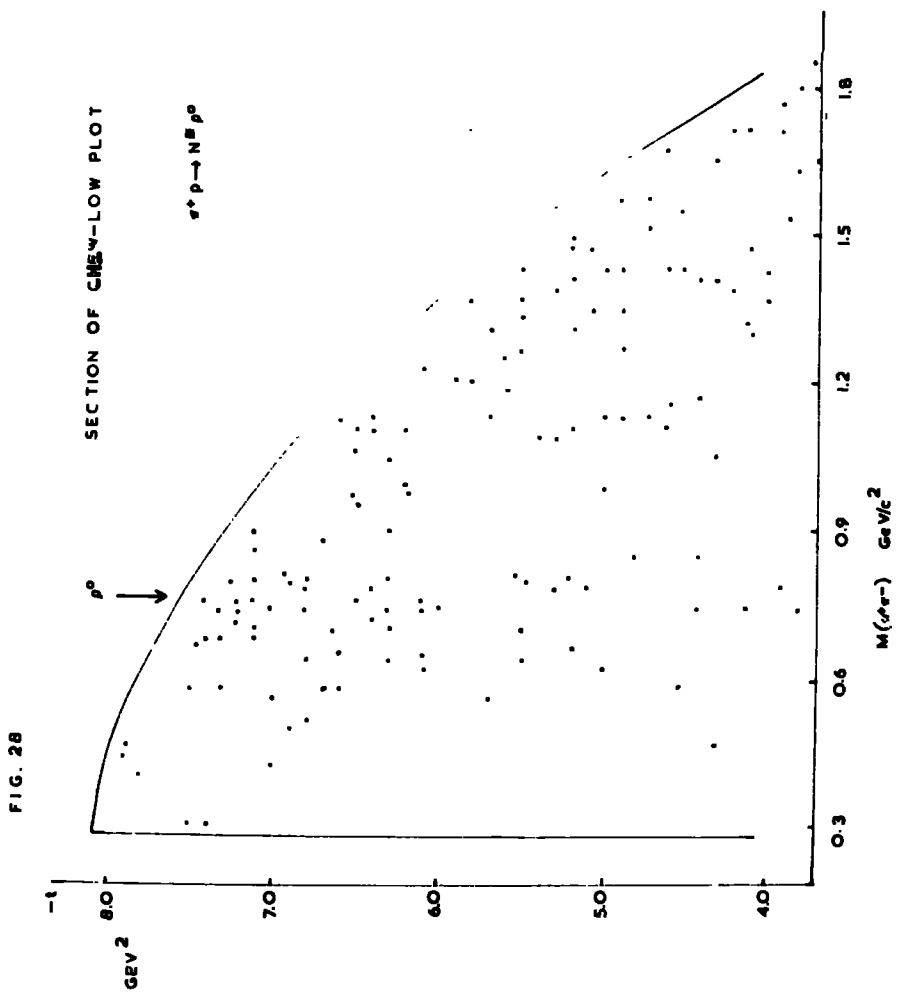


FIG. 28

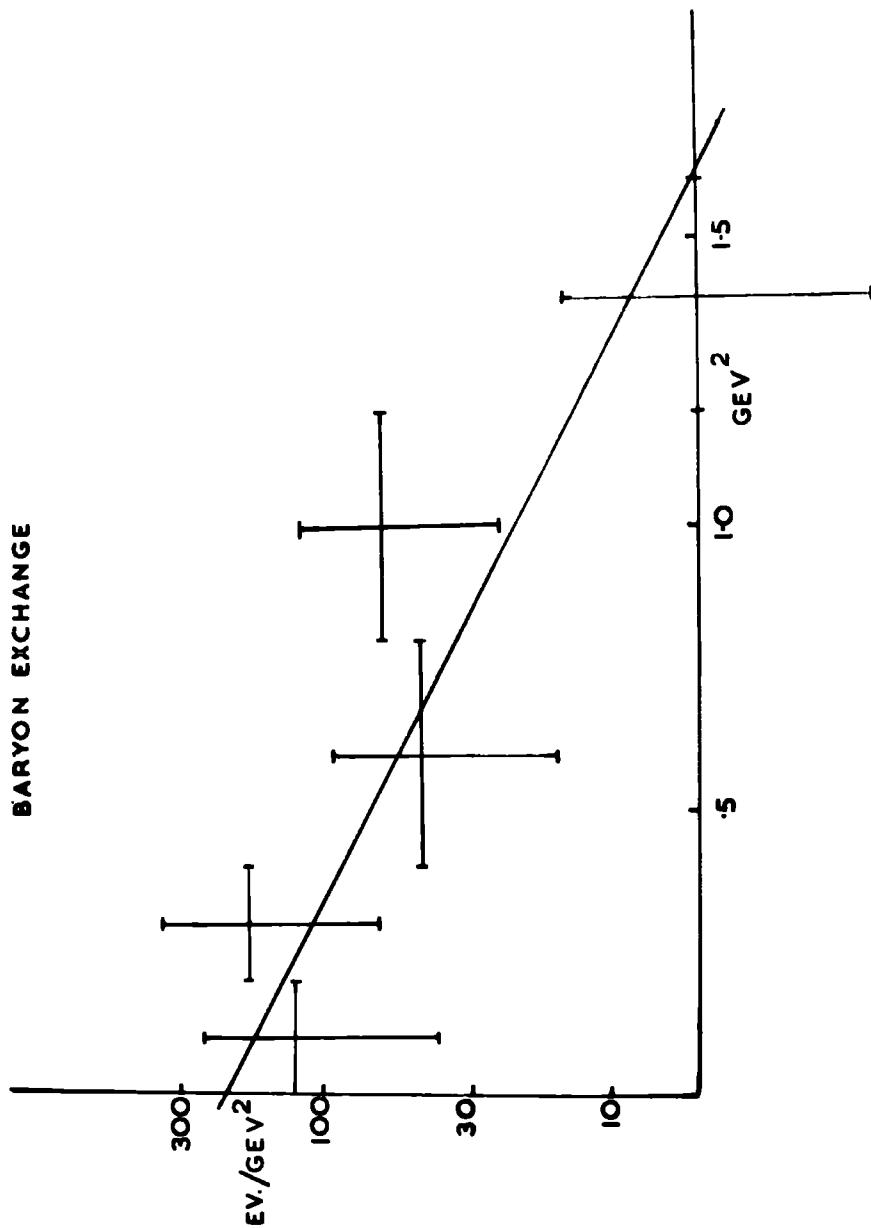
high values of  $|t|$  can be seen, consistent with the production of  $N^*\rho^0$  by a baryon exchange mechanism.

Estimating the background from nearby regions, the cross-section for the backward  $N^*\rho^0$  production is found to be  $7 \pm 3 \mu\text{b}$ . Taking the reaction as being due to baryon exchange,  $t$  is defined thus:-

$$t = \left[ q(N^*) - q(\pi^+) \right]^2 = \left[ q(\rho^0) - q(p) \right]^2$$

Using this definition of  $t$ , fig. 29 shows the distribution of  $-t$  for  $N^*\rho^0$  production, using the same intervals of mass as for the forward peak. The distribution is again plotted on a logarithmic scale. Writing  $d\sigma/dt \propto e^{at}$ ,  $a$  is found to be  $1.2 \pm 0.4 \text{ GeV}^{-2}$  for this reaction with  $|t| < 1.5 \text{ GeV}^2$ .

FIG. 29  
DISTRIBUTION OF  $-t, \pi^+ p \rightarrow N^+ \rho^0$  BY  
BARYON EXCHANGE



5.3.4 Decay angular distributions of  $N^*$  and  $\rho^0$

The  $N^*\rho^0$  reaction has been studied in terms of the Gottfried-Jackson analysis. The decay angles are defined as follows:-

$\theta_\rho$  is the angle between the directions of the incoming  $\pi^+$  and the outgoing  $\pi^+$  produced by the decay of the  $\rho^0$ .

$\phi_\rho$  is the angle between the production plane of the  $N^*$  and the plane defined by the incoming  $\pi^+$  and the  $\pi^+$  produced by the decay of the  $\rho^0$ .

Both of these angles are defined in the rest system of the  $\rho^0$ . The angles  $\theta_{N^*}$  and  $\phi_{N^*}$  are defined in a similar way for the decay of the  $N^*$  in the rest system of the  $N^*$ .

The distributions of the decay angles are given by (26):

$$W_\rho(\theta_\rho, \phi_\rho) = \frac{3}{4\pi} \left[ \rho_{11} \sin^2 \theta_\rho + \rho_{00} \cos^2 \theta_\rho - \rho_{1,-1} \sin^2 \theta_\rho \cos 2\phi_\rho - \sqrt{2} \operatorname{Re} \rho_{10} \sin 2\theta_\rho \cos \phi_\rho \right]$$

$$W_{N^*}(\theta_{N^*}, \phi_{N^*}) = \frac{3}{4\pi} \left[ \rho_{33} \sin^2 \theta_{N^*} + \rho_{11} \left( \frac{1}{3} + \cos^2 \theta_{N^*} \right) - \frac{2}{\sqrt{3}} \operatorname{Re} \rho_{3,-1} \sin^2 \theta_{N^*} \cos 2\phi_{N^*} - \frac{2}{\sqrt{3}} \operatorname{Re} \rho_{21} \sin 2\theta_{N^*} \cos \phi_{N^*} \right]$$

Where  $\rho_{mm'}$  are the spin-density matrix elements for spin components  $m, m'$  in the decay and the production of the resonance. ( $3/2, 1/2$  are abbreviated as 3, 1 in the expression for  $N^*$ .) The direction

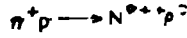
of measurement of  $m$  and  $m'$  is taken as the direction of the incoming  $\pi^+(p)$  in the rest system of the  $\rho^0(N^*)$ . On the basis of the one-pion exchange model without absorption, one would therefore expect  $m = m' = 0$ .

The density matrix elements have been calculated from the decay angular distributions for different intervals of  $t$  and are shown in fig. 30. The curves are the distributions calculated on the basis of the one-pion-exchange model with absorption at 4 GeV/c (27). There are some discrepancies in the  $\rho_{1,-1}$  and  $\rho_{33}$  elements. There is, however, the problem of selecting a pure sample of  $N^*\rho^0$  events, and there seems to be a significant amount of interference with S-wave background in the  $\rho^0$  selection, as can be seen from the unsymmetrical decay distribution ( $F-B/F+B = 0.35 \pm 0.03$  for  $\rho^0$  decays.). Bearing this problem in mind, the agreement with the absorption model calculation seems to be satisfactory.

In fig. 31 the distributions of  $\cos \theta_\rho$  and  $\cos \theta_{N^*}$  are shown for different intervals of the other, to look for correlations between the decays of  $\rho^0$  and  $N^*$ , which would not be expected if the production was by the exchange of a spinless particle

FIG 20

SPIN DENSITY MATRIX ELEMENTS



$N^*$

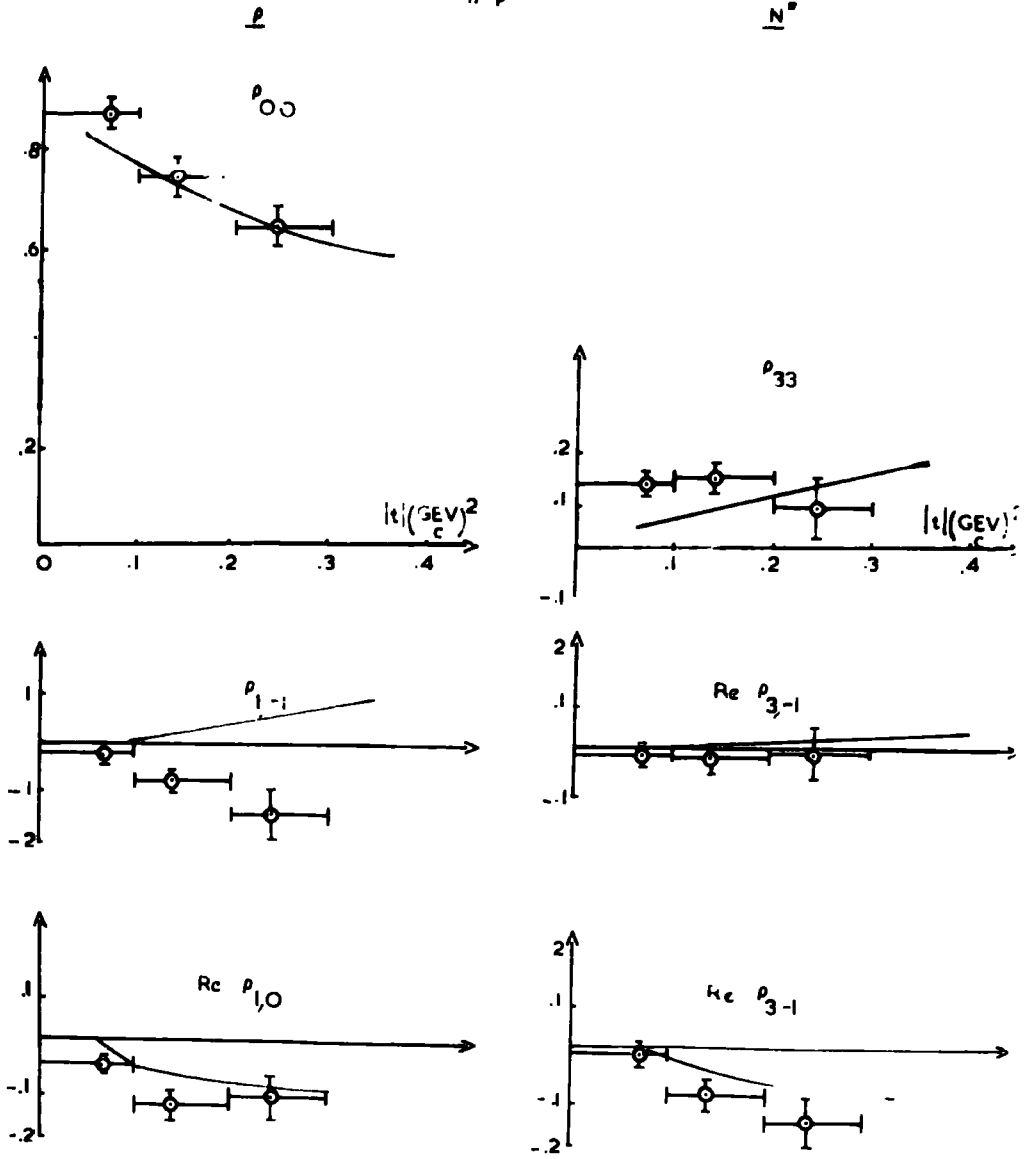
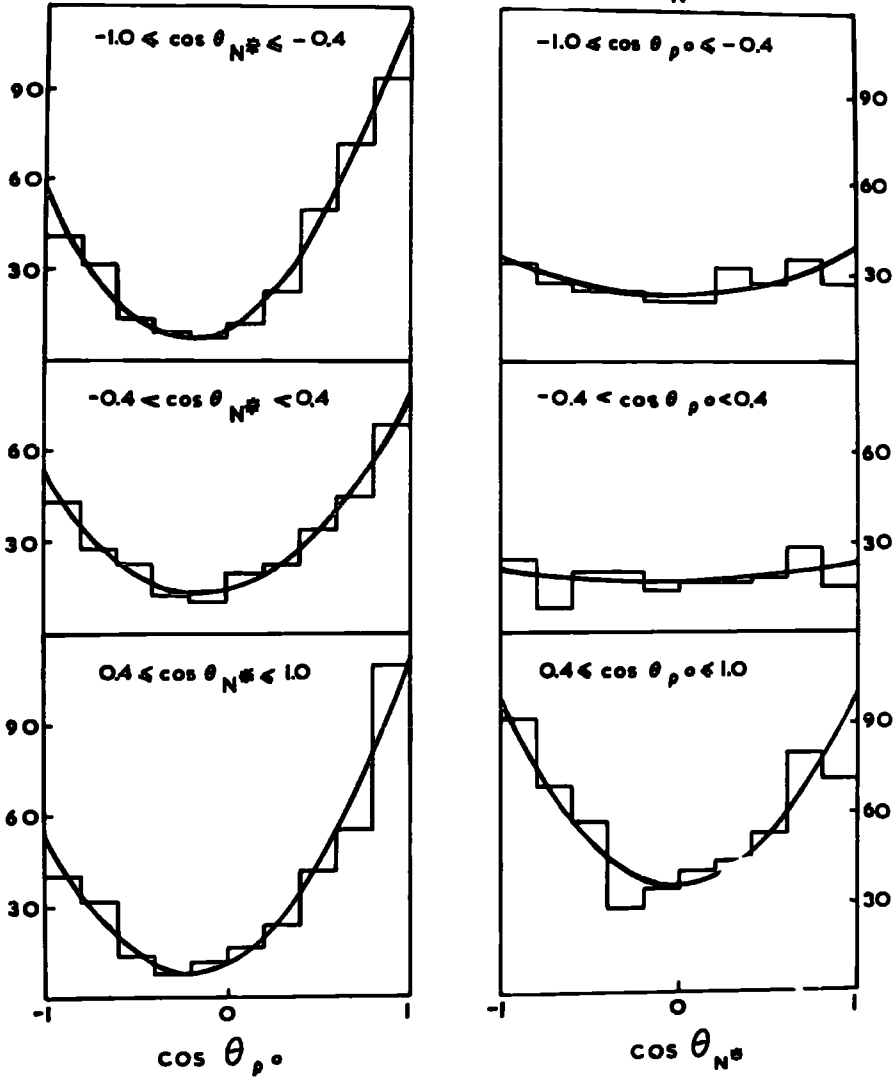


FIG.31

DECAY ANGULAR CORRELATIONS



such as a pion. Events with  $|t| < 0.3 \text{ GeV}^2$  were used for this. A correlation between the  $N^*$  and the  $\rho^0$  vertex can be observed, which is in disagreement with either a simple one-pion exchange model or a form-factor modification of it. The distributions have been fitted by a function proportional to  $(1 + B \cos\theta + C \cos^2\theta)$ . The coefficients B and C are presented in table 13. The fact that some correlation is observed indicates that there are some absorptive effects in the reaction.

Table 13

Coefficients of  $N^*$  and  $\rho^0$  decay distribution

a)  $N^*$  decay

| Range of $\cos \theta_\rho$ | B               | C               | Number of Events |
|-----------------------------|-----------------|-----------------|------------------|
| -1.0 to -0.4                | $0.04 \pm 0.13$ | $0.55 \pm 0.26$ | 264              |
| -0.4 to +0.4                | $0.06 \pm 0.15$ | $0.35 \pm 0.30$ | 180              |
| +0.4 to +1.0                | $0.01 \pm 0.13$ | $1.79 \pm 0.30$ | 573              |

b)  $\rho^0$  decay

| Range of $\cos \theta_{N^*}$ | B               | C               | Number of Events |
|------------------------------|-----------------|-----------------|------------------|
| -1.0 to -0.4                 | $3.03 \pm 0.63$ | $7.82 \pm 1.50$ | 356              |
| -0.4 to +0.4                 | $1.02 \pm 0.29$ | $3.71 \pm 0.70$ | 309              |
| +0.4 to +1.0                 | $2.51 \pm 0.50$ | $6.38 \pm 1.12$ | 352              |

### 5.3.5 The $A_2^+$ meson

Fig. 32 shows the effective mass distribution for the  $\pi^+\pi^+\pi^-$  combination. The enhancement due to the production of the  $A_2$  meson can be seen. The number of events above the background is estimated to be  $93 \pm 25$ , and the cross-section for the production of  $A_2^+$  decaying to  $\pi^+\pi^+\pi^-$  to be  $42 \pm 12 \mu\text{b}$ .

The  $A_2^+$  signal is improved by examining only the events which satisfy the following two conditions:

- 1) The effective mass of either of the two possible combinations is compatible with  $\rho^0$  i.e. in the range 0.66 to 0.88  $\text{GeV}/c^2$ .
- 2) The event is not compatible with  $N^*\rho^0$  production, the mass range of the  $N^*$  being defined to be 1.14 to 1.30  $\text{GeV}/c^2$ . It can be seen in fig. 19., that the effective mass of  $p\pi^+$  in the  $\rho$  band is roughly uniform apart from the  $N^*$  production, so roughly 10% of  $\rho^0$  not produced with  $N^*$  will be excluded by this condition, and the cross-section for  $A_2^+$  production must be corrected accordingly.

Fig. 33. shows the distribution of the  $\pi^+\pi^+\pi^-$  effective mass for events satisfying these conditions. The peak corresponding to the production of  $A_2^+$  contains  $116 \pm 21$  events above the estimated background. The cross-section for the production of  $A_2^+$  and its subsequent decay to  $\pi^+\rho^0$  is therefore estimated to be  $58 \pm 10 \mu\text{b}$ .

FIG. 32

REACTION A

MASS ( $\sigma^+ \sigma^+ \sigma^-$ )

$A_2^+$

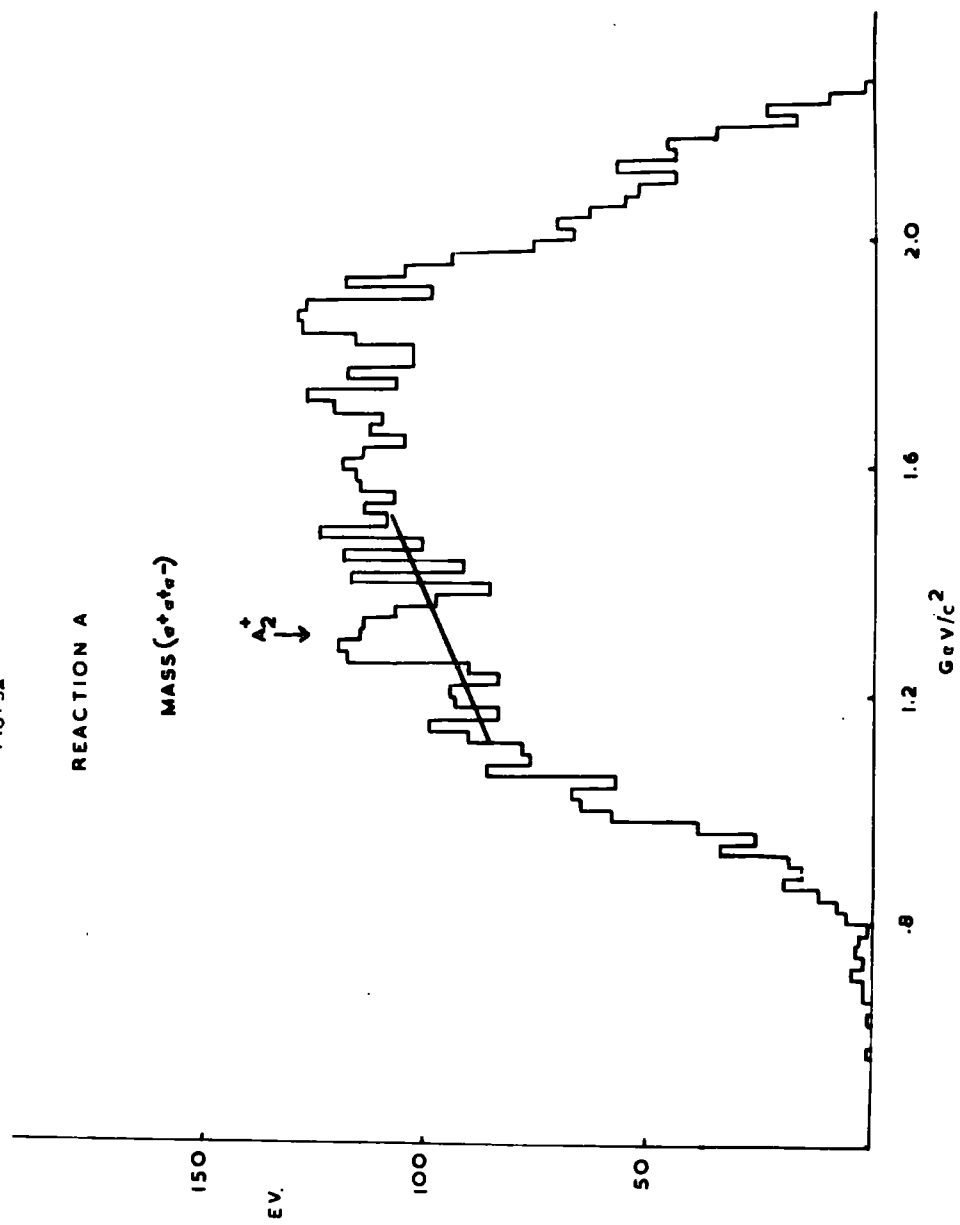
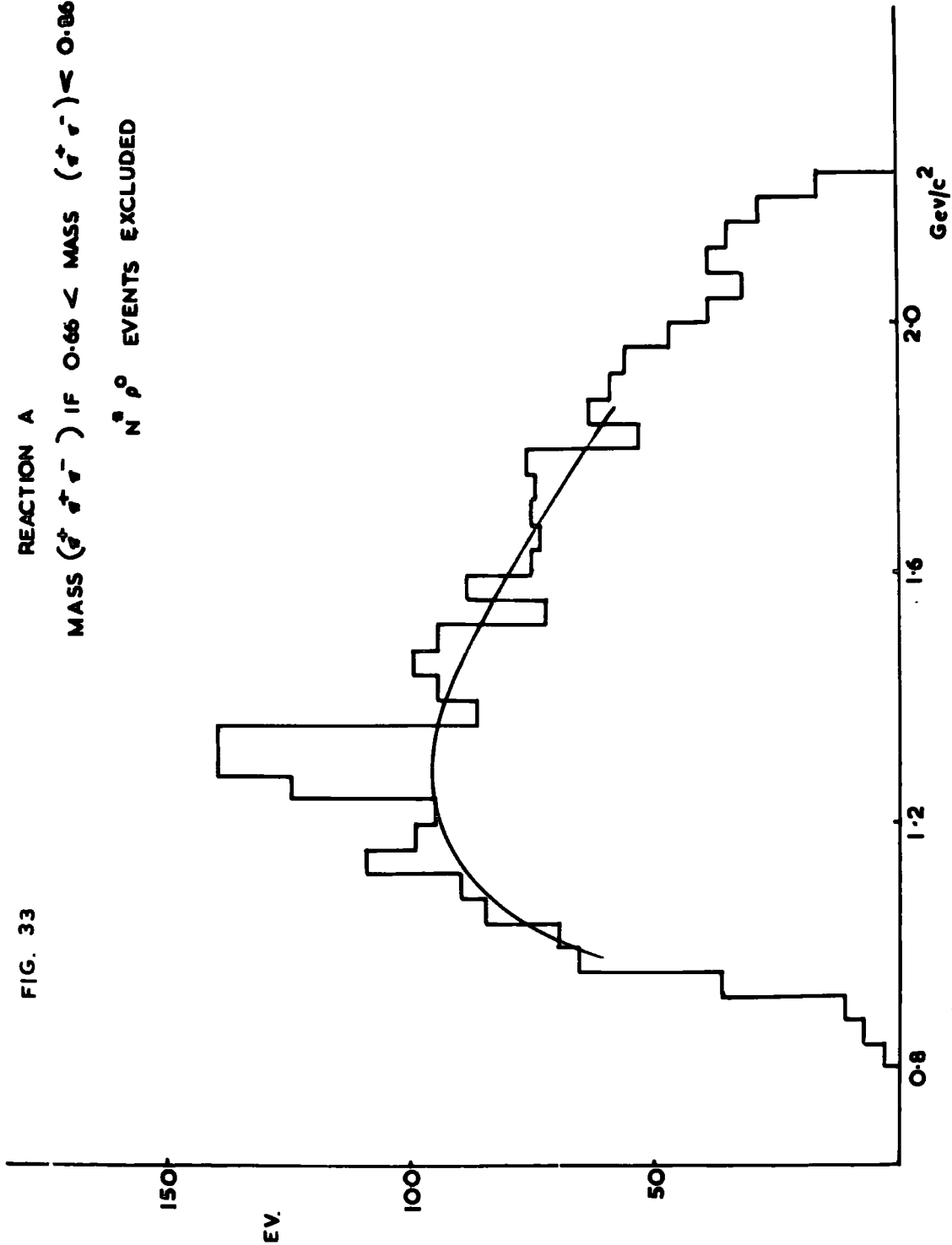


FIG. 33

REACTION A

MASS ( $e^+ e^-$ ) IF  $0.66 < \text{MASS} (e^+ e^-) < 0.86$

$N^0 \rho^0$  EVENTS EXCLUDED



#### 5.4. Reaction B

In this section the reaction B ( $\pi^+p \rightarrow p\pi^+\pi^+\pi^-\pi^0$ ) is studied. After restricting the sample on the basis of the square of the missing mass, 6453 events remain. The main features of this reaction are the production of  $N^*$  and  $\omega^0$ . In addition there is evidence for the production of  $\eta^0$ ,  $A_2$  and  $B^+$ .

##### 5.4.1 $N^*$ , $\omega^0$ and $\eta^0$ production

Fig. 34 shows a scatter plot of the effective mass of  $p\pi^+$  versus the effective mass of the remaining  $\pi^+\pi^-\pi^0$ . Each event is represented twice on the diagram, corresponding to the two possible combinations of . The bands due to the formation of  $N^*$  and  $\omega^0$  can be seen, as well as the concentration of points in the overlap region due to the combined production of  $N^*$  and  $\omega^0$ . The band due to the production of  $\eta^0$ , particularly in association with  $N^*$ , can also be seen.

In fig. 35 is shown the projection of the scatter diagram to give the effective mass distribution for  $p\pi^+$ , in which the strong  $N^*$  peak can be seen. Estimating the number of entries above the smooth background, one estimates that  $2420 \pm 150$  events in the sample proceed via the production of  $N^*$ . The cross-section for  $N^*$  production in this reaction is therefore  $1.08 \pm 0.06$  mb, or  $37 \pm 2\%$  of reaction B.

FIG. 34

MASS( $\pi^+\pi^-\pi^0$ ) vs. MASS( $p\pi^+$ )

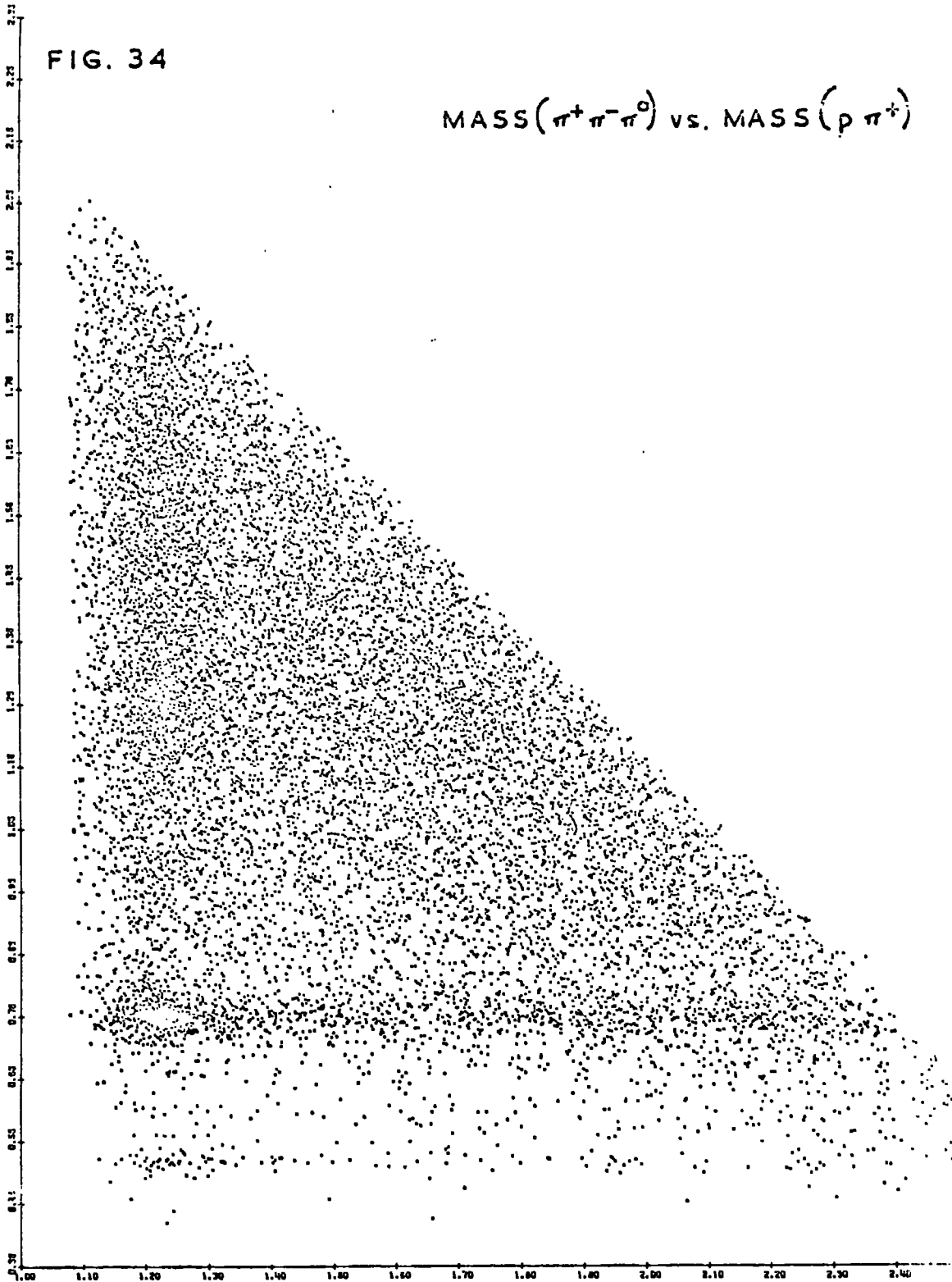


FIG. 35  
REACTION B  
MASS (  $p \pi^+$  )

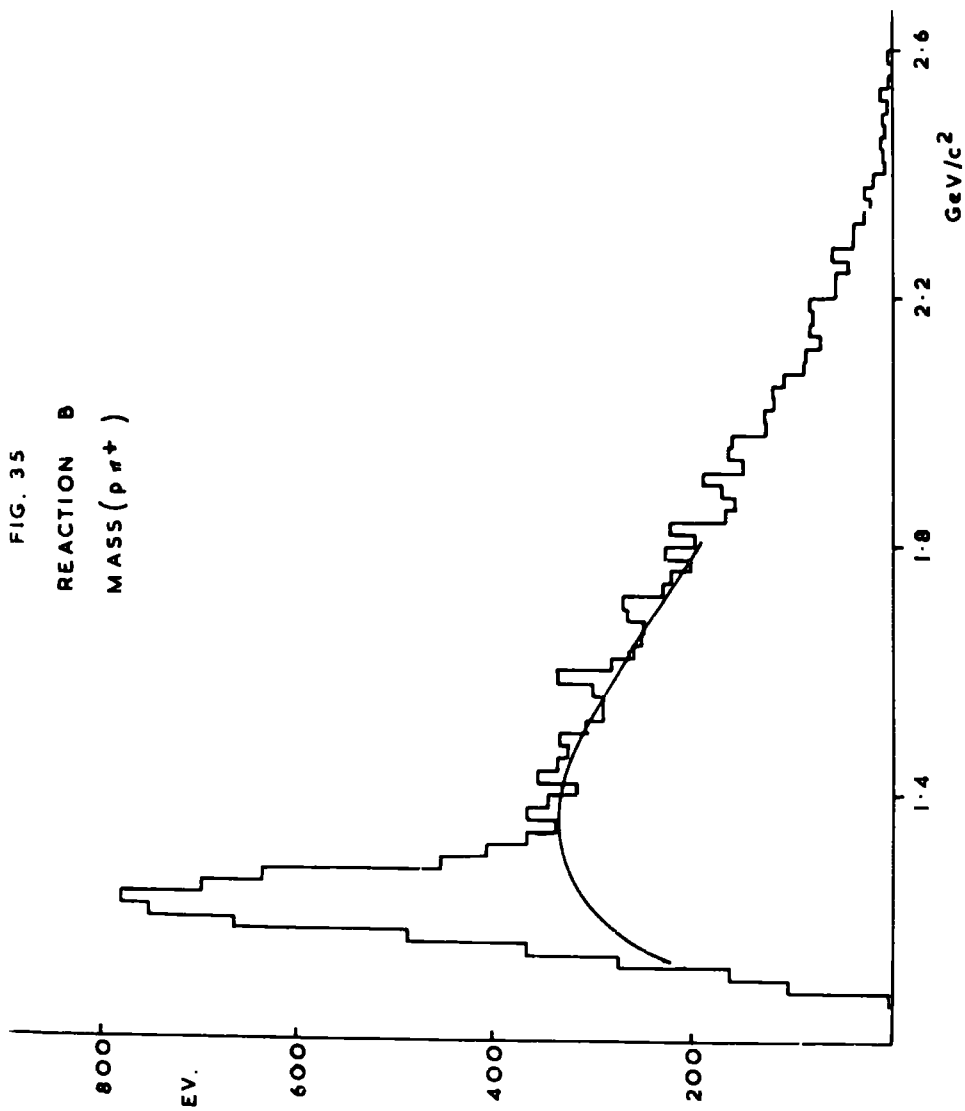


Fig. 36 is the projection of the scatter diagram to give the distribution of the effective mass of  $\pi^+\pi^-\pi^0$ . The strong production of the  $\omega^0$  can be seen.  $1150 \pm 70$  events are estimated to proceed via the production of an  $\omega^0$  decaying to  $\pi^+\pi^-\pi^0$ , and the cross-section for such a process is estimated to be  $0.51 \pm 0.045$  mb or  $18 \pm 1\%$  of reaction B. There is a small peak due to the production of  $\gamma^0$ , but a very significant one because of the small background. The number of entries above the estimated background is  $97 \pm 16$ . The cross-section for the production of  $\gamma^0$  decaying to  $\pi^+\pi^-\pi^0$  is therefore estimated to be  $43 \pm 8 \mu\text{b}$ .

Fig. 37 shows the effective mass distribution for  $\pi^+\pi^-\pi^0$  when the effective mass of the associated  $p\pi^+$  is in the range 1.14 to 1.30  $\text{GeV}/c^2$ . The peaks corresponding to  $\omega^0$  and to  $\gamma^0$  can be seen to be enhanced by this selection. However, the use of this histogram to estimate the amount of double resonance production is not as reliable as for reaction A, as in only  $60\%$ <sup>of</sup> this sample does the  $p\pi^+$  combination correspond to an  $N^*$ . The effective mass distribution of  $\pi^+\pi^-\pi^0$  was examined for different intervals of the effective mass of the remaining  $p\pi^+$ . Fig. 38 shows the number of  $\omega^0$ 's found in each sample as

FIG. 36  
REACTION B  
MASS (  $\pi^+\pi^-\pi^0$  )

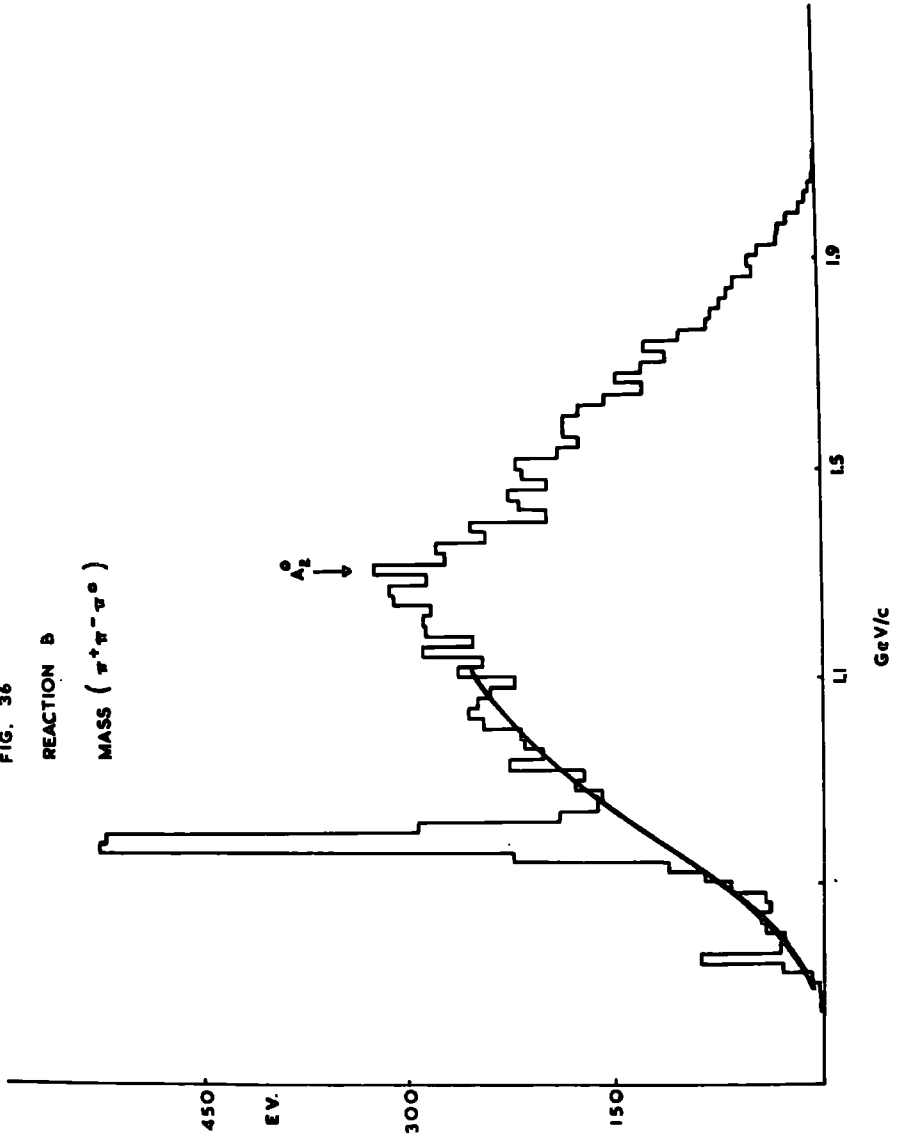


FIG. 37  
REACTION B  
MASS ( $\pi^+ \pi^- \pi^0$ ) WITH  $N^*$

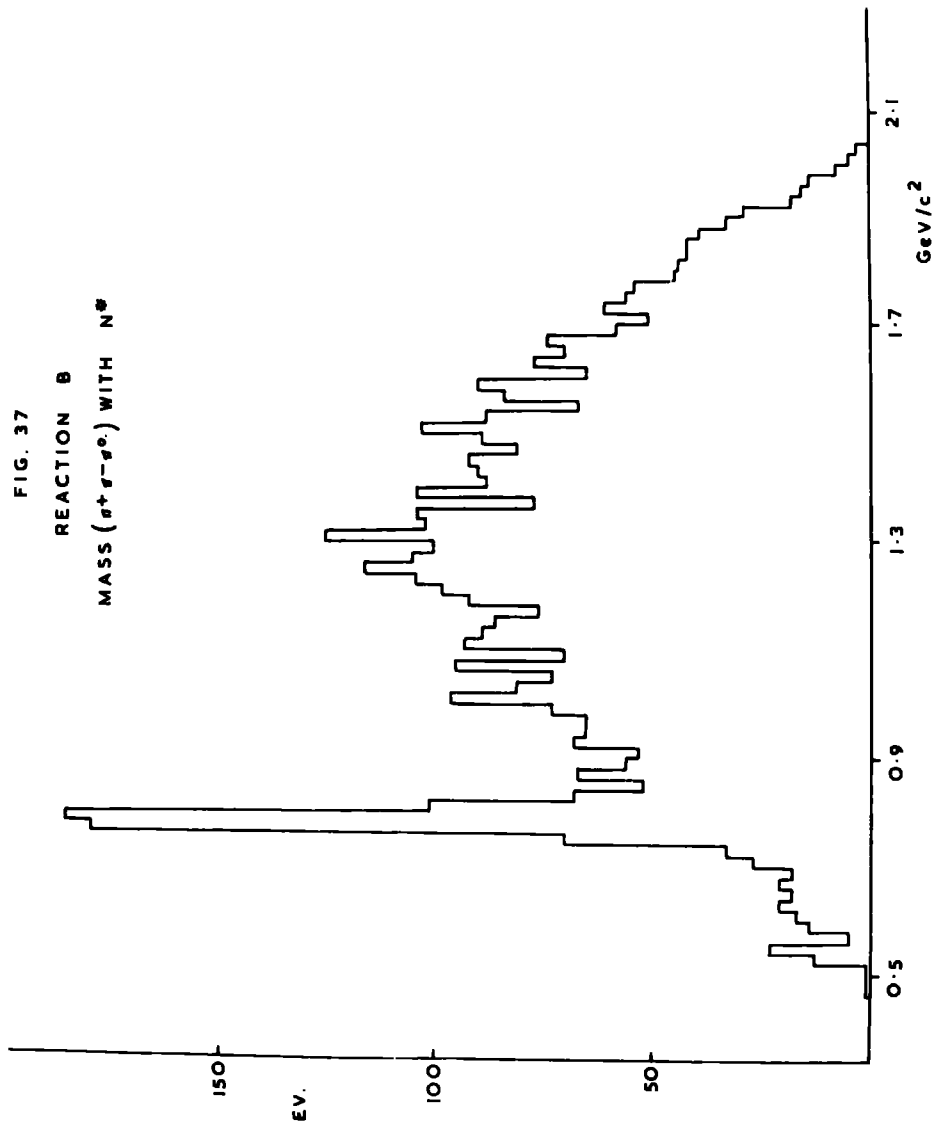
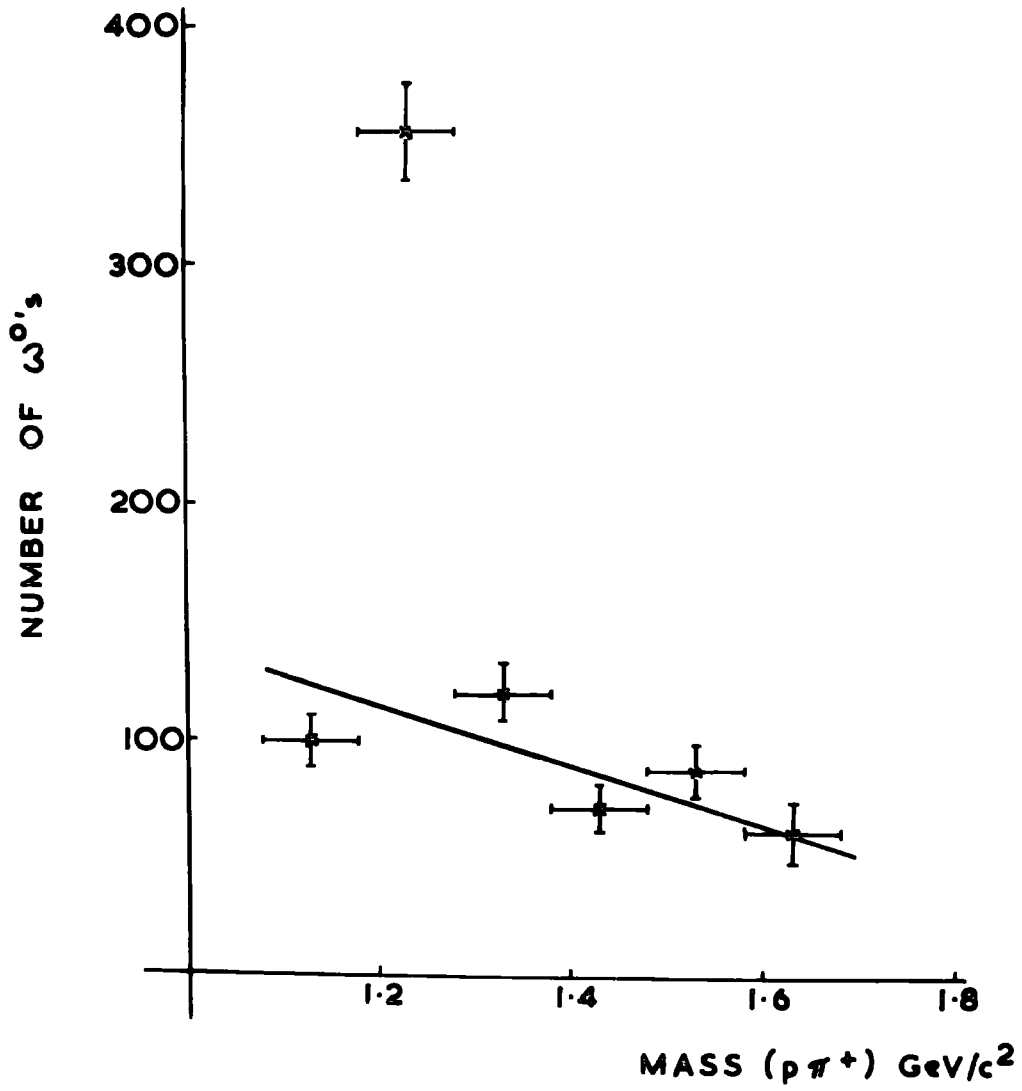


FIG.38

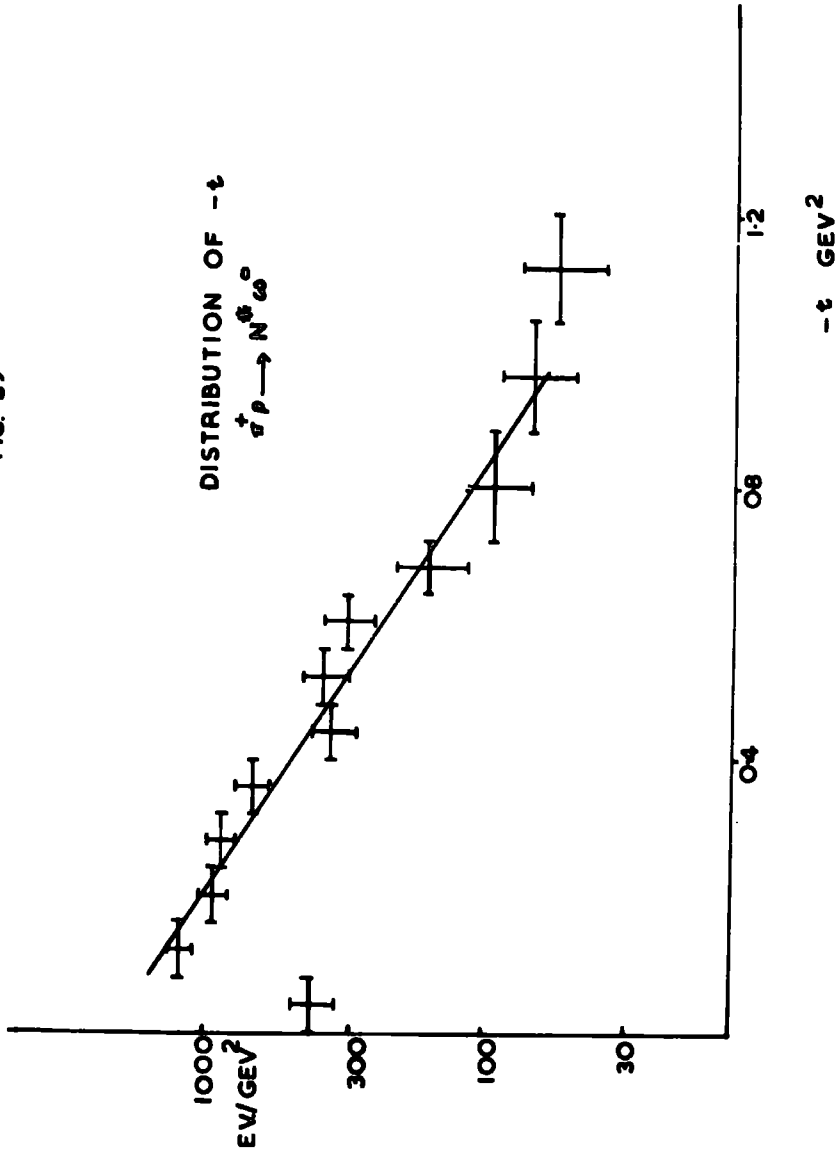


a function of the mass of the  $\rho\pi^+$  system. The line drawn on the figure is the background estimated from the three points above  $1.38 \text{ GeV}/c^2$ . The figure is essentially the distribution of the effective mass of  $\rho\pi^+$  when the products of the interaction are  $\rho\pi^+\omega^0$ , so the excess above the background corresponds to events in which  $N^*\omega^0$  is produced. This excess is estimated to be  $310 \pm 40$  events. The cross-section for the production of  $N^*\omega^0$  ( $\omega^0$  decaying to  $\pi^+\pi^-\pi^0$ ) is then  $0.14 \pm 0.02 \text{ mb.}$ , which is  $4.8 \pm 0.6\%$  of reaction B. Correcting for unseen decay modes, the cross-section for the production of  $N^*\omega^0$  is  $0.155 \pm 0.02 \text{ mb.}$  This value is compared with those from other experiments in fig. 23. To estimate the amount of  $N^*\gamma^0$  production, the scatter plot of fig. 34 was examined in the  $\gamma^0$  band, defined as  $0.52$  to  $0.58 \text{ GeV}/c^2$ . In the three regions of this band  $1.12$  to  $1.36$ ,  $1.36$  to  $1.60$ , and  $1.60$  to  $1.84 \text{ GeV}/c^2$ , one observes respectively 50, 17, and 16 points. The number of events which proceed via the production of  $N^*\gamma^0$  is estimated to be  $33 \pm 7$ . The cross-section for  $N^*\gamma^0$  production ( $\gamma^0$  decaying to  $\pi^+\pi^-\pi^0$ ) is therefore estimated to be  $15 \pm 3 \mu\text{b.}$

#### 5.4.2 t dependance of $N^*$ and $\omega^0$ production

Fig. 39 shows the distribution of  $t$  for events consistent with the production of  $N^*\omega^0$ . For this the

FIG. 39



$N^*$  was taken in the effective mass range 1.14 to 1.30  $\text{GeV}/c^2$  and the  $\omega^0$  in the range 743 to 823  $\text{MeV}/c^2$ . A forward peak for this process is observed, and an exponential representation of the form  $e^{at}$  has the slope  $a = 3.7 \pm 0.3 \text{ GeV}^{-2}$  over the range of  $|t|$ , 0.1 to 0.9  $\text{GeV}^2$ . This peak is considerably broader than that for  $N^*$  production. For comparison, the slopes for nearby regions of fig. 34 are given in table 14.

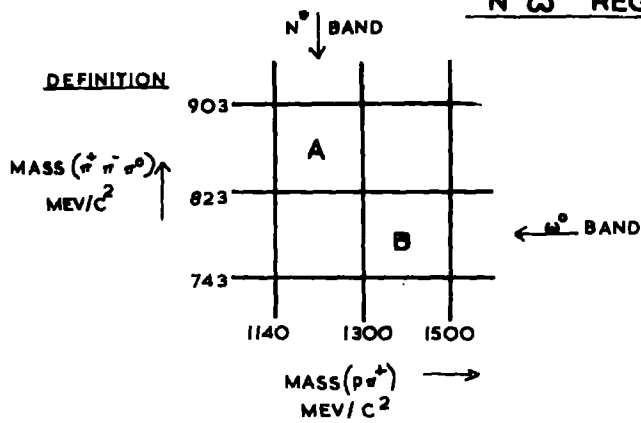
#### 5.4.3 Decay angular distributions of $N^*$ and $\omega^0$

The decay angular distributions have been studied by the Gottfried-Jackson analysis as for the  $N^* \rho^0$  production. In this case the normal to the decay plane (the direction  $\vec{p}_{\pi^+} \wedge \vec{p}_{\pi^0}$ ) was used to define the decay direction of the  $\omega^0$ , instead of the  $\pi^+$  direction as in the  $\rho^0$  decay.

Fig. 40 shows the spin density matrix elements obtained for four different intervals of  $t$ . The curves shown are the predictions of the absorption model assuming  $\rho$ -meson exchange with an electromagnetic coupling at the baryon vertex, calculated for 4  $\text{GeV}/c$  incident pion momentum. The distributions obtained do not agree with the predictions of the absorption model, although the results are much the same as those obtained by ABBBHLN collaboration (28) and by the ABC collaboration (10).

TABLE 14

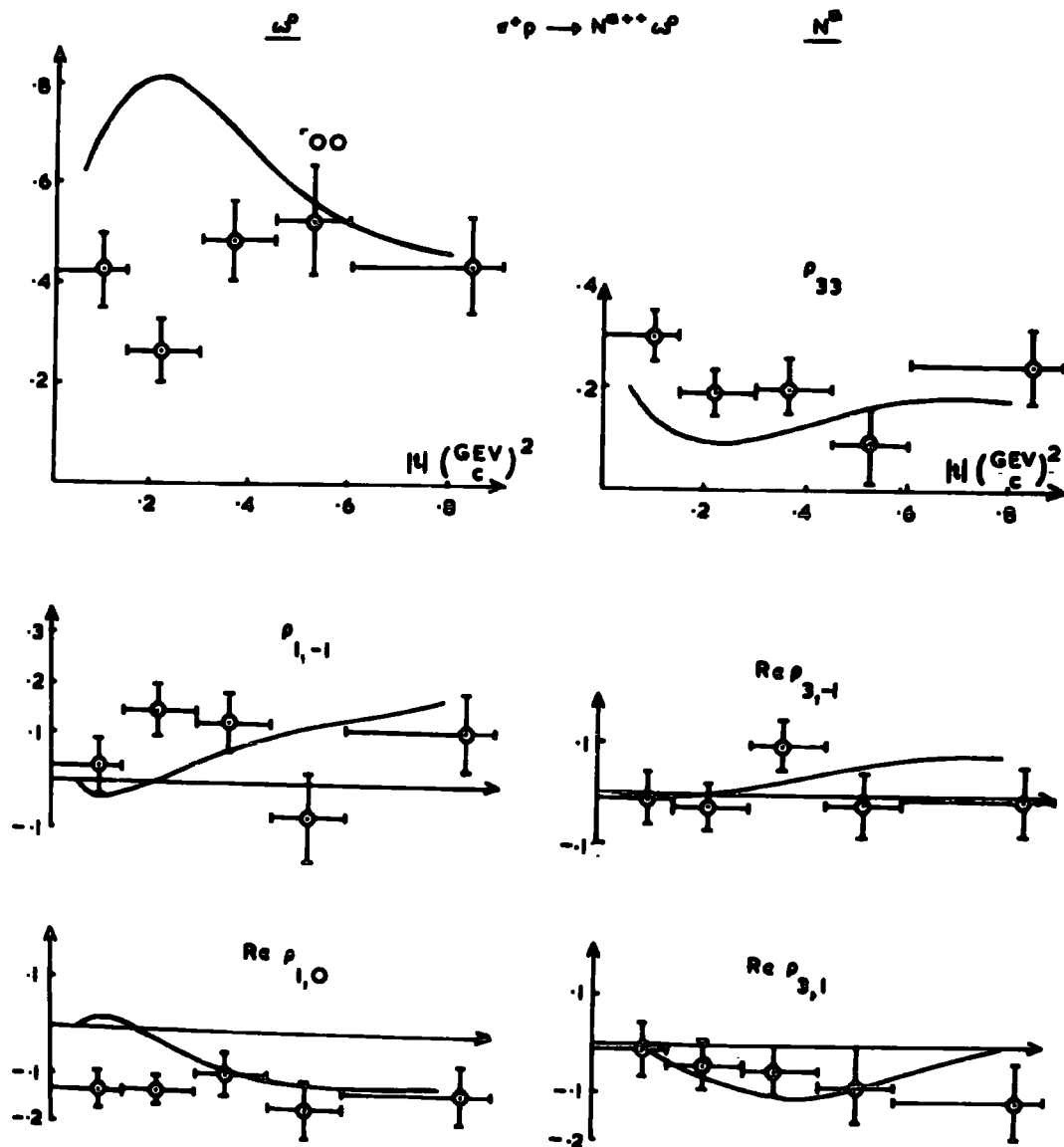
$d\sigma/dt$  SLOPES FOR REGIONS ADJACENT TO  
 $N^0\omega^0$  REGION



|   |   | RANGE OF<br>$-t$ (GEV <sup>2</sup> ) | SLOPE<br>GEV <sup>-2</sup> |
|---|---|--------------------------------------|----------------------------|
| $\pi^+ p \rightarrow N^0 \pi^+ \pi^- \pi^0$ | A | 0.1 — 0.6                            | $4.2 \pm 0.8$              |
| $\pi^+ p \rightarrow p \pi^+ \omega^0$      | B | 0.1 — 0.6                            | $3.1 \pm 0.7$              |
| $\pi^+ p \rightarrow N^0 \omega^0$          |   | 0.1 — 0.9                            | $3.7 \pm 0.3$              |

# SPIN DENSITY MATRIX ELEMENTS

FIG. 40



In fig. 41, the distributions of  $\cos \theta_{N^*}$  and  $\cos \theta_{\omega}$  are given for different intervals of the other. In this case, no significant correlation between the decays is observed. Table 15 gives the coefficients obtained by fitting each distribution with a function proportional to  $1+B \cos \theta + C \cos^2 \theta$ .

FIG. 41 DECAY ANGULAR CORRELATIONS

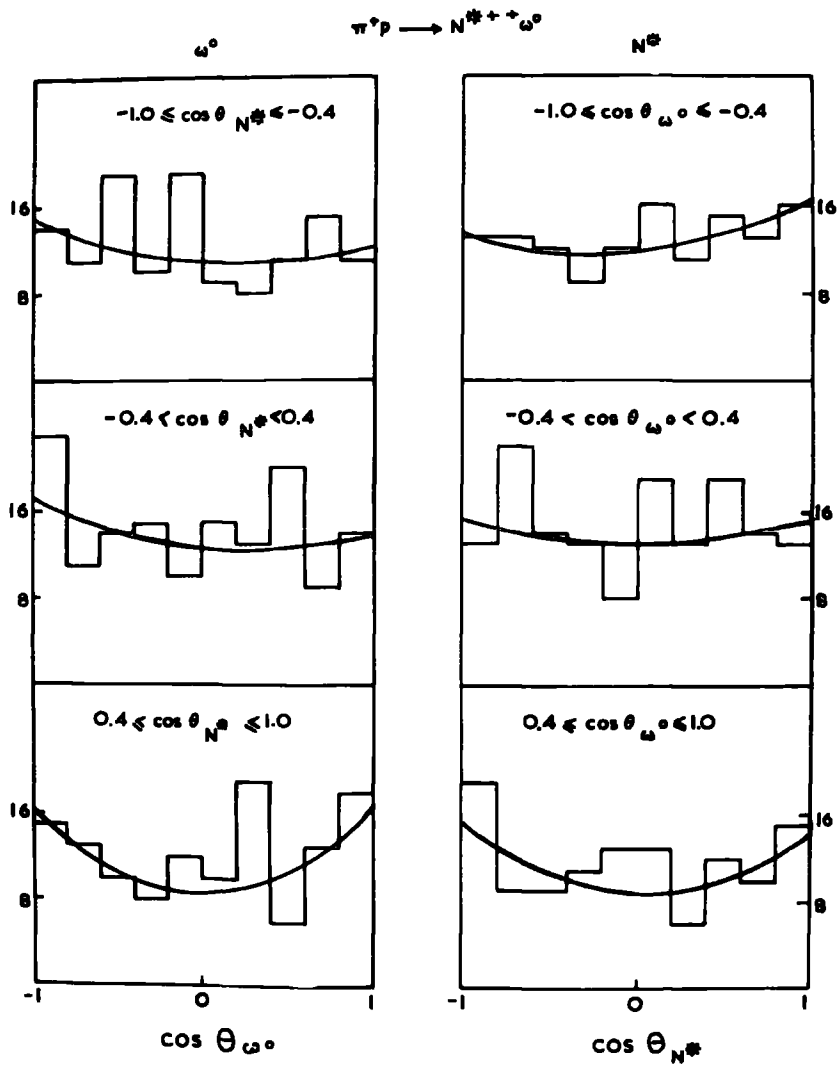


Table 15

Coefficients of  $N^*$  and  $\omega^0$  decay distributions

a)  $N^*$  decay

| Range of $\cos \theta_\omega$ | B                | C               | Number of Events |
|-------------------------------|------------------|-----------------|------------------|
| -1.0 to -0.4                  | $0.14 \pm 0.17$  | $0.28 \pm 0.34$ | 130              |
| -0.4 to +0.4                  | $-0.01 \pm 0.16$ | $0.18 \pm 0.30$ | 148              |
| +0.4 to +1.0                  | $-0.06 \pm 0.22$ | $0.67 \pm 0.45$ | 117              |

b)  $\omega^0$  decay

| Range of $\cos \theta_{N^*}$ | B                | C               | Number of Events |
|------------------------------|------------------|-----------------|------------------|
| -1.0 to -0.4                 | $-0.14 \pm 0.17$ | $0.22 \pm 0.34$ | 127              |
| -0.4 to +0.4                 | $-0.14 \pm 0.17$ | $0.23 \pm 0.34$ | 144              |
| +0.4 to +1.0                 | $-0.01 \pm 0.22$ | $0.79 \pm 0.67$ | 124              |

#### 5.4.4. $\rho$ production

Fig. 42 shows the effective mass distributions of  $\pi^+\pi^-$ , of  $\pi^+\pi^0$  and of  $\pi^-\pi^0$ . The dashed histogram in each case is the corresponding distribution excluding  $\omega^0$  events i.e. those in which a  $\pi^+\pi^-\pi^0$  combination has an effective mass in the range 743 to 823 MeV/c<sup>2</sup>. A peak in the region of the  $\rho$  meson can be seen on each distribution, and in each case, the signal is improved by the exclusion of  $\omega^0$  events. Some at least of the peak in the  $\pi^+\pi^-$  spectrum could be due to a reflection from the  $A_2^0$ .

#### 5.4.5. $A_2$ production

On fig. 36, the effective mass distribution for  $\pi^+\pi^-\pi^0$ , some enhancement in the region of the  $A_2$  meson can be seen. The signal is improved by imposing the following conditions:

- 1) The complementary  $\rho\pi^+$  combination has an effective mass in the range 1.14 to 1.30 GeV/c<sup>2</sup>.
- 2) Either the  $\pi^+\pi^0$  or the  $\pi^-\pi^0$  combination has an effective mass in the range 0.66 to 0.86 GeV/c<sup>2</sup>.

The resultant effective mass distribution is shown in fig. 43. The number of events above the background in the region of the  $A_2$  mass is estimated to be  $200 \pm 30$ . No evidence

FIG. 42

REACTION B

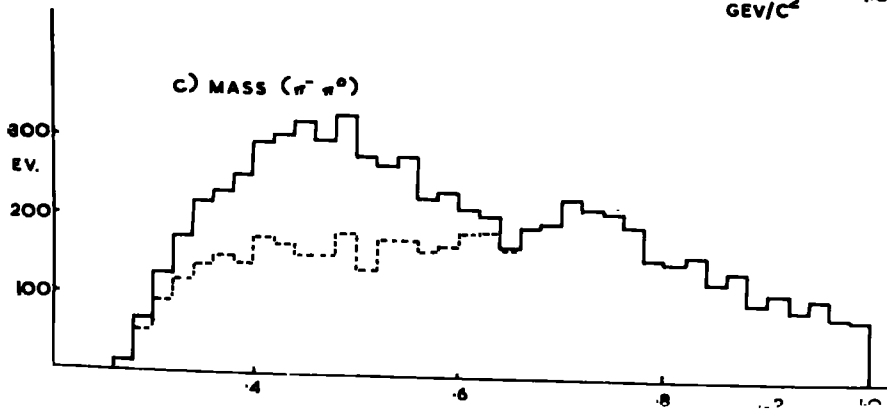
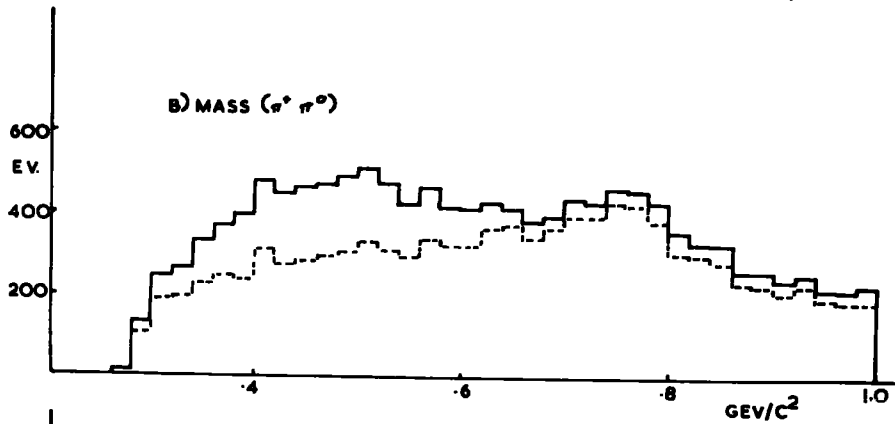
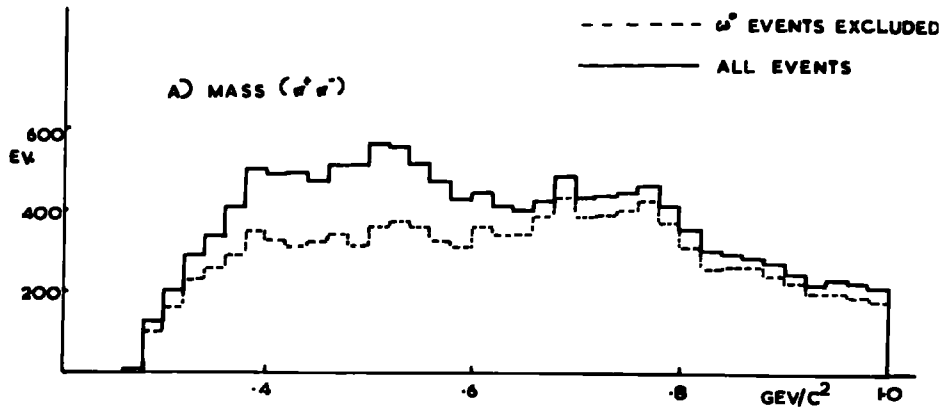
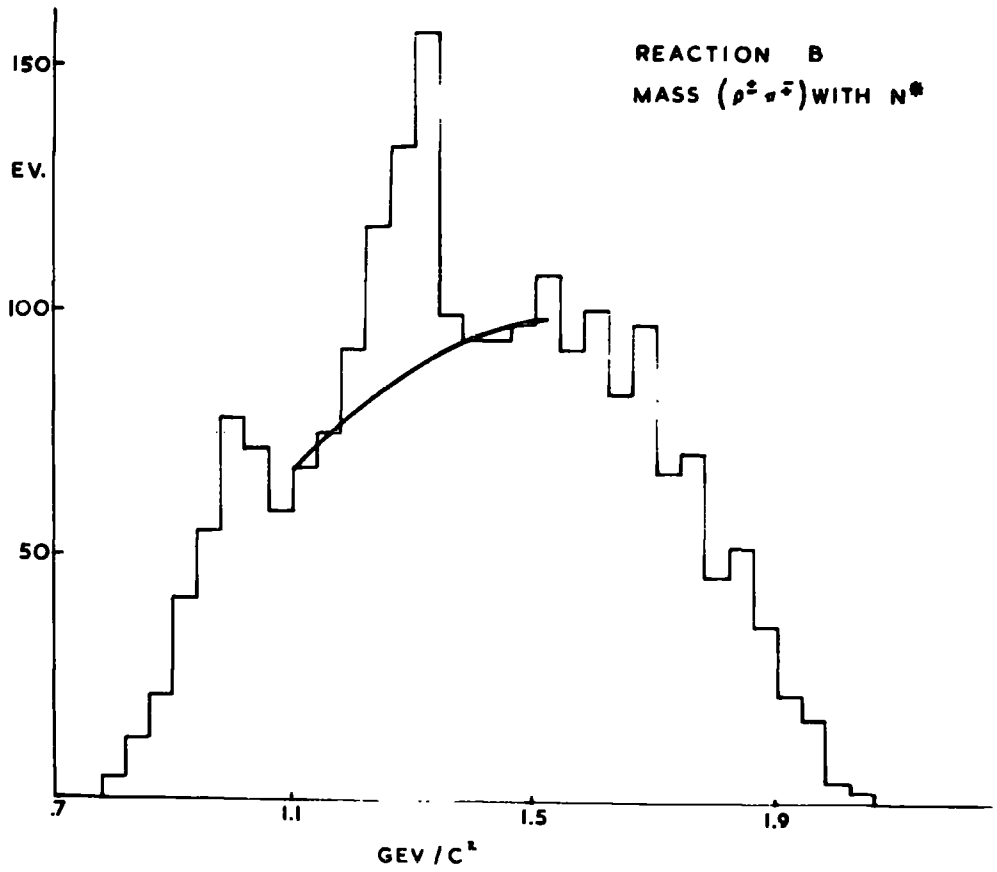


FIG. 43



is seen that the  $A_2$  is produced other than with an  $N^*$ , so one concludes that the cross-section for the production of  $N^* A_2$  ( $A_2 \rightarrow \rho\pi$ ) is  $89 \pm 13 \mu b$ .

The observation of the  $A_2$  decaying to  $\gamma^0\pi^+$  is discussed in chapter 6.

#### 5.4.6 The $B^+$ meson

Fig. 44 (a) shows the effective mass distribution for the  $\pi^+\pi^+\pi^-\pi^0$  system. Some enhancement in the region of 1.2 to 1.3  $\text{GeV}/c^2$  can be seen. Fig. 44 (b) shows the same distribution when the sample is restricted to those events in which a  $\pi^+\pi^-\pi^0$  combination is compatible with an  $\omega^0$  (743 to 823  $\text{MeV}/c^2$ ). The peak at the position of the B meson can be seen. The number of events above the background is estimated to be  $105 \pm 25$ .

The B meson was first observed in  $\pi^-p$  interactions by Bondar et al. (29) and in  $\pi^+p$  interactions by Abolins et al. (20). It was suggested by Maor and O'Halloran (30) that the peak could be the result of a Deck mechanism. The virtual dissociation of the incident pion into  $\rho\omega$  and the subsequent reaction  $\rho p \rightarrow \pi p$  should produce a broad peak in the neighbourhood of 1.2  $\text{GeV}/c^2$ . However, a significant B peak has been observed by Baltay et al. (31) in  $\bar{p}p$  annihilations, which confirms the existence of the B meson. For this reason, the peak observed here has been interpreted as being due to the production of the  $B^+$  meson.

FIG. 44

REACTION B

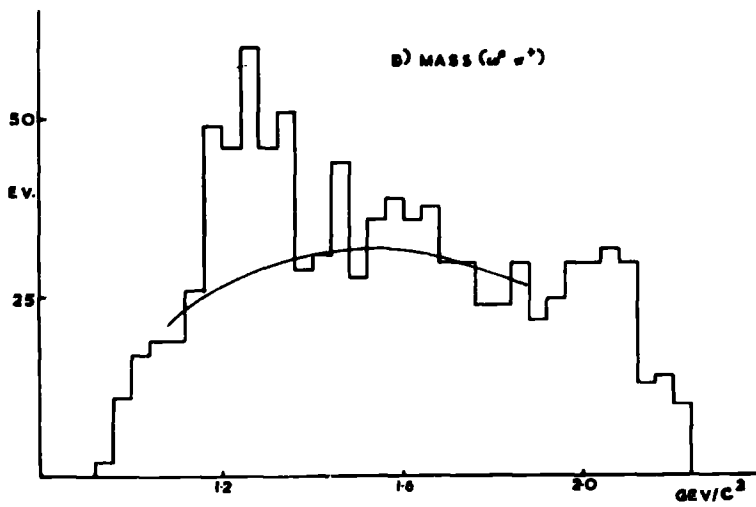
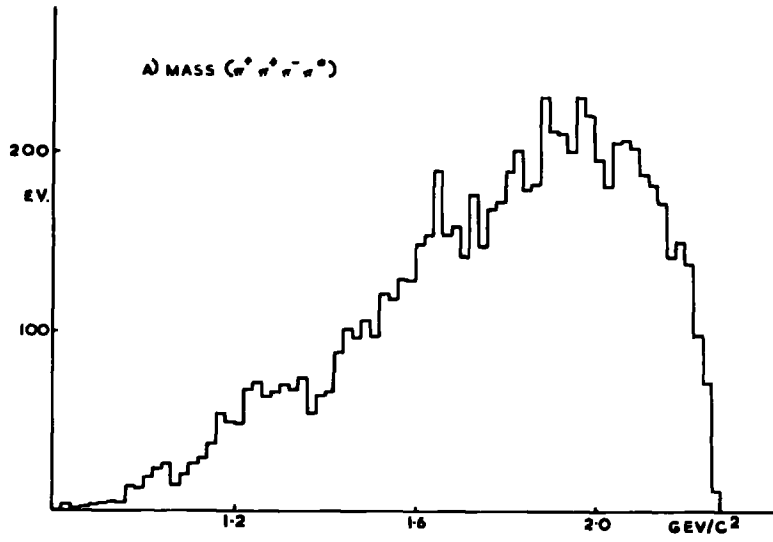


Fig. 45 gives the Dalitz plot for which the final state is compatible with  $\rho\pi^+\omega^0$ . The square of the effective mass of  $\rho\pi^+$  is plotted against the square of the effective mass of  $\pi^+\omega^0$ . Events in which both  $\pi^+\pi^-\pi^0$  combinations are compatible with an  $\omega^0$  are plotted for each value of the effective mass of  $\rho\pi^+$ . The strong production of  $N^*$  can be observed, as well as a faint band due to the  $B^+$  meson. The fact that there is a concentration of points along the whole length of the B band supports the  $J^P$  assignment of  $1^+$  for the B meson.

In order to study the decay angular distribution of the  $B^+$ , the angle  $\cos \theta_0$  is defined to be the angle between the incoming and the outgoing  $\pi^+$  (the one not produced by the  $\omega^0$  decay) in the centre of mass system of the final  $\pi^+\omega^0$  system (see fig. 46). Fig. 47 shows a scatter plot of the effective mass of  $\pi^+\omega^0$  versus  $\cos \theta_0$ .  $N^*\omega^0$  events are excluded and events in which either combination of  $\pi^+\pi^-\pi^0$  could be the decay products of an  $\omega^0$  are represented twice. A concentration of points at  $|\cos \theta_0| \approx 1$  is noticeable throughout the range of the mass of  $\pi^+\omega^0$ , but particularly at the larger values of the mass. The band corresponding to the  $B^+$  meson can be seen.

FIG. 45.  
MASS<sup>2</sup> ( $\omega^0 \pi^+$ ) VS. MASS<sup>2</sup> ( $P \pi^+$ ).

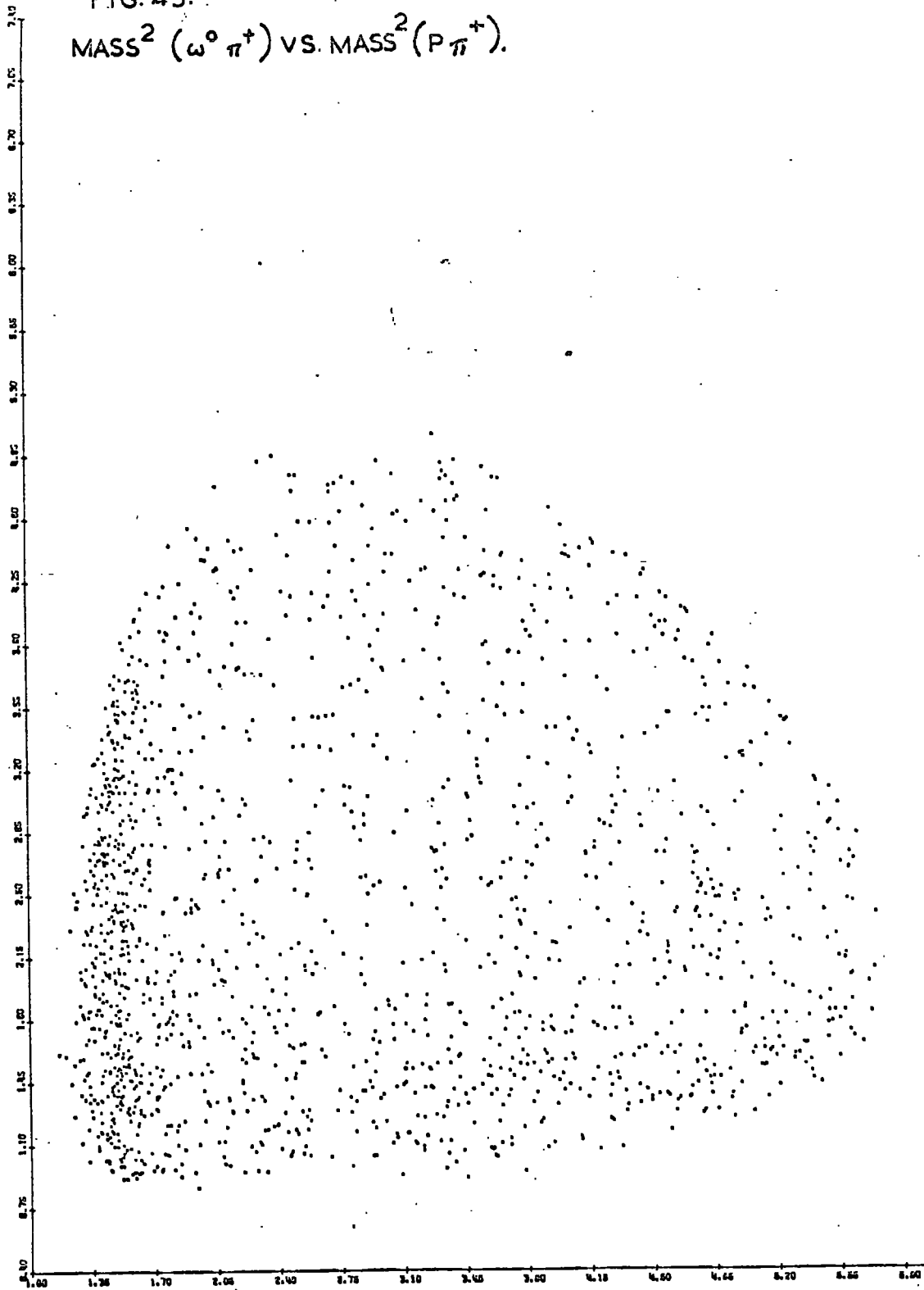


FIG. 46 DEFINITION OF  $\theta_0$

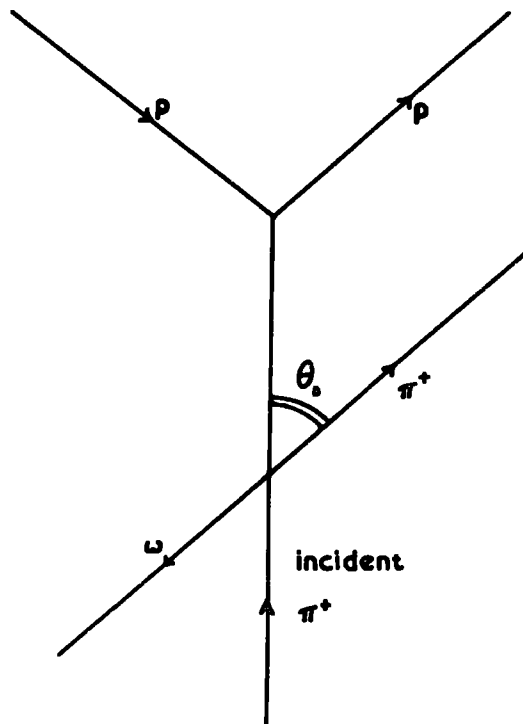
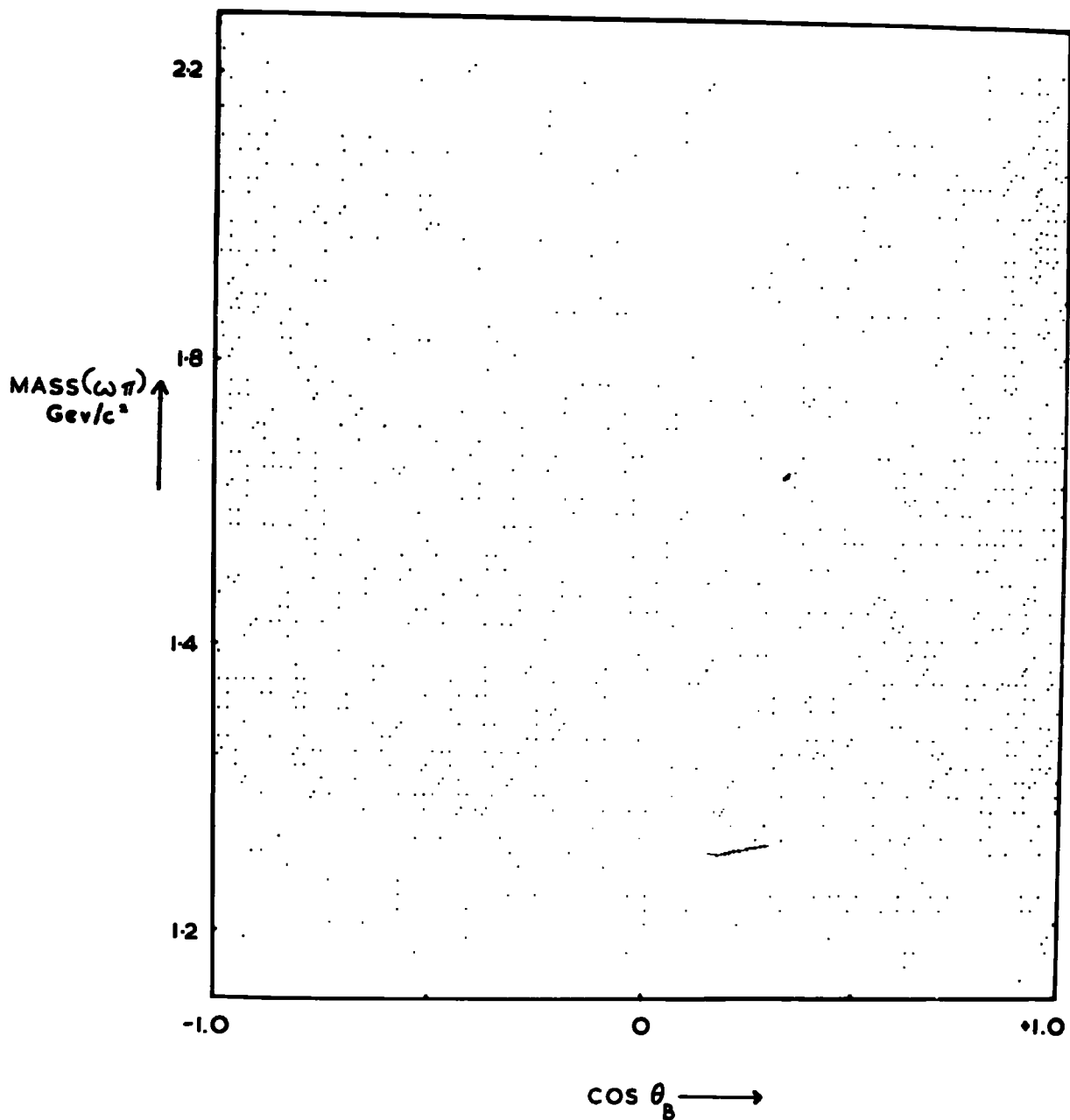


FIG. 47

MASS ( $\omega\pi$ ) vs  $\cos \theta_B$

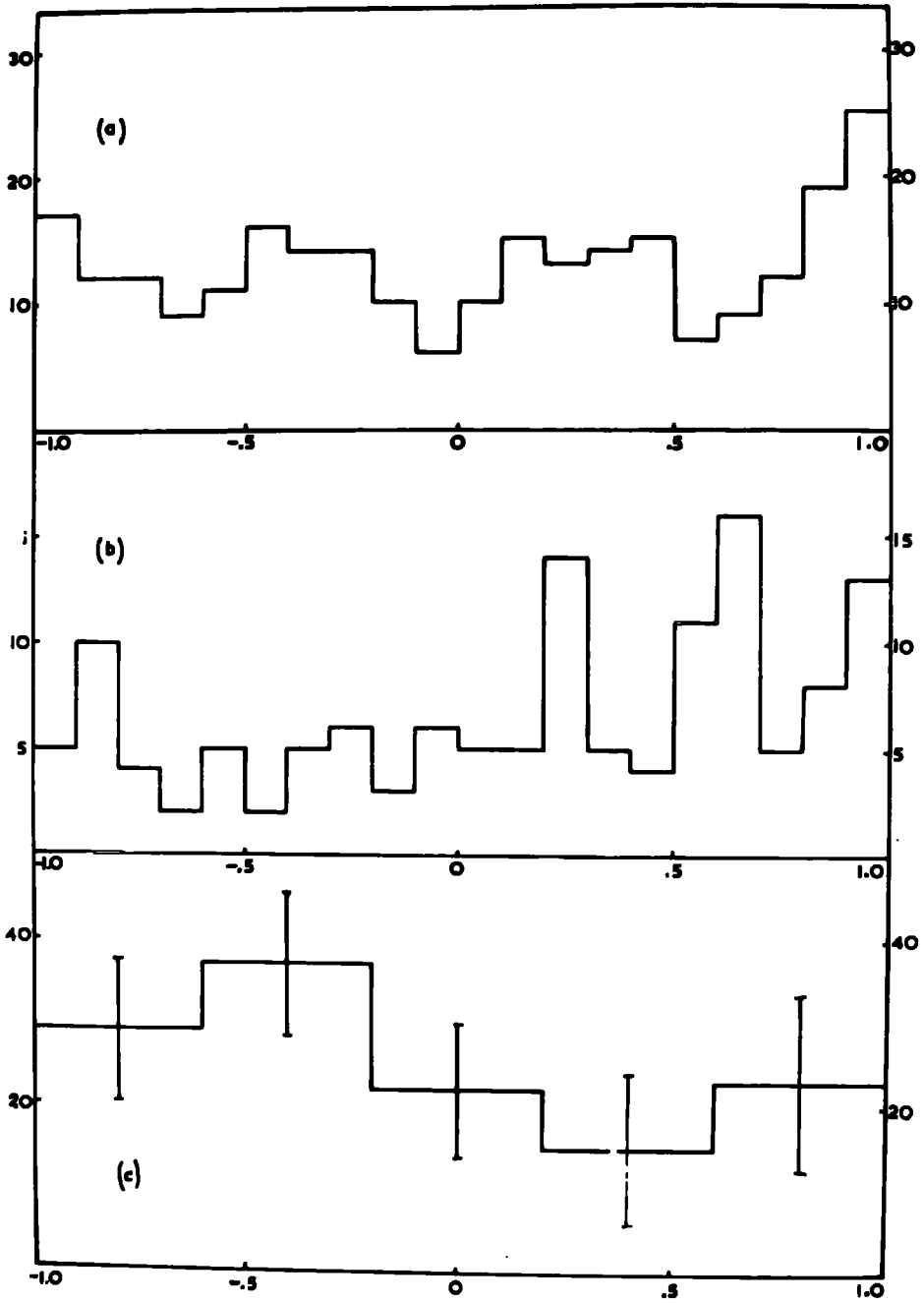


The projection of this scatter plot to give the angular distribution for the B-region is presented in fig. 48(a). The B-region is defined to be the mass interval 1.16 to 1.36 GeV/c<sup>2</sup>. Examination of fig. 44(b) shows that about 40% of the entries in the B-region corresponds to a B<sup>+</sup> meson. In order to estimate the effect that the remaining 60% would have on the distribution, control regions were defined by the mass intervals 1.06 to 1.16, and 1.36 to 1.46 GeV/c<sup>2</sup>. Fig. 48(b) shows the distribution of  $\cos \theta_B$  for the control regions. The difference of these two distributions presented in fig. 48 (c) is now the decay angular distribution for the B<sup>+</sup> meson. The statistical standard errors are indicated on this figure.

It can be seen that the angular distribution is isotropic. In fact, assuming an isotropic distribution one obtains that  $\chi^2 = 3.6$ , there being four degrees of freedom. The  $\chi^2$  probability is then 0.46. The best fit to a distribution of the form  $c + a \cos^2 \theta$  is with  $a = 0.1 \pm 0.3$ . The observed isotropic distribution supports the conclusion that the B<sup>+</sup> decay to  $\omega^0 \pi^+$  takes place in an S-state. The J<sup>P</sup> assignment would then be 1<sup>+</sup>.

FIG. 48

$\cos \theta_B$  DISTRIBUTION.



A study of the  $J^P$  assignment of the  $B^+$  meson has been made by Carmony et al (32) who find that the best fit to their data is with the  $1^-$  assignment, although the fit is not a good one, and the  $1^+$  and  $2^-$  assignments are still possible. If the B meson were a  $1^+$  meson the decays to  $K\bar{K}$  and to  $2\pi$  would be forbidden by the conservation of parity. Moreover, if the B were a  $1^-$  meson one would expect to see these decays. The rate of the decay of B to  $K\bar{K}$  has been determined by Hess (33) to be less than 2% of the rate of decay to  $\omega\pi$  and the rate of decay to  $2\pi$  has been found by the ABBBHLM Collaboration (35) to be less than 30%. The fact that these decay modes have not been observed is evidence against the  $J^P$  assignment of  $1^-$  for the B meson.

The projection of Fig. 47 to give the effective mass distribution of  $\omega^0\pi^+$  is given for  $|\cos\theta_0| < 0.5$  in fig. 49(a), and for  $|\cos\theta_0| > 0.5$  in fig. 49(b).

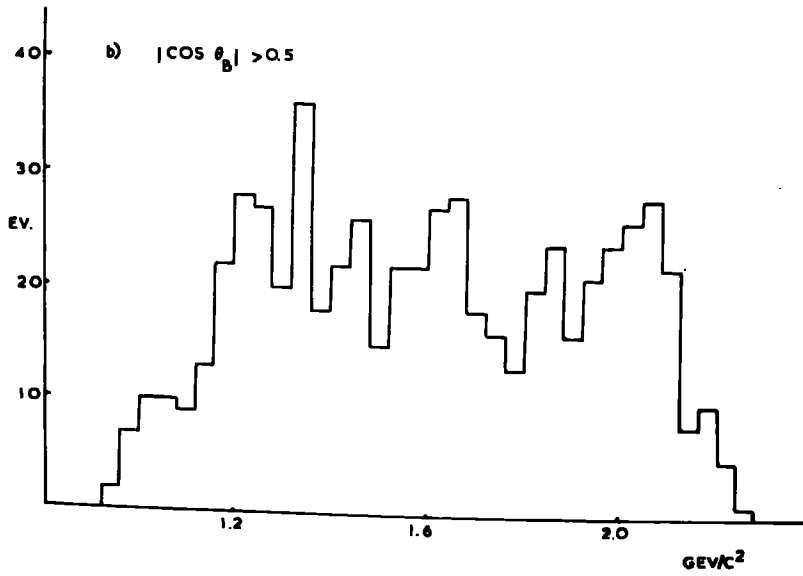
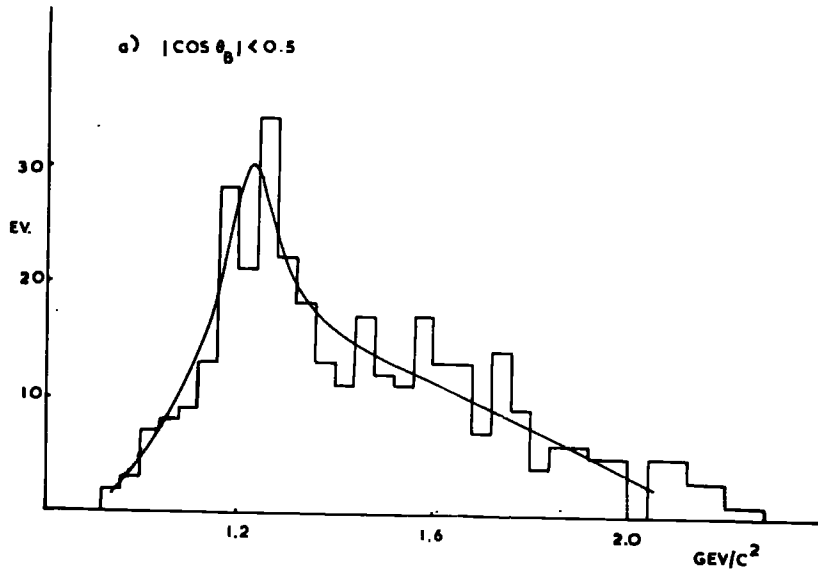
The B meson peak is clearer in the first of these. An attempt was made to fit the distribution of fig. 49(a) in order to obtain a value for the mass and the width of the B as follows:

The background of the distribution was estimated

FIG. 4R

MASS ( $\omega^0 \pi^+$ )

REACTION B



by fitting a third order polynomial curve to the mass intervals 0.96 to 1.1, and 1.4 to 2.2 GeV/c<sup>2</sup>. The experimental distribution in the range of 1.04 to 2.0 GeV/c<sup>2</sup> was fitted by minimum  $\chi^2$  to a distribution of the form of the sum of the background and a Breit-Wigner function:-

$$N\Gamma^2 / (\Gamma^2 + (M^2 - M_0^2)^2 / M_0^2)$$

Where N is proportional to the number of events in which a B<sup>+</sup> is produced.

$\Gamma$  is the full width of the peak

$M_0$  is the central mass value of the peak and M is the  $\pi^+\omega^0$  effective mass.

The best fit was obtained with  $\Gamma = 125 \pm 30$  MeV/c and  $M_0 = 1230 \pm 20$  MeV/c<sup>2</sup>. The estimated standard errors quoted here are such that a deviation of one standard error on either of these quantities would increase the  $\chi^2$  value to one more than the minimum (17.4 for 18 degrees of freedom). The fitted distribution is shown on fig. 49(a). The values obtained for the width and the mass of the B meson are compared with those obtained in other

experiments in the table below. The values obtained in this experiment are in good agreement with those from other experiments.

Table 16  
Mass and Width of B meson

|                      | Mass<br>MeV/c <sup>2</sup> | Width<br>MeV/c <sup>2</sup> |
|----------------------|----------------------------|-----------------------------|
| Abolins et al.(20)   | 1220                       | 100 ± 20                    |
| Chung et al.(36)     | 1220                       | 180 ± 30                    |
| Goldhaber et al.(37) | 1220                       | 80                          |
| Baltay et al. (31)   | 1200 ± 15                  | 100 ± 30                    |
| This experiment      | 1230 ± 20                  | 125 ± 30                    |

### 5.5 Reaction E

In this section, the reaction  $\pi^+ p \rightarrow p \pi^+ K^+ K^-$  is studied. Events which have also been successfully fitted with a hypothesis of reaction A have not been included in the sample of events. 309 events of reaction E are studied here. By a Monte Carlo generation of events of reaction B, it was found that about 1% of such events would give a spurious fit to reaction E. From the number of events of reaction B, one would then expect about 60 to give

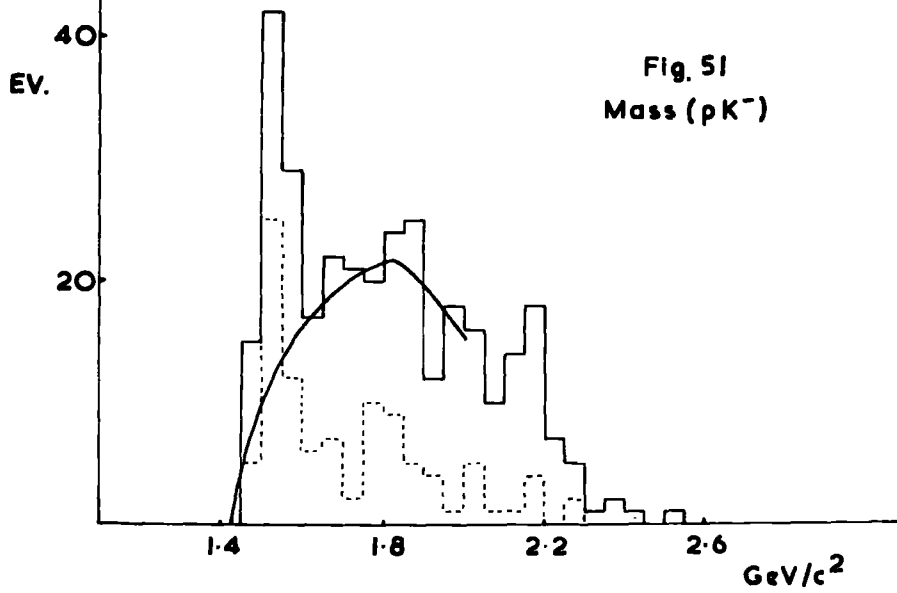
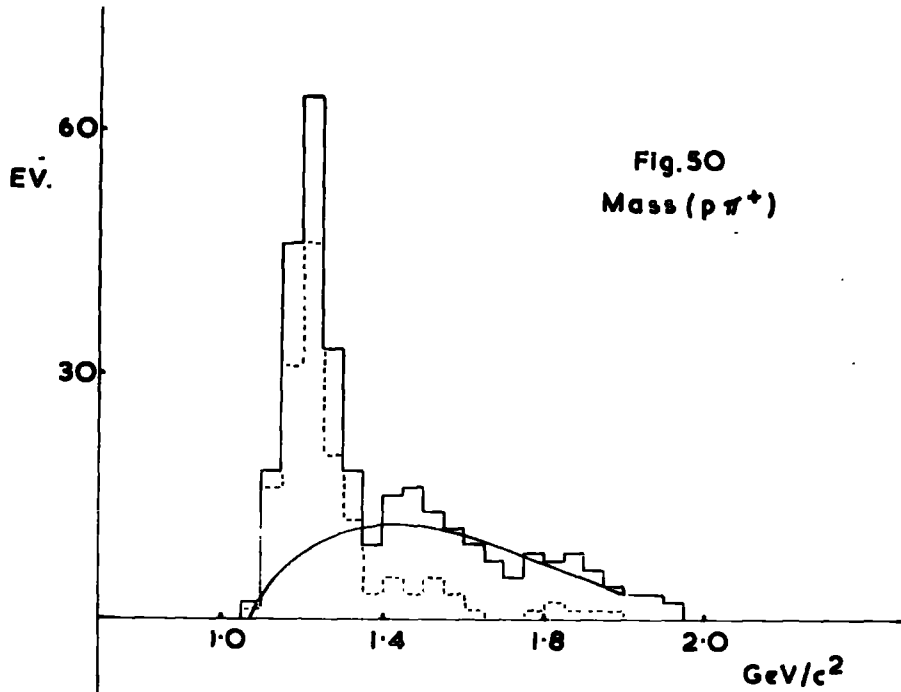
a fit to reaction E, and the sample of events would have a contamination of about 20% by spurious fits. By generating events of reaction E 70% were found to give a spurious fit to reaction B so the acceptance of the 4c fit to the 1c fit is justified.

Fig. 50 shows the effective mass distribution for the  $p\pi^+$  combination. The peak due to the production of  $N^*$  can be clearly seen. The number of events above the smooth background in the region of the  $N^*$  is estimated to be  $137 \pm 17$  which corresponds to a cross-section for the production of  $N^*$  in this reaction of  $47 \pm 6 \mu\text{b}$ . The dashed histogram shows the effective mass distribution for events in which the four momentum transfer is less than  $1.0 \text{ GeV}^2$ .

In fig. 51 is presented the distribution of the effective mass of  $p K^-$ . The production of  $Y^*$  (1520) is observed and by estimating the number of events above a smooth background, the cross-section for the production of  $Y^*$  (1520) and its decay to  $p K^-$  is found to be  $16 \pm 4 \mu\text{b}$ . This resonance is also produced peripherally as can be seen from the dashed histogram on this figure, which is the effective mass distribution for events in which the four momentum transfer is less than  $1.0 \text{ GeV}^2$ :



REACTION E



The effective mass distribution of the  $K^-\pi^+$  system is shown in fig. 52. A strong signal at the position of the  $K^*(890)$  is observed. The number of events in this peak above the estimated background corresponds to a cross-section for the production of  $K^*(890) \rightarrow K^-\pi^+$  of  $12 \pm 5 \mu\text{b}$ . A peak at the position of the  $\kappa(730)$  meson is also seen on this distribution the cross-section being estimated as  $3.5 \pm 2 \mu\text{b}$ . The shaded histogram on the figure gives the same distribution excluding events in which an  $N^*$  could have been produced i.e. in which the effective mass of the  $p\pi^+$  system is found to be in the range 1.12 to 1.32  $\text{GeV}/c^2$ . Both of the peaks appear more pronounced after this rejection. The cross-sections for the production of  $K^*(890)$  and of  $\kappa(730)$  in this reaction have been re-estimated using this distribution. The values obtained are  $10 \pm 3 \mu\text{b}$ . and  $4 \pm 1.5 \mu\text{b}$ . respectively.

The distribution of the effective mass of  $K^+K^-$  is plotted in fig. 53. The peak due to the decay of the  $A_2$  meson into  $K^+K^-$  can be seen. The cross-section for this process is estimated to be  $7 \pm 3.5 \mu\text{b}$ .

REACTION E

FIG. 52

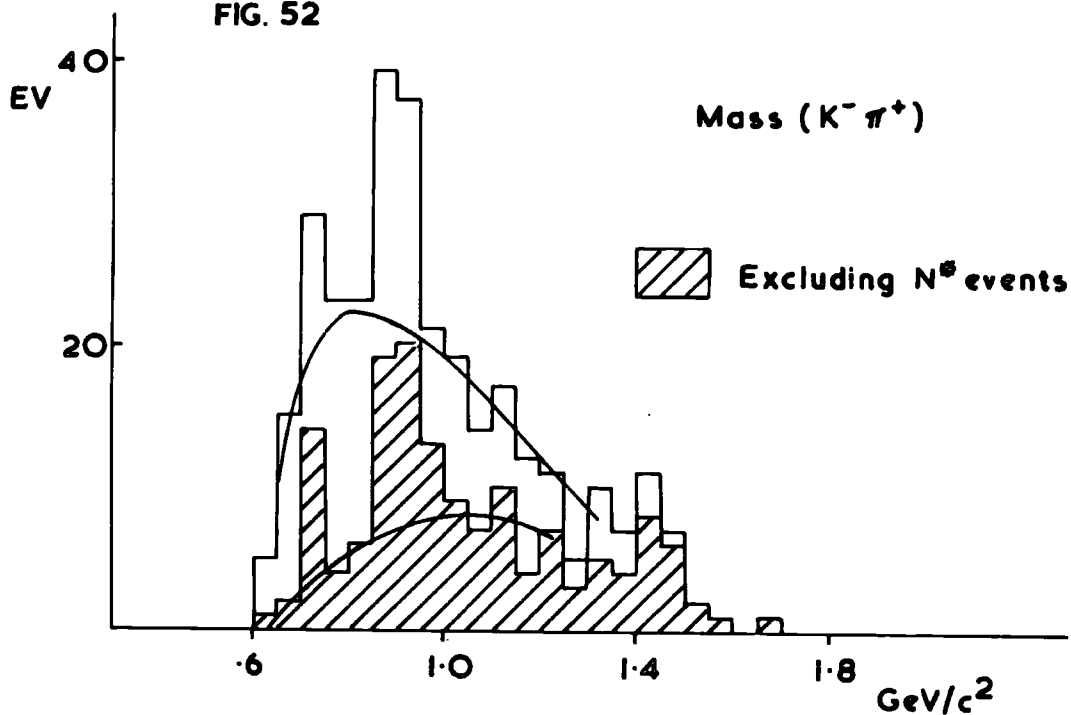
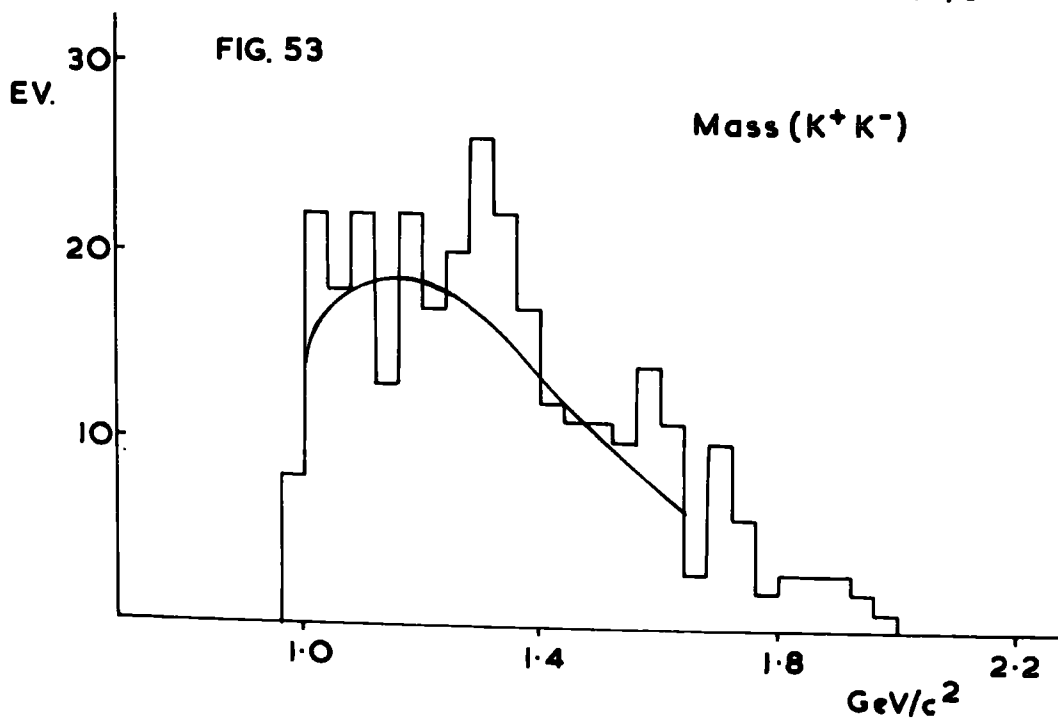


FIG. 53



CHAPTER 6

THE PRODUCTION AND DECAY OF THE A<sub>2</sub> MESON

6.1 Introduction

In this chapter the production of the A<sub>2</sub> meson is studied and the branching ratio into its different decay modes is examined. The decay of the A<sub>2</sub> into  $\rho\pi$ ,  $\gamma\pi$  and  $K\bar{K}$  have all been observed and measured in various experiments and the results of this experiment are compared with those of other authors.

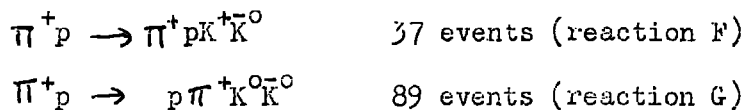
The A<sub>2</sub> is observed to be produced in two reactions namely:-



Different decay modes of the A<sub>2</sub> are observed in both of these reactions and in the second reaction there is evidence for the production of N<sup>+</sup>A<sub>2</sub><sup>+</sup>. The relative rates of the different charge states for reaction (2) is of course predictable from Clebsch-Gordan coefficients and the predictions are examined experimentally.

In determining the branching ratio for the  $K\bar{K}$  mode, an examination is made of events which were measured as a separate part of the complete 5 GeV/c

experiment. Two pronged events with at least one visible  $V^0$  decay have been selected and measured. The system of analysis of these has been the same as for the four pronged events. Only two of the fitted hypotheses for the events is of interest here and these are:



For the samples of these events, the cross-section is 0.30 per event found. It should be noted that if the  $K^0$  (or  $\bar{K}^0$ ) decays by the short-lived mode,  $K_S$ , it will almost certainly decay within the chamber. As about two thirds of such decay is to  $\pi^+ \pi^-$ , and one third to  $\pi^0 \pi^0$  one expects to see two thirds of  $K_S$  decays. The  $K_L$  decays are unlikely to be seen in the chamber, and the measurement is not likely to give a kinematic fit to a two pion decay.

Recent suggestions that the  $A_2$  peak consists of two separate resonances with different decay modes are also discussed.

## 6.2 The reaction $\pi^+ p \rightarrow p A_2^+$

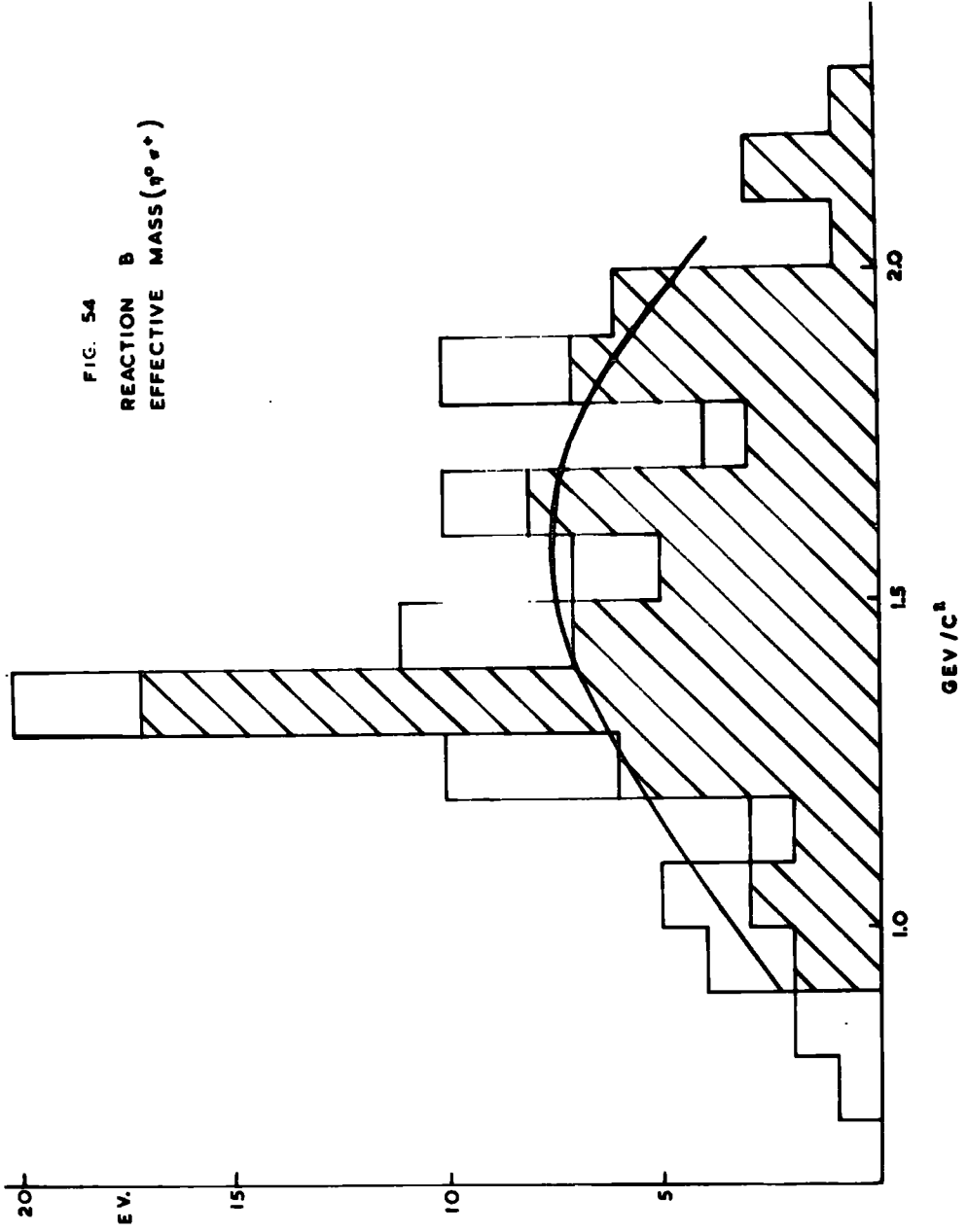
In this reaction it is possible to observe the three decay modes of the  $A_2^+$ . The decay to  $\rho^0 \pi^+$  is observable in reaction A, the  $\eta^0 \pi^+$  decay mode is seen in reaction B, and the  $K\bar{K}$  mode is seen in reaction F.

The production of  $A_2^+$  in reaction A has already been discussed. The cross-section for this process was estimated to be  $58 \pm 10 \mu\text{b}$ . This value must be corrected for the unobserved decay  $A_2^+ \rightarrow \rho^+ \pi^0$ , which is expected from Clebsch-Gordan coefficients to occur at the same rate as the decay to  $\rho^0 \pi^+$ . The cross-section for  $A_2 \rightarrow \rho \pi$  is therefore  $116 \pm 20 \mu\text{b}$ . It is possible to try to estimate the parameters of the peak by taking the median value of the events in the excess above background for the mass, and a rough estimate of the width of the peak is possible. Examination of fig. 33 then gives the values of  $1305 \pm 15 \text{ MeV}/c^2$  for the mass of the  $A_2$ , and  $100 \pm 20 \text{ MeV}/c^2$  for the width. Chikovani et al (38) have reported that the  $A_2$  peak is really two separate peaks. No evidence for the splitting of the  $A_2$  peak can be observed in this distribution.

Evidence of the  $\eta^0 \pi^+$  decay mode of the  $A_2^+$  is seen in reaction B. Fig. 54 shows the effective mass spectrum of

$\eta^0 \pi^+$ , where for this purpose the  $\eta^0$  selection was defined as a  $\pi^+ \pi^- \pi^0$  system with an effective mass in the range 535 to 565  $\text{MeV}/c^2$ .

FIG. 54  
REACTION B  
EFFECTIVE MASS ( $^{\circ}\pi^{\circ}$ )



An examination of fig. 36 shows that a large proportion of the selected  $\pi^+\pi^-\pi^0$  combinations corresponds to an  $\eta^0$ . A peak in the  $A_2$  region of the  $\gamma\pi$  mass spectrum can be seen. The peak remains after the exclusion of  $N^*\eta^0$  events, where the mass of the  $N^*$  band is defined as 1.12 to 1.32  $\text{GeV}/c^2$ . This distribution is shown as a shaded histogram on fig. 54. As the background is rather less after the exclusion of  $N^*\eta^0$  events, this distribution has been used to estimate the parameters of the peak. The mass and width of this peak are estimated to be  $1320 \pm 30 \text{ MeV}/c^2$  and  $100 \pm 50 \text{ MeV}/c^2$  respectively. These values are consistent with those obtained for the  $\rho\pi$  peak. The estimated number of events above a smooth background is  $19 \pm 5$  and the cross-section for the observation of the  $\gamma\pi$  decay mode is  $8.5 \pm 2 \mu\text{b}$ . The branching ratio of the  $\eta^0$  is such that 27% of the decays are to  $\pi^+\pi^-\pi^0$  and to  $\pi^+\pi^-\gamma$ . It is not likely that the kinematic fitting can distinguish these, and so both of these modes will be observed in spite of the false assignment. Correcting for unseen decays, the cross-section for the  $\gamma\pi$  decay mode of the  $A_2$  is  $31 \pm 10 \mu\text{b}$ . This then leads to a value for the branching ratio:

$$A_2 \rightarrow \gamma\pi / A_2 \rightarrow \rho\pi = 0.27 \pm 0.09$$

The values reported by other experiments are set out in the table below:

Table 17

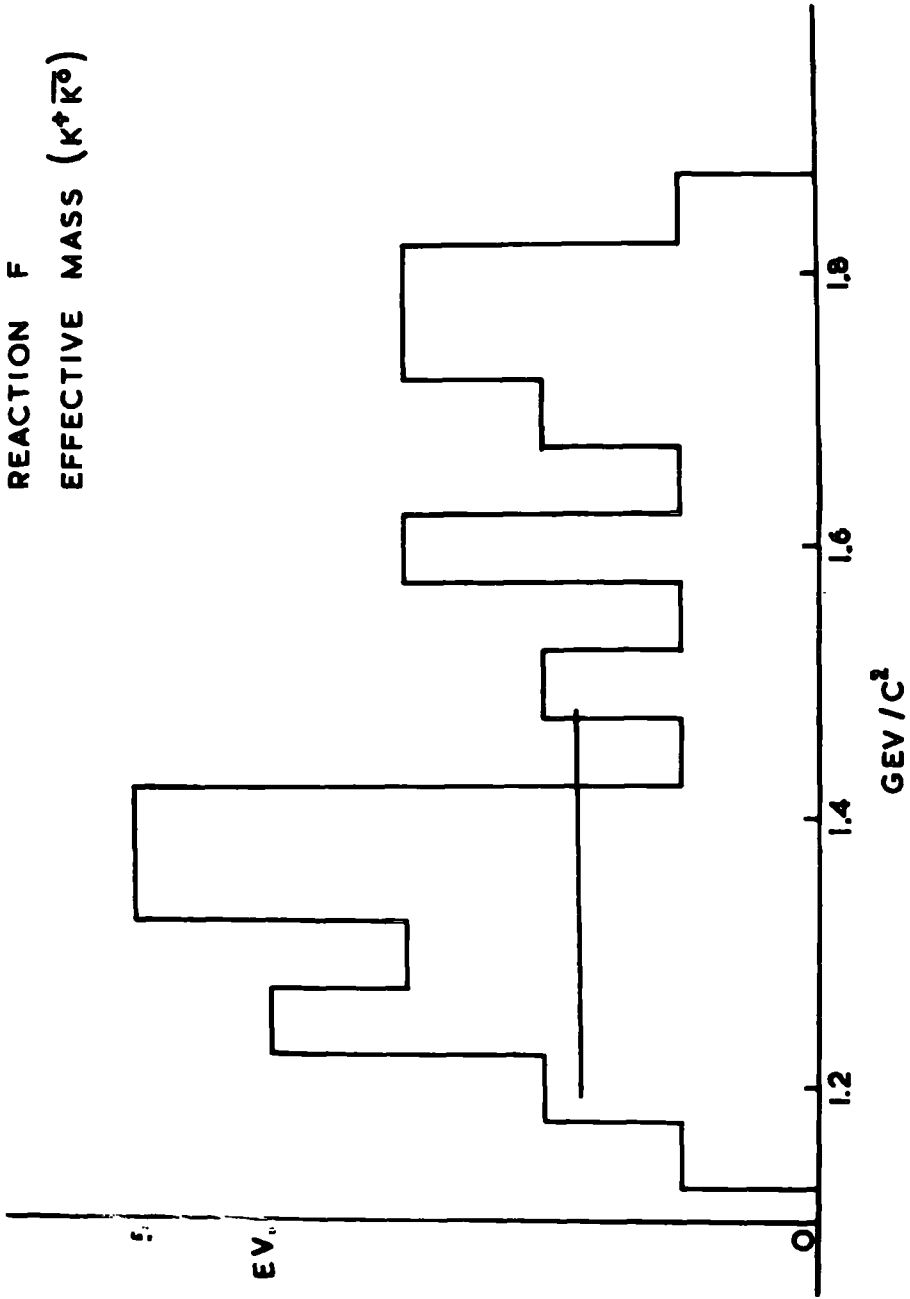
Branching ratio  $A_2 \rightarrow \gamma\pi / A_2 \rightarrow \rho\pi$

|                       |      |                 |
|-----------------------|------|-----------------|
| ABBBHLM collaboration | (22) | $0.3 \pm 0.2$   |
| Chung et al.          | (39) | $0.12 \pm 0.08$ |
| Dubovikov et al.      | (40) | $0.24 \pm 0.08$ |
| ABC collaboration     | (41) | $0.09 \pm 0.04$ |
| GHMS collaboration    | (42) | $0.18 \pm 0.08$ |
| This experiment       |      | $0.27 \pm 0.09$ |

The value obtained in this experiment is in good agreement with those from other experiments. It is possible to take a weighted mean of the six quantities, and in doing so, this experiment would contribute 10% of the weight. If this is done, one obtains for the branching ratio, the value  $0.15 \pm 0.03$ . The value of  $\chi^2$  is 6.1 for five degrees of freedom, so all the values obtained are in reasonable agreement with each other.

The decay of the  $A_2$  is observable in reaction F. Fig. 55 shows the distribution of the effective

FIG. 55



mass of  $K^+K^0$  for this reaction. The peak in the  $A_2$  region can be seen, and the mass ( $1350 \pm 30 \text{ MeV}/c^2$ ) and width ( $125 \pm 50 \text{ MeV}/c^2$ ) of this peak are in reasonable agreement with the  $A_2$  meson. It is estimated that there are  $10 \pm 4$  events above the background in this region corresponding to a cross-section of  $3.0 \pm 1.2 \mu\text{b}$ . Correcting for the  $K_L$  decays and the neutral  $K_S$  decays one obtains that the cross-section for  $A_2 \rightarrow K\bar{K}$  is  $9 \pm 4 \mu\text{b}$ , and the branching ratio can be calculated:

$$A_2 \rightarrow K\bar{K} / A_2 \rightarrow \rho\pi = 0.08 \pm 0.04$$

### 6.3 The reaction $\pi^+p \rightarrow N^* A_2$

In this reaction it is possible to observe two of the decay modes of the  $A_2$ . The decay to  $\rho\pi$  is observable in reaction B. The decay to  $K\bar{K}$  is observable as  $K^+K^-$  in reaction E, and as  $K^0\bar{K}^0$  in reaction G.

The production of  $N^* A_2$  in reaction B has already been discussed, and the cross-section was found to be  $89 \pm 13 \mu\text{b}$ . The mass and the width of the peak in fig. 43 are estimated to be  $1300 \pm 20 \text{ MeV}/c^2$  and  $140 \pm 40 \text{ MeV}/c^2$ .

These values are in reasonable agreement with those found in the previous section.

In fig. 56 (a), the scatter diagram of the effective mass of  $p\pi^+$  versus the effective mass of  $K^+K^-$  for events of reaction E is presented. The band due to the production of  $N^*$  can be seen clearly. In this band, a concentration of points in the  $N^* A_2$  production region can be seen. Fig. 56 (b) shows the effective mass distribution for  $K^+K^-$  if the associated  $p\pi^+$  has an effective mass in the  $N^*$  band (defined as 1.14 to 1.30  $\text{GeV}/c^2$ ). A peak at the position of the  $A_2$  is observed. The mass and width of this peak are estimated to be  $1340 \pm 40$  and  $120 \pm 40$   $\text{MeV}/c^2$  respectively which are in good agreement with the expected values for the  $A_2$ . The number of events in the peak above the estimated background is  $16 \pm 8$  which corresponds to a cross-section of  $7.2 \pm 3.6 \mu\text{b}$ . for this process.

Fig. 57 (a) is the scatter diagram of the effective mass of  $p\pi^+$  against the effective mass of  $K^0\bar{K}^0$ . Again a concentration of points in the  $N^* A_2$  region can be noticed, and in fig. 57 (b), the distribution of the effective mass of  $K^0\bar{K}^0$  associated with an  $N^*$  is shown. Once more, a peak

FIG. 56

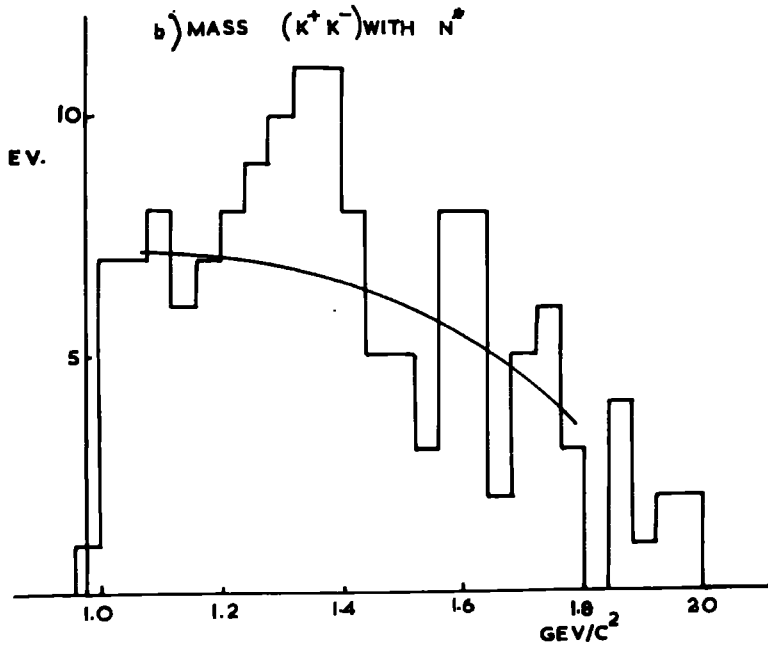
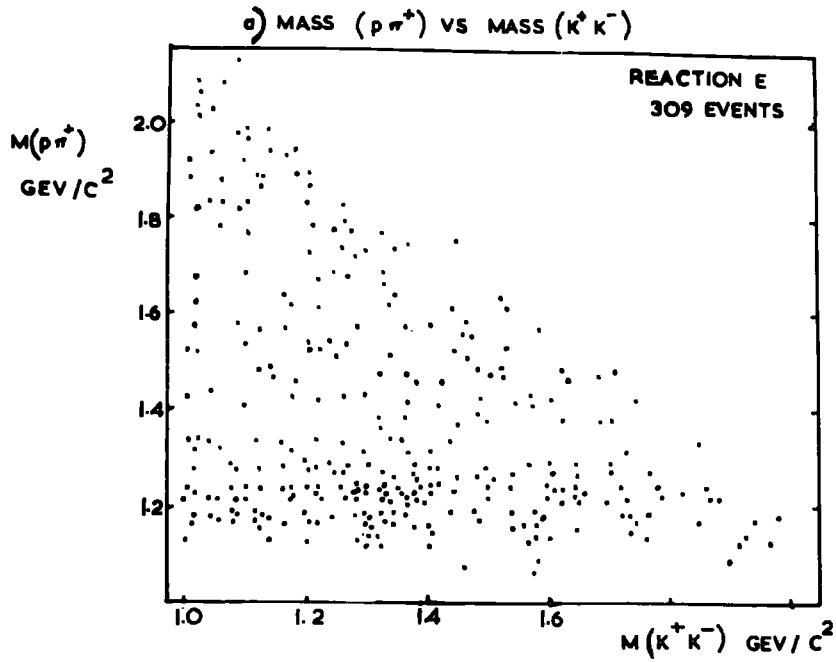
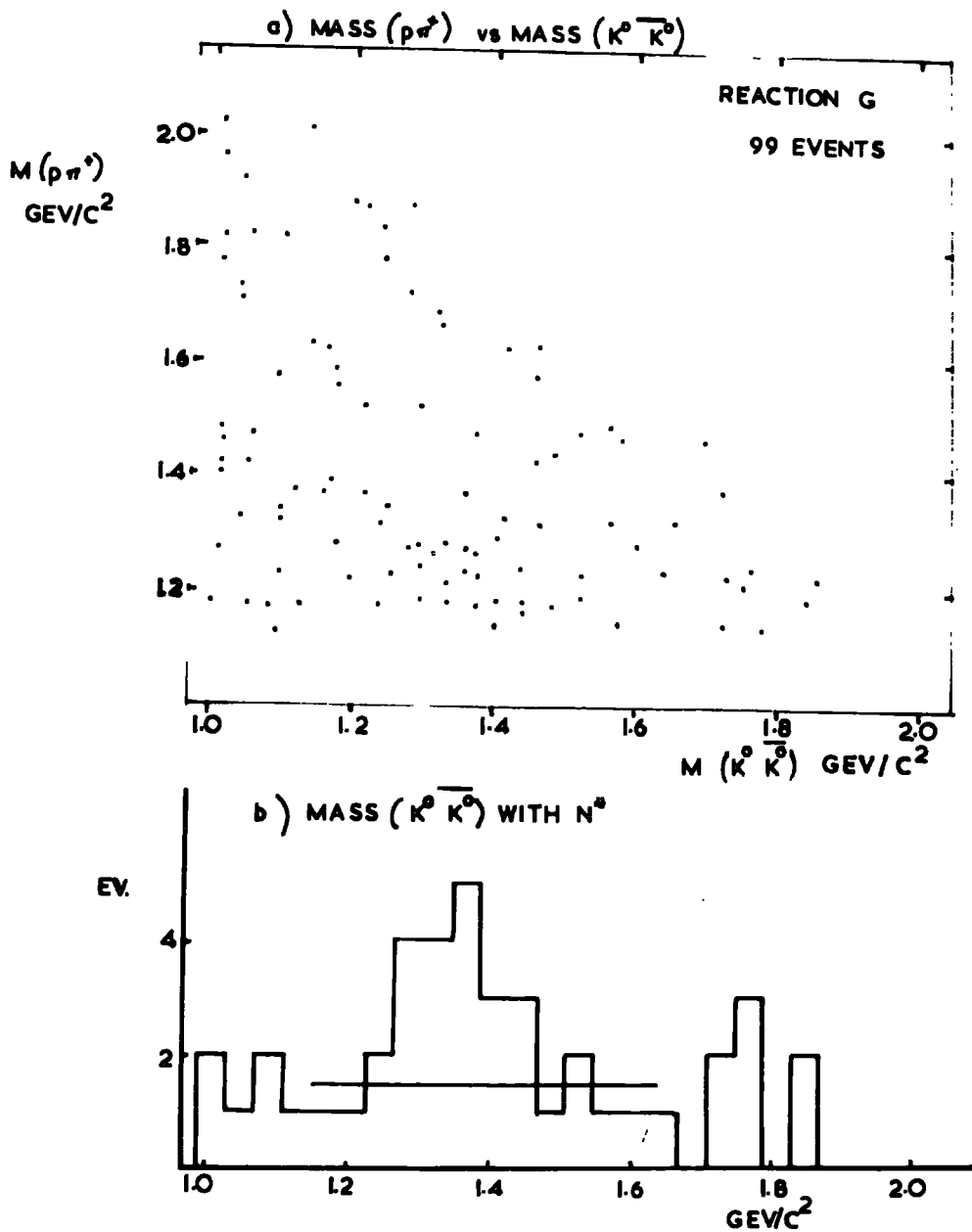


FIG 57



at  $1360 \pm 40 \text{ MeV}/c^2$  is observed. These values are compatible with the values for the  $A_2$  meson. The number of events in this peak is estimated to be  $12 \pm 5$ . If the quantum numbers of the  $A_2$  are the accepted ones, in particular that  $I$  is  $1^-$ , the branching ratio of the  $A_2$  to  $K^+K^-$ ,  $K_S K_S$ ,  $K_L K_L$ ,  $K_S K_L$  should be in the ratio 2:1:1:0. Since the  $K\bar{K}$  systems being studied here are those in which at least one of the decays is observed, it follows that the  $K_S K_S$  mode is being observed, and that there is no contribution from  $K_S K_L$ . The probability that at least one decay of  $K_S K_S$  should be observed is 8/9. Correcting for unseen decays one obtains a cross-section for  $A_2 \rightarrow K_S K_S$  of  $4.0 \pm 1.7 \mu\text{b}$ .

The ratio of the decay modes  $K^+K^-$  and  $K_S K_S$  is therefore  $1.8 \pm 1.2$  which is in good agreement with the expected value of 2. Assuming the relative rates of decay to be as expected, it is found that the cross-section for the decay mode  $A_2 \rightarrow K\bar{K}$  is  $15 \pm 5 \mu\text{b}$ . From this the branching ratio  $A_2 \rightarrow K\bar{K} / A_2 \rightarrow \rho\pi$  is calculated to be  $0.17 \pm 0.06$ .

6.4 The  $A_2 \rightarrow K\bar{K}/A_2 \rightarrow \rho\pi$  branching ratio

Two independent estimations have thus been made of the  $K\bar{K}$  branching ratio in this experiment. The difference between the two values is  $0.09 \pm 0.07$  so there is some disagreement between the values. The two values are not however inconsistent. Taking the weighted mean one finds for the branching ratio  $A_2 \rightarrow K\bar{K} / A_2 \rightarrow \rho\pi, 0.11 \pm 0.04$ . The values obtained by other experiments are listed in the table below.

Table 18

Branching ratio  $A_2 \rightarrow K\bar{K} / A_2 \rightarrow \rho\pi$

|                        |                   |
|------------------------|-------------------|
| Lander et al. (43)     | $<0.08$           |
| Armenteros et al. (44) | $<0.04$           |
| Chung et al. (39)      | $0.053 \pm 0.021$ |
| ABC collaboration (41) | $0.04 \pm 0.02$   |
| This experiment        | $0.11 \pm 0.04$   |

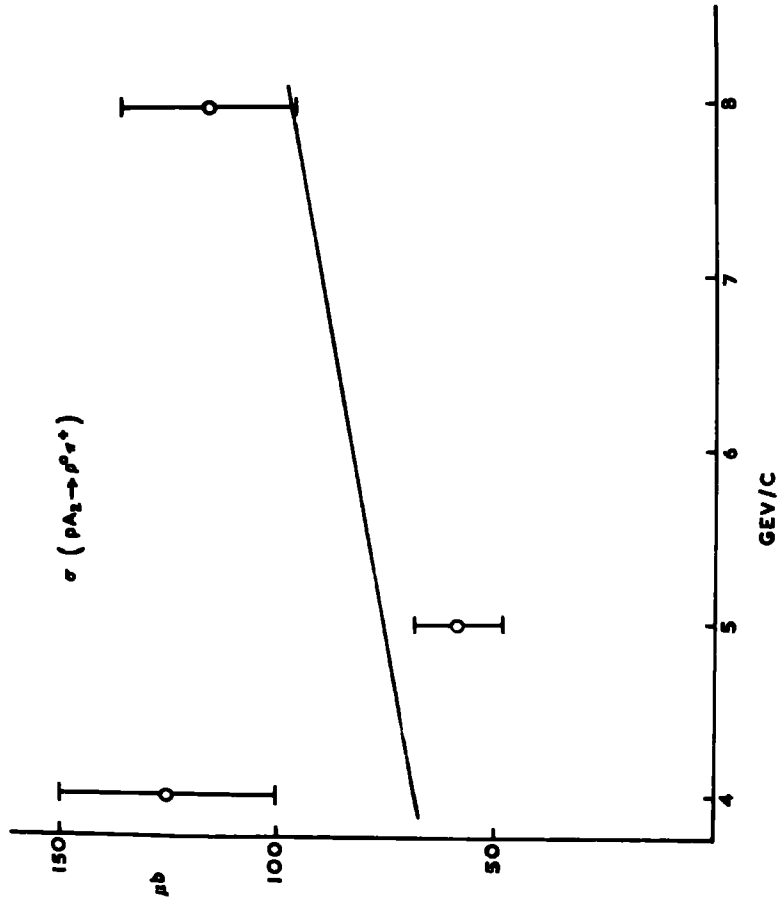
The branching ratio obtained by this experiment is rather high compared with that found in other experiments. One possible explanation of this lies

in the fact that the cross-section found for the production of  $pA_2$  ( $A_2 \rightarrow \rho^0 \pi^+$ ) is rather low in comparison with other experiments (see fig. 58). One can attempt to obtain from the three experiments a better value for the cross-section. Assuming a linear variation over the range considered, the best fit is shown on the figure, although the fit is not a good one. The value thus obtained for the reaction  $\pi^+ p \rightarrow pA_2$  ( $A_2 \rightarrow \rho^0 \pi^+$ ) at 5 GeV/c is  $75 \pm 15 \mu\text{b}$ . This would give for the branching ratio  $A_2 \rightarrow \gamma\pi / A_2 \rightarrow \rho\pi$ ,  $0.21 \pm 0.08$  which is in even better agreement with other experiments. Indeed the weighted mean for this and other experiments for this branching ratio would become  $0.20 \pm 0.04$ .

Following the same procedure for the  $K\bar{K}$  branching ratio in the reaction  $pA_2$ , the value  $0.06 \pm 0.03$  is obtained. The high value obtained from the  $N^* A_2$  reaction remains unexplained although it is not altogether inconsistent with this value. The weighted mean from the two reactions is  $0.08 \pm 0.03$  which is in reasonable agreement with other experiments.

A further possibility is that there are two resonances at the  $A_2$  position having different decay modes. This hypothesis would be supported

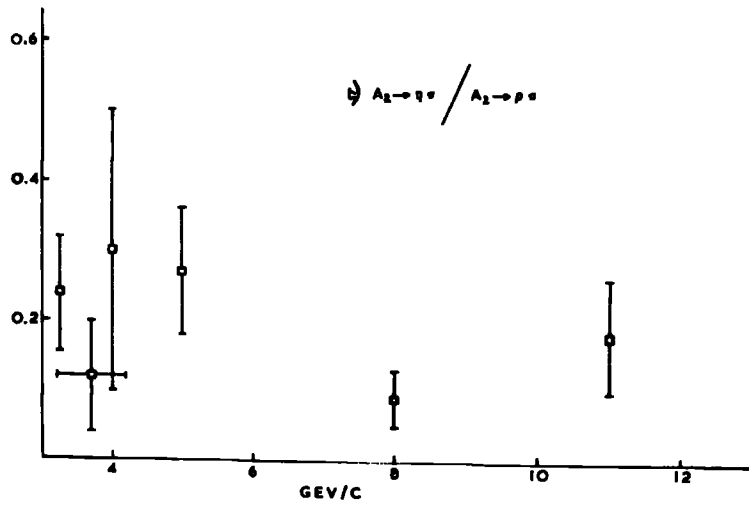
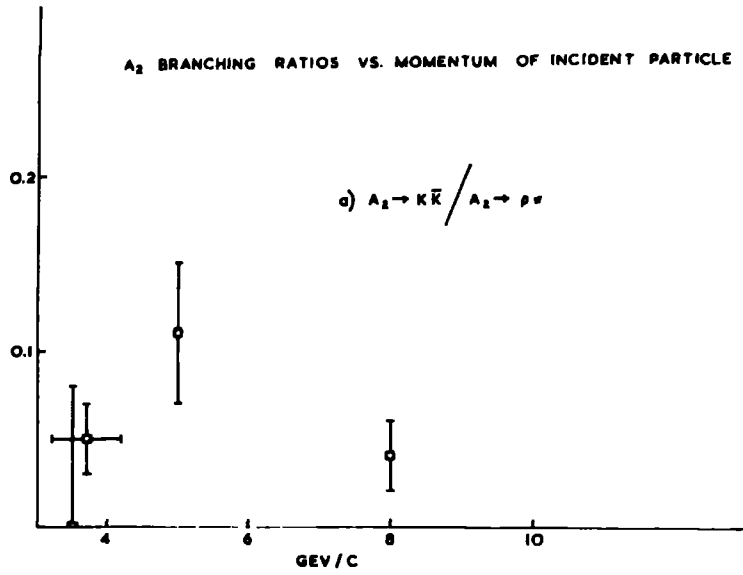
FIG. 5B  $\sigma(\rho A_2 \rightarrow \rho^0 \sigma^+)$  vs. MOMENTUM OF INCIDENT  $\sigma^+$



by the missing mass spectrometer experiment of Chikovani et al. (38) in which some slight evidence for two peaks is found. In this experiment there does seem to be a slight difference in the central mass values of the peaks being  $1300 \pm 15 \text{ MeV}/c^2$  for the  $\rho\pi$  peaks, and  $1350 \pm 20 \text{ MeV}/c^2$  for the  $K\bar{K}$  peaks. The difference between these corresponds to about two standard deviations, but it should also be noted that the estimation of the standard error on the central mass value of the peaks is rather uncertain so definite conclusions about a significant mass difference can not be made.

Morrison (45) has suggested the possibility of a meson with a mass similar to the  $A_2$ , but with  $J^P = 2^-$  or  $1^+$ , which would decay to  $\rho\pi$  but the decays to  $K\bar{K}$  and to  $\gamma\pi$  would be forbidden. Differences in the cross-section for the production of the two resonances at different energies should give a variation in the experimentally determined branching ratios of the  $A_2$ . Fig. 59, the experimentally measured branching ratios,  $A_2 \rightarrow K\bar{K} / A_2 \rightarrow \rho\pi$ , and  $A_2 \rightarrow \gamma\pi / A_2 \rightarrow \rho\pi$  are shown as a function of the momentum of the incident particle ( $\pi^+$  or  $\pi^-$ ) including the values obtained by this experiment. No evidence for a variation in the branching ratio can be seen.

FIG. 59



A fit to the experimental data of the form:-

branching ratio  $\propto 1/(1 + R_p^{1.5})$  (See appendix B) has been made. The best fit is given by  $R = 0.005 \pm 0.01$  which is consistent with zero. On the basis of this fit, one concludes that the proportion of a  $2^-$  or  $1^+$  meson in the  $\rho\pi$  peak at the position of the  $A_2$  is less than 15% in this experiment.

The decay modes  $K\bar{K}$  and  $\rho\pi$  have been examined separately to check the correctness of assuming both to be a decay of the same particle.

#### 6.5 The $K\bar{K}$ decay mode

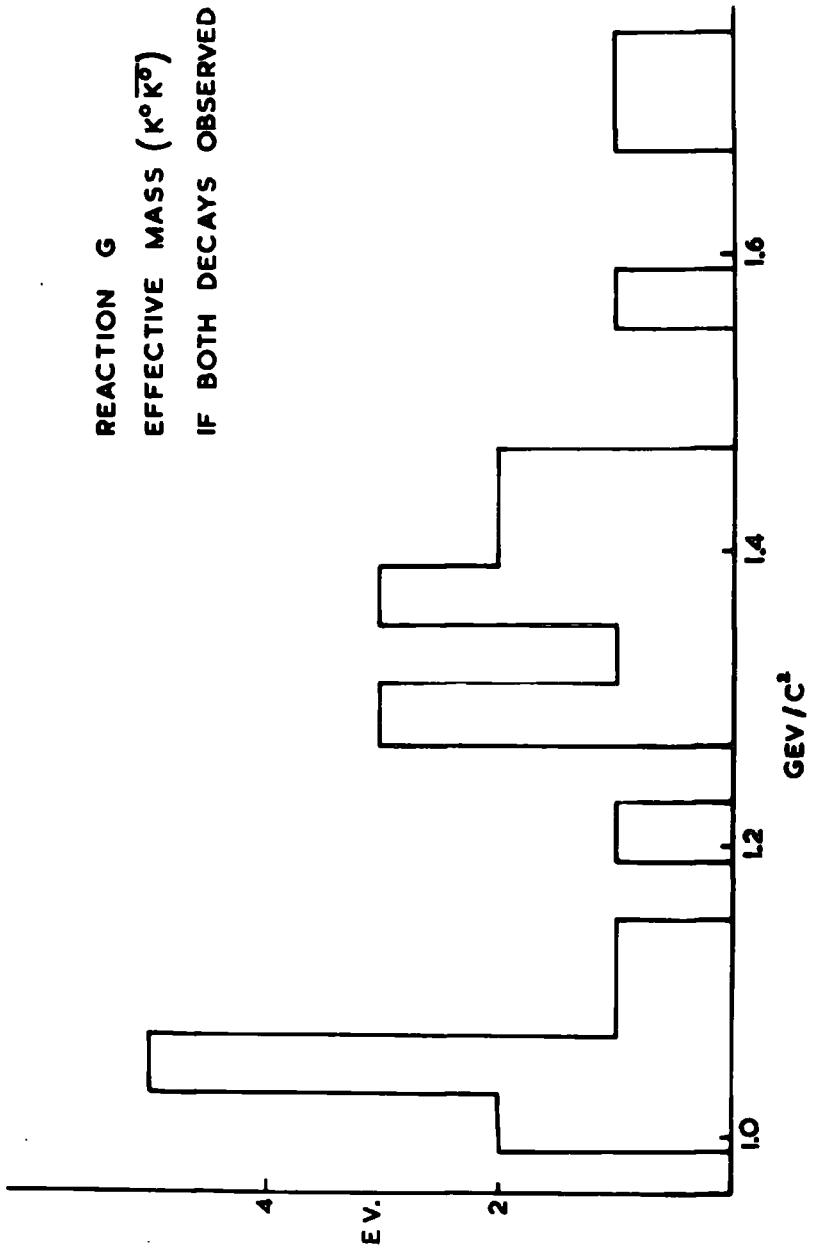
The  $K\bar{K}$  decay is observed as  $K^+K^0$ ,  $K^+K^-$  and  $K^0\bar{K}^0$ . The fact that the  $K^+K^0$  mode is observed establishes that  $I = 1$ . The decay of states of definite  $I, I_3$  and  $G$  to  $K\bar{K}$  was discussed in chapter 1. For the decay of an  $I = 1$  neutral meson, the decay modes are as follows.

|      |  |                |
|------|--|----------------|
| Odd  | $G -$ parity, $K^+K^-, K_S K_S, K_L K_L$ | in ratio 2:1:1 |
| Even | $G -$ parity, $K^+K^-, K_S K_L$          | in ratio 1:1   |

Fig. 60 shows the distribution of the effective mass of  $K^0\bar{K}^0$  in reaction G for the events where both decays are seen. The background is low in this distribution because the probability of observing two uncorrelated  $K^0$  decays as  $K_S$  is  $1/9$ , and the

FIG. 60

REACTION G  
EFFECTIVE MASS ( $K^0 \bar{K}^0$ )  
IF BOTH DECAYS OBSERVED



concentration around the mass of the  $A_2$  is clearly seen. It is estimated that there are  $8.5 \pm 3.5$  events in the peak. The probability of seeing both decays of  $K_s K_s$  is  $4/9$  so there is good agreement with the number of events in which at least one decay is observed (probability  $8/9$ ). The agreement with the rate of decay to  $K^+ K^-$  has already been pointed out. The observed decay to  $K^0 \bar{K}^0$  is therefore seen to be quite consistent with a state of odd G-parity. For a decay to  $K\bar{K}$ , the following relation holds:-

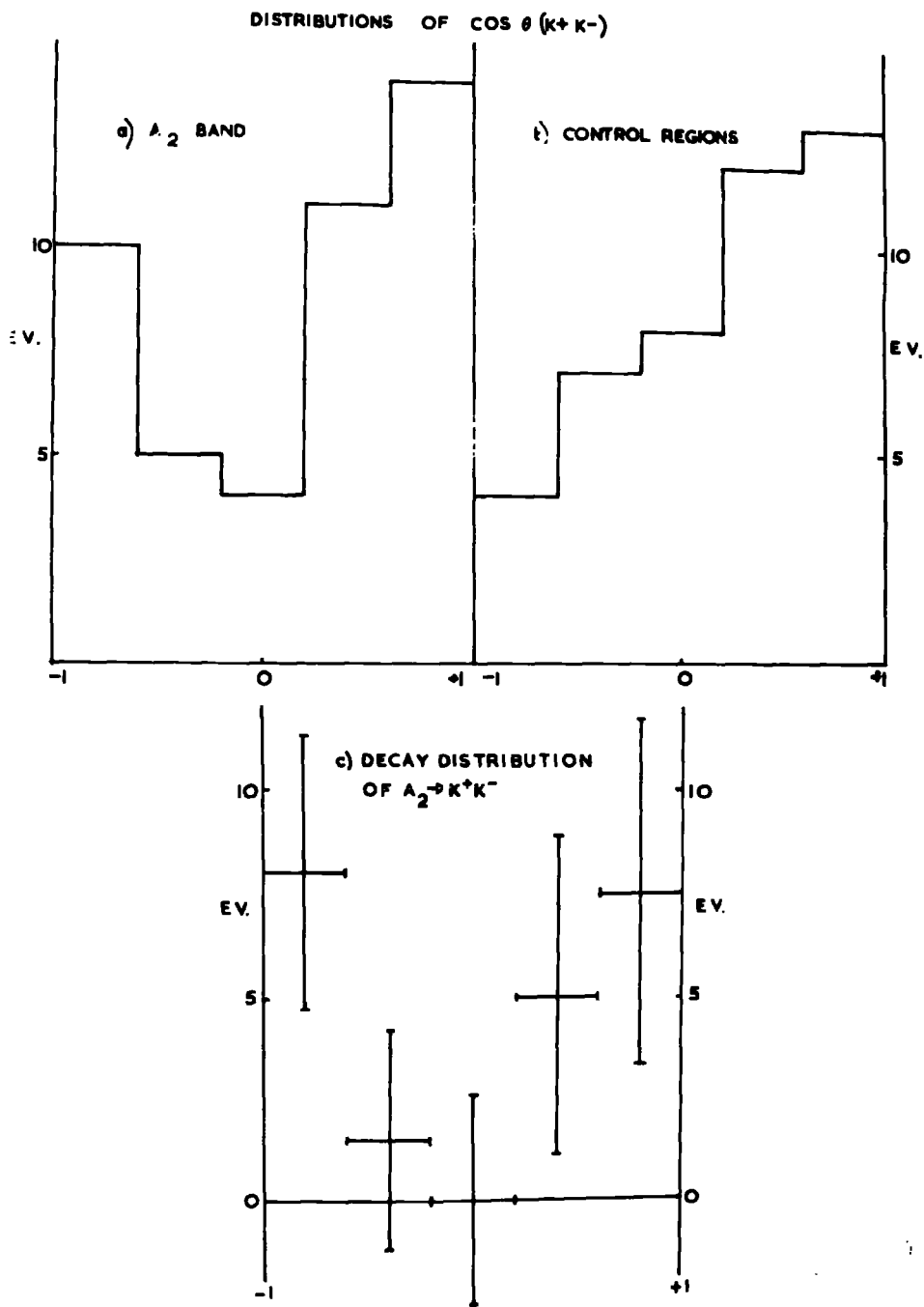
$$G = (-1)^l + I,$$

where  $l$  is the orbital angular momentum of the  $K\bar{K}$  system. It follows then that  $l$  must be even, and that for the parent particle,  $J$  must also be even. This further leads to the conclusion that the parity is even.

Of course, the assumption has been made that the decay to  $K\bar{K}$  is a strong decay so that the relevant conservation laws are valid. The observed width of the peak supports this assumption.

The decay angular distribution of the  $K^+ K^-$  decay mode has been examined. Fig. 61 (a) shows the angle between the  $K^+$  and the incoming  $\pi^+$ , in the

FIG. 61.



centre of mass system of the  $K^+K^-$ , if the  $K^+K^-$  has an effective mass system in the range 1225 to 1400  $\text{MeV}/c^2$ . Fig. 61 (b) shows the distribution of the same angle for the control regions, that is for those  $K^+K^-$  systems with effective mass in the ranges 1050 to 1225  $\text{MeV}/c^2$  and 1400 to 1575  $\text{MeV}/c^2$ . The background in the  $A_2$  region was estimated as half the distribution for the control regions, and the decay angular distribution for the  $A_2$  region, after subtracting the background, is shown in fig. 61 (c). The distribution is not in agreement with an isotropic decay to  $K^+K^-$  ( $\chi^2$  probability = 0.18) which is evidence against an S-state. A spin assignment of 2 is not contradicted by the observed decay distribution.

The  $K\bar{K}$  decay modes of the  $A_2$  as observed in this experiment have been studied. The experimental evidence favours the accepted quantum numbers for the  $A_2$  i.e.  $I^G J^P = 1^- 2^+$ .

### 6.6 The $\rho\pi$ decay mode

That the G parity of the  $A_2$  is odd can be concluded directly from the fact that the decay is to three pions. Further, the spin and parity of the  $A_2$  to  $\rho\pi$  has been determined by the ABC collaboration (46) and by Armenise et al. (47)

who find good evidence for  $J^P = 2^+$ . These quantum numbers are in agreement with those for the  $K\bar{K}$  mode. That the isospin is also in agreement can be confirmed by observing the different charge modes for the  $N^*A_2$  reaction. The initial  $\pi^+p$  system has  $I = 3/2$  and  $I_3 = +3/2$ , and the relative proportions of the different charge modes can be calculated from Clebsch-Gordan coefficients assuming  $I = 1$  for the  $A_2$ . Table 19 gives firstly the fraction of the production process in which the appropriate charge state of  $N^*A_2$  is produced. The table then gives the probability that the  $N^*$  and  $A_2$  decay in the observed mode, and the fraction of the  $N^*A_2$  reactions which proceed in the way shown. The corresponding fractions assuming that  $I = 2$  for the  $A_2$  meson are also given in the table.

The cross-section for the first process has already been shown to be  $89 \pm 13 \mu\text{b}$ . There is no significant evidence for  $N^{*+}$  produced in reactions B and D, but as the  $A_2$  is observed to be produced only in association with an  $N^*$  in reaction B, events were selected in which the  $p\pi^0$  (reaction B) or an  $n\pi^+$  (reaction D) combination has an effective mass

TABLE 19

Charge Modes of  $N^*A_2$  production

| Reaction | Process   | $I(A_2) = 1$  |               |                              |                | $I(A_2) = 2$  |               |                              |                |
|----------|---|---------------|---------------|------------------------------|----------------|---------------|---------------|------------------------------|----------------|
|          |   | Fraction of:- |               |                              |                | Fraction of:- |               |                              |                |
|          |   | prod          | $N^*$ decay   | $A_2 \rightarrow p\pi$ decay | total          | prod          | $N^*$ decay   | $A_2 \rightarrow p\pi$ decay | total          |
| B        | 1) $N^{*++} A_2^0$<br>$\hookrightarrow p\pi^+ \hookrightarrow p^+\pi^+$   | $\frac{3}{5}$ | 1             | 1                            | $\frac{9}{15}$ | $\frac{1}{5}$ | 1             | *                            | *              |
| B        | 2) $N^{*+} A_2^+$<br>$\hookrightarrow p\pi^0 \hookrightarrow p^0\pi^+$    | $\frac{2}{5}$ | $\frac{2}{3}$ | $\frac{1}{2}$                | $\frac{2}{15}$ | $\frac{2}{5}$ | $\frac{2}{3}$ | $\frac{1}{2}$                | $\frac{2}{15}$ |
| D        | 3) $N^{*+} A_2^+$<br>$\hookrightarrow n\pi^+ \hookrightarrow p^0\pi^+$    | $\frac{2}{5}$ | $\frac{1}{3}$ | $\frac{1}{2}$                | $\frac{1}{15}$ | $\frac{2}{5}$ | $\frac{1}{3}$ | $\frac{1}{2}$                | $\frac{1}{15}$ |
| B        | 4) $N^{*0} A_2^{++}$<br>$\hookrightarrow p\pi^- \hookrightarrow p^+\pi^+$ | 0             |               |                              |                | $\frac{2}{5}$ | $\frac{1}{3}$ | 1                            | $\frac{2}{15}$ |

\*Assuming  $I = 2$ , the decay  $A_2^0 \rightarrow p^0\pi^0$  would account for  $2/3$  of the decays, and it is uncertain what proportion of these decays would be detected as being compatible with  $p^+\pi^+$  decays. In any case,  $3/15$  can be quoted as the upper limit to the fraction of  $N^* A_2$  reactions.

in the range 1.14 to 1.30 GeV/c<sup>2</sup>. Fig. 62 shows the distribution of the effective mass of the remaining  $\pi^+\pi^+\pi^-$  combination if either of the  $\pi^+\pi^-$  combinations is compatible with a  $\rho^0$  (0.66 to 0.86 GeV/c<sup>2</sup>). In each case a small peak is observable at the position of the  $A_2$ , which remains when events with  $|t| < 1.0 \text{ GeV}^2$  are selected (the dashed histograms). By estimating the number of events above a smooth background, the cross-sections for the second and third processes respectively are estimated to be  $17 \pm 8$  and  $12 \pm 6 \mu\text{b}$ . The experimentally observed ratios for the three  $N^* A_2$  processes are  $9 : (1.9 \pm 0.9) : (1.35 \pm 0.7)$  which are in good agreement with the expected 9:2:1 for  $I(A_2) = 1$ .

Fig. 63 shows the effective mass distribution for the  $\pi^+\pi^+\pi^0$  system with a  $\pi^+\pi^0$  combination having a mass compatible with the  $\rho$  mass, and requiring that the associated  $\rho\pi^-$  system is compatible with the  $N^*$  mass. As expected, there is no evidence for  $A_2^{++}$ .

The evidence is therefore in favour of the  $A_2$  decaying to  $\rho\pi$  being an  $I = 1$  meson, and that there is no contribution to the  $A_2$  peak from an  $I = 2$  meson.

FIG. 62

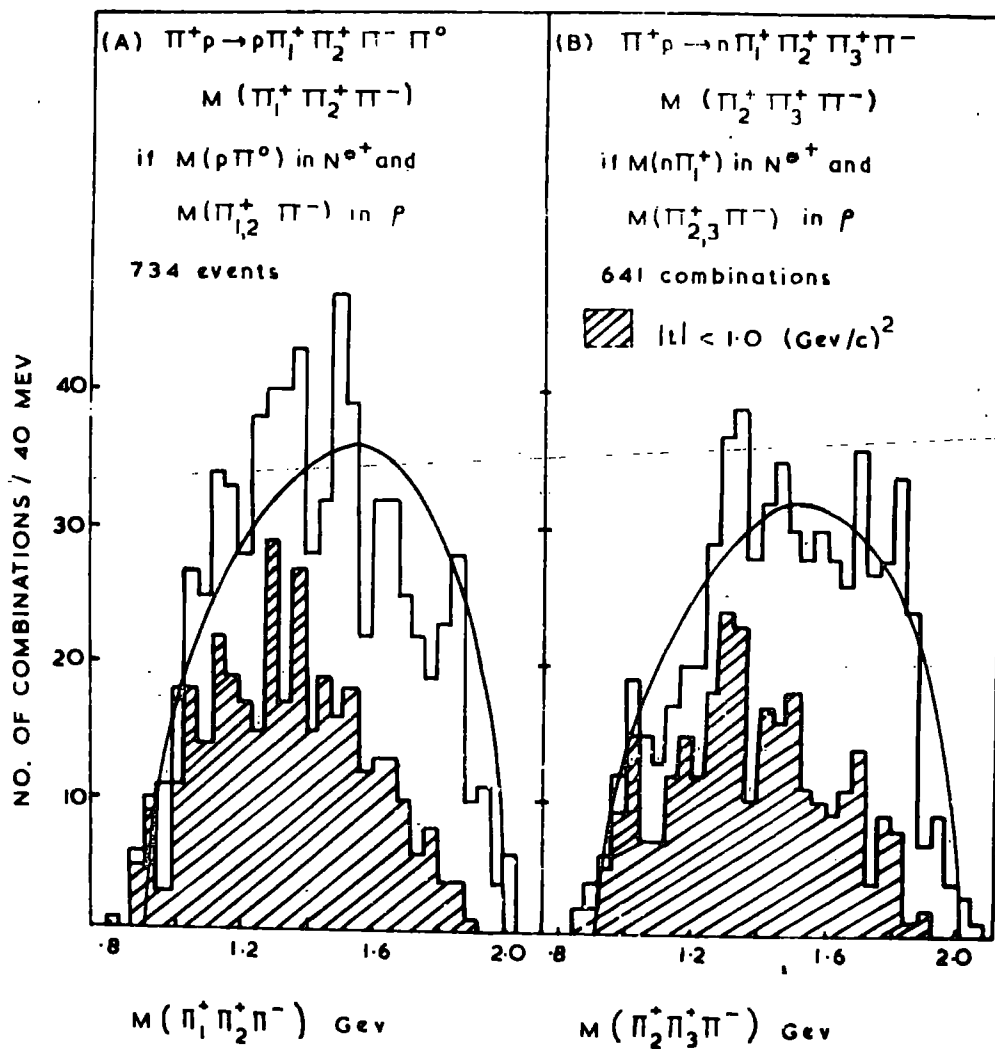
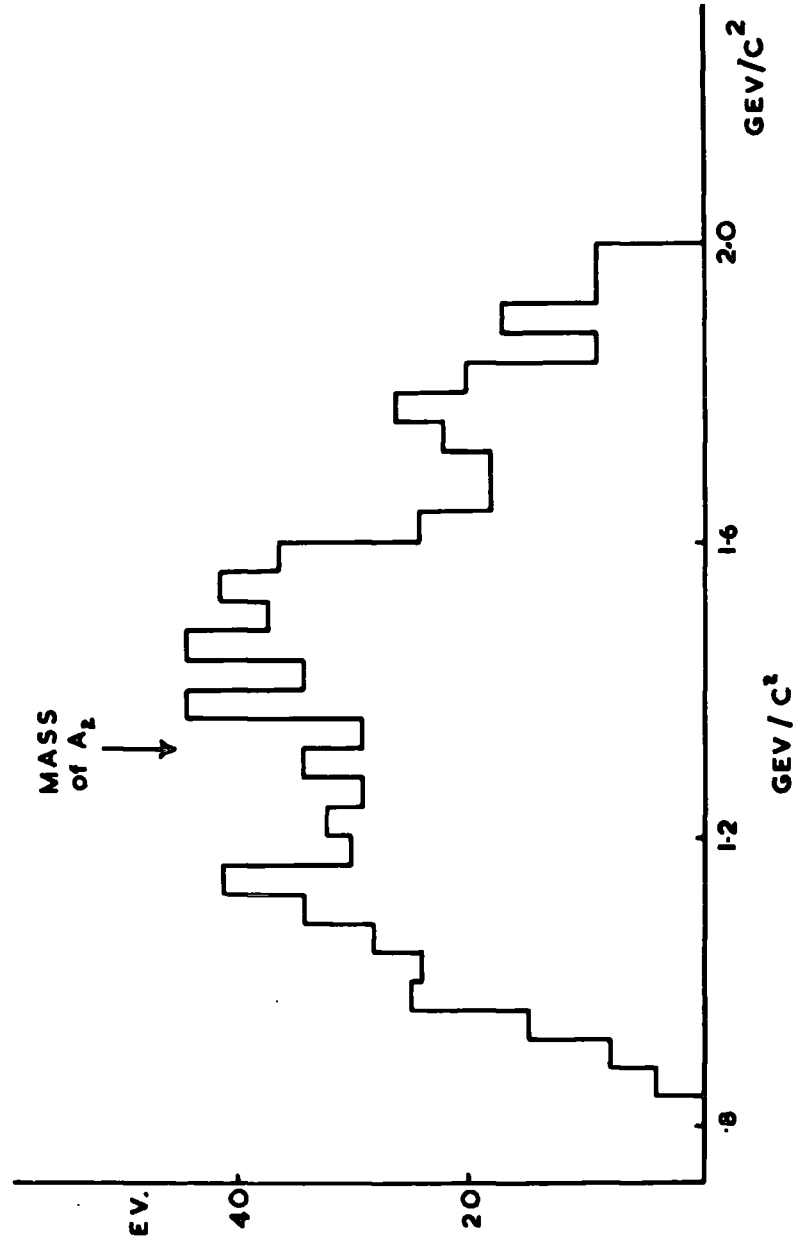


FIG. 63 MASS ( $p^+ \pi^-$ ) WITH  $N^{p0} \rightarrow p \pi^-$



## 6.7 Conclusions

Decays to  $\rho\pi$  and to  $K\bar{K}$  have been observed. The central mass values of the peaks show a hardly significant difference. The quantum numbers of the  $A_2$  deduced from the different decay modes are the same. The evidence of this experiment is therefore not in agreement with the suggestion that there are two resonances with different decay modes at the mass of the  $A_2$ , but that different decay modes of one particle are observed. With this assumption, the branching ratios of these modes and of the  $\eta\pi$  decay mode of the  $K\bar{K}$  decay mode of the  $A_2$  have been determined.

## CONCLUSION

An experiment has been described in which the interactions of 5 GeV/c positive pions with protons has been investigated. The observed cross-sections for the different final states are in good agreement with the general trend as observed in other experiments.

A large fraction of the interactions have been seen to take place via the production of intermediate resonant states, and the cross-sections for the observation of these states have been determined. In particular, a considerable number of interactions have been observed to proceed through one of several quasi-two-body reactions. The observed two-body processes are  $N^*\rho^0$ ,  $N^*\pi^0$ ,  $N^*\omega^0$ ,  $N^*\gamma^0$ ,  $N^*A_2$ ,  $pA_2$  and  $pB^+$ , and two types of investigation of these reactions have been made.

The first of these has been to examine two reactions for the purpose of understanding the mechanisms by which the reactions take place. The reaction  $N^*\rho^0$  has been investigated on the basis of the absorptive OPE model, with the exchange of a pion. The spin density matrix elements, determined by the Gottfried-Jackson analysis method from the decay angular distributions, have been shown to have a similar behaviour to those found in other experiments. That is, that the overall agreement was

good, with only small deviations from the theoretical predictions. The agreement has been found to be good in spite of the problem of isolating a pure sample of  $N^*\rho^0$  interactions, as is evident from the asymmetrical decay of the  $\rho^0$ . Some significant correlation has been observed between the decays of the  $N^*$  and the  $\rho^0$ , which is itself indicative of absorptive corrections in the reaction mechanisms. The  $N^*\omega^0$  reaction has been investigated in a similar manner on the basis of the exchange of the vector  $\rho$  meson. The spin density matrix elements were found to be in reasonable agreement with those found in other experiments, but in serious disagreement with the predictions of the absorption model. The results of this experiment serve to underline the remarks made in chapter 1, that the absorption model works very well for pseudoscalar meson exchange, but poorly for vector meson exchange.

The differential cross-sections for the reactions  $N^*\rho^0$  and  $N^*\omega^0$  have been examined, and the slope of the approximately exponential part of the distributions was determined. The measured slopes were found to be in agreement with those found at 8 GeV/c. In addition, a small but significant backward peak in the  $N^*\rho^0$  reaction was interpreted

as being due to a baryon exchange mechanism. The differential cross-section for backward  $N^* \rho^0$  production was examined, and the slope of the distribution was found to be much smaller than for meson exchange interactions. This fact could be interpreted as due to the exchange of a heavier particle or, on the optical model, to a smaller radius for the production.

The second type of investigation on two-body processes has been to examine a reaction for the purpose of determining the properties of one of the products. Such has been the case for the  $B^+$  meson and the  $A_2$  meson.

The measured mass and width of the  $B^+$  meson from this experiment agree well with the results of other experiments. In addition the angular distribution of its decay to  $\omega^0 \pi^+$  has been investigated. The observed decay of the  $B^+$  was isotropic, which is consistent with an S-wave decay, that is a  $J^P = 1^+$  assignment for the B meson.

The  $A_2$  meson has also been investigated. It was observed in its three decay modes,  $\rho\pi$ ,  $\gamma\pi$  and  $K\bar{K}$ , and the measured branching ratios from this experiment were in agreement with other determinations. There has been speculation recently, after the observation

of a splitting in the  $A_2$  peak in a missing mass spectrometer experiment, that there may be two resonances at the  $A_2$  position, having different decay modes or at least different branching ratios. Historically, some of the quantum numbers of the  $A_2$  have been deduced assuming it to decay both to  $\rho\pi$  and to  $K\bar{K}$ . These two decay modes have been discussed separately here, and the evidence points to the same assignment of I, G, J and P for both decays, so the assumption that these are different decay modes of the same resonance seems to be justified. The  $N^*A_2$  reaction was observed in different charge modes, and the ratio in which these were observed seems to discount the possibility of an  $I=2$  resonance being included in the peak. The suggestion of Morrison, that a resonance with  $J^P=1^+$  or  $2^-$  might give rise to an apparent variation of the branching ratio of the  $A_2$  with the momentum of the incident pion, has been investigated. No evidence for such a variation was found.

ACKNOWLEDGEMENTS

The author wishes to thank Professor G. D. Rochester for his encouragement and for his interest in the work. He is especially indebted to Dr. J. V. Major for his guidance throughout this work, and also to his colleagues in the High Energy Nuclear Group of this University and his collaborators in other universities for their assistance with various stages of this work.

His thanks are also due to the technical staff of the Physics Department, especially to those who have maintained the measuring machines in working order, and to those who have carefully scanned and measured the photographs. He would also like to thank Mr. M. Lee for his work in photographing the diagrams and Miss Margaret Foord for typing this thesis. Thanks are also due to the personnel of the British National Hydrogen Bubble Chamber.

Finally, the author would like to thank the Science Research Council for a studentship and for travel grants.

APPENDIX A

In Reap, an optional test on the quality of the measurement of a track is available. This test has the advantage of being quicker than the complete fitting of a curve to the measured points of a track at the expense of making some approximation. In cases where this test failed, the full check on the track was made and the deviation of each point from the fitted curve was printed out for examination.

The test is based on the quantity:-

$$K = \frac{L_1 + L_2 - L_3}{L_1 \cdot L_2 \cdot L_3}$$

where  $L_1$ ,  $L_2$  and  $L_3$  are defined in fig. 11(b)

Suppose that:-

$r$  is the radius of the circle passing through the three measured points.

$\theta$  is the (acute) angle between the two chords  $L_1$  and  $L_2$ .

Then:

$$L_3^2 = L_1^2 + L_2^2 + 2L_1L_2 \cos \theta \quad \dots(1)$$

Since the section of track over which three successive points are measured is small compared with the radius of curvature of the track, the angle  $\theta$  is small, and equ.(1) can be written to a very good approximation:-

$$L_3^2 = L_2^2 + L_1^2 + 2L_1L_2(1 - 1/2 \theta^2) \quad \dots(2)$$

and also:  $\theta \doteq \frac{L_1 + L_2}{2r}$  ... (3)

Combining equ.(2) and (3) one obtains that:-

$$\frac{1}{4r^2} = \frac{(L_1 + L_2 + L_3) \cdot (L_1 + L_2 - L_3)}{L_1 \cdot L_2 \cdot L_3} \quad \dots(4)$$

Making the further small angle approximation that

$L_3 \doteq L_1 + L_2$ , equ. (4) becomes:-

---

$$\frac{1}{8r^2} = \frac{L_1 + L_2 - L_3}{L_1 \cdot L_2 \cdot L_3} = K \quad \dots(5)$$

The quantity K is therefore a function of the radius of curvature of a track. Its value was calculated for each set of three consecutively measured points, and successive values were compared.

APPENDIX B

Morrison (45) has suggested the possibility of the existence of two resonances with mass similar to that assigned to the  $A_2$  meson. One with  $J^P = 2^+$  would decay to  $\rho\pi$  as well as to  $K\bar{K}$  and to  $\gamma\pi$ . The other meson having  $J^P = 1^+$  or  $2^-$  could decay to  $\rho\pi$ , but decays to  $K\bar{K}$  and to  $\gamma\pi$  would be forbidden. Expressing the variation of production cross-section with the momentum of the incoming pion ( $p$ ) in the form:-

$$\sigma(p) \propto p^n$$

it is suggested that for production taking place by exchange of a meson,  $n \approx -1.5$ , and for production which could take place by Pomeranchuk exchange (e.g. the  $1^+$  or  $2^-$  meson)  $n \approx 0$

Writing the cross-section for the production of  $A_2$  (decaying to  $\rho\pi$ ) in the form:-

$$\sigma_2(p) = c_2 p^{-1.5}$$

and for the assumed  $1^+$  or  $2^-$  meson

$$\sigma_3(p) = c_3$$

Suppose that  $K$  is the branching ratio  $A_2 \rightarrow K\bar{K} / A_2 \rightarrow \rho\pi$  and  $\gamma$  is the branching ratio

$A_2 \rightarrow \gamma\pi / A_2 \rightarrow \rho\pi$ . The cross-section for the production of  $A_2$  decaying in these two alternative modes would be  $K \sigma_2(p)$  and  $\gamma \sigma_2(p)$ .

If in an experiment, the two peaks in the effective mass spectrum could not be resolved, the measured branching ratios would be:-

$$\frac{A_2 \rightarrow K\bar{K}}{A_2 \rightarrow \rho\pi} = \frac{K \sigma_2(p)}{\sigma_2(p) + \sigma_3(p)} = \frac{K}{1 + R.p^{1.5}}$$

where  $R = C_3/C_2$

$$\text{and } \frac{A_2 \rightarrow \gamma\pi}{A_2 \rightarrow \rho\pi} = \frac{\gamma}{1 + R.p^{1.5}}$$

On the basis of the hypothesis of a  $1^+$  or  $2^-$  meson with a mass similar to that of the  $A_2$  meson, one would expect the measured branching ratio of the decay modes of the  $A$  would vary with the momentum of the incident pion in a way similar to the expressions above. The existence of the extra meson would give a non-zero value of  $R$ .

REFERENCES

1. L.Michel, Il Nuovo Cimento 10, 319 (1953).
2. T.D.Lee and C.N. Yang, Il Nuovo Cimento 3, 749 (1956).
3. M.Goldhaber, T.D.Lee and C.N.Yang, Physical Review 112, 1796 (1958).
4. M.Gell-Mann, California Institute of Technology Synchrotron Laboratory Report, CTSL-20 (1961).
5. Y.Ne'eman, Nuclear Physics 26, 222 (1961).
6. V.E. Barnes et al., Physical Review Letters 12, 204 (1964).
7. M.Gell-Mann, Physics Letters 8, 214 (1964).
8. F.Gursey and L.A.Radicati, Physical Review Letters 13, 173 (1964).
9. Badier et al., Proceedings of the Oxford International Conference on Elementary Particles (1965).
10. Aachen-Berlin-CERN Collaboration, Physics Letters 19, 608 (1965).
11. E.Ferrari and F.Selleri, Il Nuovo Cimento 27, 1450 (1963).
12. N.J.Sopkovich, Il Nuovo Cimento 26, 186 (1962).
13. K.Gottfried and J.D.Jackson, Il Nuovo Cimento 34, 735 (1965).
14. E.Kiel and W.W.Neale, CERN Internal Report, TC/02 63-3 (1963).
15. P.R.Williams, CERN Internal Report, TC/NBC 65-1 (1965).
16. W.Blum, CERN Internal Report, TC/NBC 63-2 (1963).
17. G.Kellner, CERN Internal Report, TC/NBC 65-4 (1965).

18. Bonn-Durham-Nijmegen-Paris(E.P.)-Turin Collaboration, to be published in Physical Review.
19. C.Alff et.al., Physical Review Letters 9, 322 (1962).
20. M.Abolins et.al,Physical Review Letters 11, 381 (1963).
21. G.Goldhaber et al., Physical Review Letters 12, 336 (1964).
22. Aachen-Berlin-Birmingham-Bonn-Hamburg-London (I.C.)-Munchen Collaboration, Physical Review 138B, 897 (1965).
23. Aachen-Berlin-CERN Collaboration Physics Letters 12, 356 (1964).
24. H.L.Anderson, Proceedings of the 6th Annual Rochester Conference on High Energy Nuclear Physics (1965).
25. R.T. Deck, Physical Review Letters 13, 169 (1964).
26. K.Gottfried and J.D.Jackson, Il Nuovo Cimento 33, 309 (1964).
27. J.D. Jackson, Reviews of Modern Physics 37, 484 (1965)
28. Aachen-Berlin-Birmingham-Bonn-Hamburg-London(I.C.)-Muchen Collaboration, Il Nuovo Cimento 35, 659 (1965).
29. L.Bondar et al., Physics Letters 5, 209 (1963).
30. U.Maor and T.A.O'Halloran Jr., Physics Letters 15, 281 (1965).
31. C. Baltay et al., Physical Review Letters 18, 93 (1967).
32. D.D. Carmony et al., Physical Review Letters 12, 254 (1964).

33. R.I.Hess, Thesis, Berkeley (1966), quoted in ref.34.
34. A.H.Rosenfeld et al., Reviews of Modern Physics 39, 1 (1967).
35. Aachen-Berlin-Birmingham-Bonn-Hamburg-London(I.C.)-Muchen Collaboration, Physics Letters 10, 240 (1964).
36. S.U.Chung et al., Physical Review Letters 16, 481 (1966).
37. G.Goldhaber et al., Physical Review Letters 15, 118 (1965).
38. G.Chikovani et al., Physics Letters 25B, 44 (1967).
39. S.U.Chung et al., Physical Review Letters 15, 325 (1965).
40. Dubovikov et al., quoted in ref.34.
41. Aachen-Berlin-CERN Collaboration, quoted in ref.45.
42. Genova-Hamburg-Milan-Saclay Collaboration, quoted in ref.45.
43. R.L.Lander et al., Physical Review Letters 13, 346a (1964).
44. R. Armenteros et al., Physics Letters 17, 344 (1965).
45. D.R.O.Morrison, Physics Letters 25B, 238 (1967).
46. Aachen-Berlin-CERN Collaboration, Physics Letters 25B, 48 (1967).
47. N.Armenise et al., Physics Letters 25B, 53 (1967).

## LIST OF FIGURES

### Figure

1.  $\pi^+p$  total and elastic cross-sections.
2.  $K^+p \rightarrow$  three-body cross-sections.
3. Feynman diagrams for CPE models.
  - a) Simple CPE model.
  - b) CPE model with absorption.
4. Layout of the  $C\alpha$  beam.
5. Plan view of the British National Hydrogen Bubble Chamber.
6. Diagram of the British National Hydrogen Chamber, showing the scan zone, fiducial marks and approximate positions of cameras.
7. Test of Fiducial mark system.
8. System of analysis of the data.
9. Form of paper tape output from the measuring machines.
10. General structure of Reap.
11. Track tests in Reap.
12. Relative ionisation.
13. Plot of the square of the missing mass ( $MM^2$ ) against the missing energy (ME).
14. Four-prong cross-sections.
15. The square of the missing mass for reactions A, B and D.
16. Reaction A:  $\chi^2$  distribution for each laboratory in the collaboration.
17. Reaction B:  $\chi^2$  distribution for each laboratory in the collaboration.
18. Angular distributions.

Figure

19. Reaction A:  
Effective mass of  $\rho\pi^+$  versus effective mass  
of  $\pi_2^+\pi^-$
20. Reaction A:  
Effective mass of  $\rho\pi^+$
21. Reaction A:  
Effective mass of  $\pi^+\pi^-$
22. Reaction A:  
Effective mass of  $\pi^+\pi^-$ , remaining  $\rho\pi^+$  compatible  
with an  $N^*$ .
23. Two-body cross-sections versus the laboratory  
momentum of the incident pion.
  - a)  $\pi^+p \rightarrow N^*\rho^0$
  - b)  $\pi^+p \rightarrow N^*\rho^+$
  - c)  $\pi^+p \rightarrow N^*\omega^0$
24. Reaction A: - Effective mass of  $\pi^+\pi^-$ 
  - a)  $\cos \theta_{\pi^+} > 0$
  - b)  $\cos \theta_{\pi^+} < 0$

$\theta_{\pi^+}$  is the angle between the incident  $\pi^+$  and  
the outgoing  $\pi^+$ .
25. Reaction A: -  $t(\pi^+/\pi^+\pi^-)$  versus effective  
mass of  $\pi^+\pi^-$ .
26. Reaction A: Effective mass of  $\rho\pi_1^+$  versus  
effective mass of  $\pi_2^+\pi^-$ ,  
if  $-t < 0.3 \text{ GeV}^2$ .
27. Reaction A: Differential cross-section for  
 $N^*\rho^0$  production.
28. Reaction A: Section of fig. 25 for high values  
of  $|t|$ .
29. Reaction A: Differential cross-section for  
 $N^*\rho^0$  production by baryon exchange.

Figure

30. Reaction A: Spin density matrix elements for  $N^* \rho^0$  production.
31. Reaction A: Correlation of the angular distributions of  $N^*$  and  $\rho^0$  decays.
32. Reaction A: Effective mass of  $\pi^+ \pi^+ \pi^-$ .
33. Reaction A: Effective mass of  $\pi^+ \pi^+ \pi^-$ , if one  $\pi^+ \pi^-$  combination is compatible with  $\rho^0$ , but excluding events compatible with  $N^* \rho^0$  production.
34. Reaction B: Effective mass of  $\rho \pi^+$  versus of effective mass of  $\pi^+ \pi^- \pi^0$ .
35. Reaction B: Effective mass of  $\rho \pi^+$ .
36. Reaction B: Effective mass of  $\pi^+ \pi^- \pi^0$ .
37. Reaction B: Effective mass of  $\pi^+ \pi^- \pi^0$ , remaining  $\rho \pi^+$  compatible with  $N^*$ .
38. Reaction B: Number of  $\omega$ 's versus effective mass of  $\rho \pi^+$ .
39. Reaction B: Differential cross-section for  $N^* \omega^0$  production.
40. Reaction B: Spin density matrix elements for  $N^* \omega^0$  production.
41. Reaction B: Correlation of the angular distributions of  $N^*$  and  $\omega^0$  decays.
42. Reaction B: Effective mass of two-pion systems,
  - a)  $\pi^+ \pi^-$
  - b)  $\pi^+ \pi^0$
  - c)  $\pi^- \pi^0$
43. Reaction B: Effective mass of  $\pi^+ \pi^- \pi^0$ , if  $\pi^+ \pi^0$  or  $\pi^- \pi^0$  is compatible with  $\rho$ , and the associated  $\rho \pi^+$  is compatible with  $N^*$ .

Figure

44. Reaction B:

- a) Effective mass of  $\pi^+\pi^+\pi^-\pi^0$
- b) Effective mass of  $\pi^+\pi^+\pi^-\pi^0$ , if a  $\pi^+\pi^-\pi^0$  combination is compatible with  $w^0$ .

45. Reaction B: Dalitz plot; effective mass of  $\pi^+\pi^-\pi^0$  versus the effective mass of  $p\pi^+$ .

46. Definition of  $\theta_B$ .

47. Reaction B: Effective mass of  $w^0\pi^+$  versus  $\cos \theta_B$ .

48. Distribution of  $\cos \theta_B$ .

- a)  $B^+$  meson region
- b) control regions
- c) difference between distributions a) and b).

49. Reaction B: Effective mass of  $w^0\pi^+$ ,

- a)  $|\cos \theta_B| < 0.5$
- b)  $|\cos \theta_B| > 0.5$

50. Reaction E: Effective mass of  $p\pi^+$ .

51. Reaction E: Effective mass of  $pK^-$ .

52. Reaction E: Effective mass of  $K^-\pi^+$ .

53. Reaction E: Effective mass of  $K^+K^-$ .

54. Reaction B: Effective mass of  $\pi^+\pi^+\pi^-\pi^0$ , if a  $\pi^+\pi^-\pi^0$  combination is compatible with  $\gamma^0$ .

55. Reaction F: Effective mass of  $K^+K^-$ .

56. Reaction E:

- a) Effective mass of  $p\pi^+$  versus effective mass of  $K^+K^-$ .
- b) Effective mass of  $K^+K^-$ , if  $p\pi^+$  is compatible with  $N^*$ .

Figure

57. Reaction G:
- Effective mass of  $\rho\pi^+$  versus effective mass of  $K^0\bar{K}^0$ .
  - Effective mass of  $K^0\bar{K}^0$ , if  $\rho\pi^+$  is compatible with  $N^*$ .
58. Cross-section for  $\pi^+\rho \rightarrow \rho A_2 (A_2 \rightarrow \rho^0 \pi^+)$  versus laboratory momentum of incident  $\pi^+$ .
59. Branching ratios of  $A_2$  decay versus laboratory momentum of incident particle in the experiment in which it was determined.
60. Reaction G: Effective mass of  $K^0\bar{K}^0$ , if both decays are observed.
61. Reaction E: Angular distribution of  $K^+K^-$  system.
- $A_2$  region,
  - control regions,
  - difference between a) and b).
62. a) Reaction B: Effective mass of  $\pi^+\pi^+\pi^-$ , if a  $\pi^+\pi^-$  combination is compatible with  $\rho^0$ , and  $\rho\pi^0$  is compatible with  $N^*$ .
- b) Reaction D: Effective mass of  $\pi^+\pi^+\pi^-$ , if a  $\pi^+\pi^-$  combination is compatible with  $\rho^0$ , and  $n\pi^+$  is compatible with  $N^*$ .
63. Reaction B: Effective mass of  $\pi^+\pi^+\pi^0$ , if a  $\pi^+\pi^0$  combination is compatible with  $\rho^+$ , and  $\rho\pi^+$  is compatible with  $N^*$ .

LIST OF TABLES

| <u>Table</u>  | <u>Page No.</u> |
|---|-----------------|
| 1. $K\bar{K}$ Eigenstates of I, $I_3$ and G                               |                 |
| 2. Test of no-field film  | 29.             |
| 3. Rejection Criteria   | 47.             |
| 4. 4-prong cross-sections   | 55.             |
| 5. Distribution of fitted hypotheses                                      | 56.             |
| 6. Percentage of type A fits  | 58.             |
| 7. Ratio of type B fits to type A fits                                    | 59.             |
| 8. Reaction cross-sections  | 60.             |
| 9. Median $\chi^2$ for reaction B   | 65.             |
| 10. Comparison of $\omega^0$ peaks  | 66.             |
| 11. Forward-backward ratios   | 67.             |
| 12. $d\sigma/dt$ slopes for regions adjacent to $N^* \omega^0$ region     |                 |
| 13. Coefficients of $N^*$ and $\rho^0$ decay distributions                | 85.             |
| 14. $d\sigma/dt$ slopes for regions adjacent to $N^* \omega^0$ region     |                 |
| 15. Coefficients of $N^*$ and $\omega^0$ decay distributions              | 93.             |
| 16. Mass and width of $B$ meson   | 100.            |
| 17. Branching ratio $A_2 \rightarrow \gamma\pi / A_2 \rightarrow \rho\pi$ | 107.            |
| 18. Branching ratio $A_2 \rightarrow K\bar{K} / A_2 \rightarrow \rho\pi$  | 111.            |
| 19. Charge modes of $N^* A_2$ production                                  | 118.            |